POLITECNICO DI TORINO

Master's Degree in Civil Engineering

MASTER'S DEGREE THESIS

Life Cycle Analyses Integration in Structural and Environmental optimizations of Steel-Framed Structures

Supervisor:

Prof. Giuseppe Carlo Marano

Co-supervisors:

Dott. Eng. Raffaele Cucuzza
Dott. Eng. Roberta Di Bari

Candidate:

Benedetta Bartoli

OCTOBER 2023 - A.Y. 2022/2023

Abstract

Lowering environmental effects has lately been a key objective of structural optimization due to the significant amount of CO_2 emissions in the civil engineering sector and the increased attention on environmental concerns and sustainable development.

This thesis introduces an approach for the simultaneous optimization of steel space frame structures' size, shape, and topology. The study's originality stems from the specification of the objective function, which takes into consideration environmental issues by integrating the Life Cycle Assessment method in addition to conventional mass minimization. More specifically, the ideal number of elements, in terms of beams and nodes, has been investigated based on manufacturing and practical considerations.

Additionally, the structural buckling verification, which is the most problematic type of instability for steel structures to control, has been incorporated into the OF.

The introduction of structural optimization techniques' fundamental concepts and the simultaneous understanding of the LCA methodology with their respective applications in construction works served as a foundation of this work. In Chapter 2, an in-depth review of the recent literature on environmental structural optimization is presented. To appropriately examine the structural typology in a subsequent phase, the major theoretical case study has been studied and depicted in Chapter 3. First, a brief description of space frame structures has been provided, highlighting the key characteristics, issues, and civil engineering applications. Afterwards, the effectiveness of the software and the parametric design method were covered. In an attempt to go closer to the case study's primary highlights, a summary of the design variables taken into consideration has been presented and outlined in detail, along with the model's description and any pertinent analysis choices. This initial phase,

which focuses on fully understanding the behavior of such internally hyperstatic structures, aims to optimize the structure only by minimizing the total mass and to determine the best clustering strategy. The efficiency of the developed structure and the suggested objective function were analyzed. After a testing phase on a theoretical level, the methodology has been upscaled and applied to a real-case study, i.e. an industrial building with a single storey in Chapter 4. Both gravitational and lateral loads have been considered to create a model with sufficient accuracy. The environmental formulation of the OF is now covered and discussed in terms of both internal tool development and data collecting. The numerical outcomes for the industrial building's size, shape, and topology optimization have been provided in Chapter 5. To demonstrate how the findings of this study might inspire other innovations, and more especially to build a more sophisticated tool in the future to integrate environmental considerations in the early design phases, potential future advances for such analysis have been outlined in Chapter 6.

Contents

List of Figures

List of Tables

Chapter 1

Introduction

Although the optimization problem dates back centuries, it was only with the advent of computer-aided engineering software and their ability to carry out increasingly complex tasks that this discipline truly advanced. While the optimization issue has made significant academic progress, the same cannot be said for the professional world, where it encounters considerable opposition. The lack of specialized software for conducting computerized design optimization studies in civil engineering is the primary cause of the professional sector's skepticism toward optimization techniques (2018). However, certain criteria must be met to achieve the optimal result. Within the area of civil engineering, optimization can be carried out at each stage of a project's life cycle, including planning, building, operation, and maintenance, even if, however, the highest potential lies in early decision-making.

Due to the substantial quantity of CO_2 and other Greenhouse Gases (GHG) emissions in the civil engineering sector - 40% of total $CO_2eq.$ on a global level (2022) - and the growing focus on environmental issues and sustainable development, lowering environmental impacts has recently become another important goal of structural optimization.
Buildings' effects on the environment are measured in terms of energy use or GHG emissions and, according to the European Union (EU), buildings are specifically to blame for 36% of its $CO_2eq.$ emissions and 40% of its energy use. Just the residential sector accounts for 25,4% of the total energy consumed in the EU (2019).

Starting with the preliminary "Energy Performance of Buildings Directive" (EPBD), also known as European Directive 2002/91/EC (2003), significant measures were

taken in the EU to enhance the energy efficiency of the building stock. This document has had a historic effect because it created the first integrated strategy in EU history that established obligatory energy improvements in the case that buildings or building parts were retrofitted. After some years, the EPBD recast, also known as Regulation 2010/31/EU, outlined new guidelines and objectives. This latter has made it possible to make progress toward more stringent and minimal standards for the energy efficiency of newly constructed and renovated European structures (2019).

It is generally accepted that the optimization of a building during the design/refurbishment phase can be defined as the search for the set of features (design) or interventions (refurbishment) on the building envelope and building installations, such as Heating, Ventilation, Air Conditioning (HVAC) systems, and possibly on the energy sources, whose combination gives the minimum of the objective function of the optimization problem. However, there is a significant quantity of energy required for the building's construction and disposal, commonly referred to as the building's *embodied energy*, which is neglected in favor of the energy consumptions that occur during the building's use phase, known as the operational component (2019). While EPBD's other initiatives led to national legislations of buildings in terms of operational energy performance, there is still a lack of requirements for total lifecycle emissions, including embodied emissions.
Life Cycle analyses (LCA, LCC, LCEA, LCSA, LCWE, etc.) can be integrated into optimization problems for the assessment of economic, environmental, and social impacts over the whole building lifecycle (production stage, operational stage and end of life). Embodied energy and impacts derived by materials as well as the energy used at the building site during construction, its renovation, and End-of-Life (EoL - demolition and recycling) are combined.

Therefore, it is essential to deal with that class of environmental optimizations which, instead of quantifying the environmental impact through the use of energy, uses, e.g., $CO_2eq.$ emissions as a parameter. Indeed, this method is frequently combined with the Life Cycle Assessment (LCA) European procedure (2006a). Lifecycle assessment (LCA) can be used to investigate the environmental effect of a product or the purpose that the product is intended to perform. In the European context, such international standards have been also specified for the building sector

(2011, 2022).

By describing the mathematical formulation of optimization issues and providing the necessary terminology to better understand how the LCA approach operates, this introductory chapter will be concluded. In the next chapters, the thesis is developed.

1.1 Mathematical formula of optimization problems

In general, mathematical optimization (or mathematical programming) is a branch of applied mathematics that studies techniques for determining the maximum and minimum points of an *Objective Function* (OF) by altering the values taken by the variables. The general form of an optimization problem can be defined as follows:

$$Min/Max : f(x)$$

where x is typically a vector $= [x_1, x_2, ..., x_n]$ and represents a set of *design variables*, in which n is the number of design variables; $f(x)$ is the objective function.
Most engineering optimization problems have physical bounds (lower and upper bounds) as external dimension limits for structures, and the issue is constrained by equality and inequality *constraints*, which restrict the values taken by the variables to the feasibility space (2021). These bounds are usually in the form of:

$$g_i(x) \leq 0, i = 1, 2, 3, ..., m$$

$$h_j(x) = 0, j = 1, 2, 3, ..., l$$

where $g_i(x)$ and $h_j(x)$ represent, respectively, inequality and equality constraints and m and l are the number of constraints.

Two macro-categories can be identified: *single-objective* and *multi-objective*. Since the emphasis is on the decision variable space, the Pareto optimum solution is unique in single objective optimization problems. The multi-objective optimization method extends the idea of optimization by enabling single objectives to be optimized at the same time, resulting in a set of trade-off solutions that are considered equally optimal.

Optimization problems and algorithms can be classified using a multitude of factors. Depending on the optimization objectives, the OFs of single or multi-objective strategies can be expressed in terms of cost, structural performance, and environmental impact.

Ultimately, based on the design analyzed variables, structural optimization can be organized into three types of analysis (2021):

- *Size optimization* is a design technique that uses the cross-sectional areas of structures or structural components as design variables.
- *Shape optimization* uses structure nodal coordinates as design variables.
- *Topology optimization* concentrates on how nodes or joints are linked and sustained, to remove unnecessary structural elements to achieve the best design possible.

1.2 LCA framework

The term "Life Cycle Assessment" (LCA), as previously mentioned, refers to a methodology for describing the potential environmental effects of a product or service throughout its entire life cycle. The stages from the extraction of raw materials through production, usage, end-of-life, recycling, and disposal are included in the so-called "cradle-to-grave" life cycle of a product (2006a, 2006b).

The ISO standards 14040 (2006b) and 14044 (2006a) outline the framework and calculation rules of LCA and offer principles for performing LCA analyses. An LCA study is developed in accordance with the standards using the following four steps: *goal and scope definition*, *inventory analysis*, *impact assessment*, and *interpretation* (see Figure 1.1).

The goal and scope of the study are established in the first phase. By describing the intended use, the motivations for the study's design, and the intended audience, the purpose is made clear. The scope should be clearly defined to guarantee that the study's depth and breadth are appropriate for the stated purpose. The scope includes the product system under investigation, its features, the functional unit, the system boundary, allocation procedures, impact assessment methodology, data

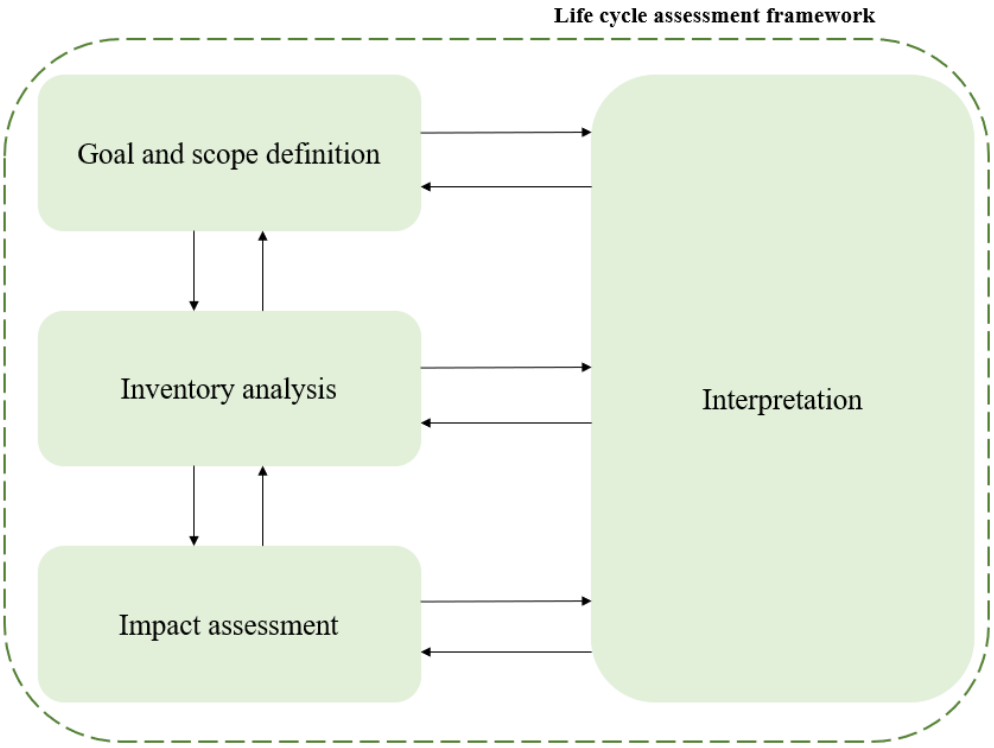

Figure 1.1: Life Cycle Assessment framework (adapted from ISO 14040 2006b)

requirements, assumptions, limitations, data quality requirements, report type, and format, and, if necessary, the critical review (2006a).

The data for the significant inputs and outputs for each unit process inside the system boundary are gathered and connected to the previously established functional unit in the second phase, known as the life cycle inventory analysis phase (LCI). The smallest element taken into account in the life cycle inventory analysis for which input and output data are quantified is referred to as a unit process (2006b). For each unit process, the inputs and outputs related to energy, raw materials, auxiliary inputs, products, co-products, waste, and releases to air, water, and soil are examined. Data validation and correlation with the functional unit and unit process are all included in the computation of data (2006a).

Impact category	Indicator	Unit
Climate change - total[1]	Global Warming Potential total (GWP-total)	kg CO_2 eq.
Climate change - fossil	Global Warming Potential fossil fuels (GWP-fossil)	kg CO_2 eq.
Climate change - biogenic	Global Warming Potential biogenic (GWP-biogenic)	kg CO_2 eq.
Climate change - land use and land use change	Global Warming Potential land use and land use change (GWP-luluc)	kg CO_2 eq.
Ozone Depletion	Depletion potential of the stratospheric ozone layer (ODP)	kg CFC 11 eq.
Acidification	Acidification potential, Accumulated Exceedance (AP)	mol H^+ eq.
Eutrophication aquatic freshwater	Eutrophication potential, fraction of nutrients reaching freshwater end compartment (EP-freshwater)	kg CPO_4 eq.
Eutrophication aquatic marine	Eutrophication potential, fraction of nutrients reaching marine end compartment (EP-marine)	kg N eq.
Eutrophication aquatic terrestrial	Eutrophication potential, Accumulated Exceedance (EP-terrestrial)	mol N eq.
Photochemical ozone formation	Formation potential of tropospheric ozone (POCP)	kg NMVOC eq.
Depletion of abiotic resources - minerals and metals	Abiotic depletion potential for nonfossil resources (ADP-minerals&metals)	kg Sb eq.
Depletion of abiotic resources - fossil fuels	Abiotic depletion potential for fossil resources (ADP-fossil)	MJ, net calorific value
Water use	Water (user) deprivation potential, deprivation-weighted water consumption (WDP)	m^3 world eq. deprived

Table 1.1: Core environmental impact indicators (adapted from EN 15804 2022)

The Life Cycle Impact Assessment (LCIA) converts the corresponding materi-

[1]The total GWP is the sum of:

- GWP-fossil,
- GWP-biogenic,
- GWP-luluc.

als and consumed energy evaluated previously in the LCI into understandable impact indicators. These indicators express the severity of the contribution of the impact categories to the environmental load. For example, impacts on the ecological environment can include global warming, ozone layer depletion, eutrophication, acidification, and others (Table 1.1). In LCIA, these definitions refer to an impact category. Each impact category is afterward quantified through an environmental indicator. In a LCIA, after the selection of the impact categories to be included in the analysis, there is the assignment of LCI outputs results to an impact category. For instance all GHG emissions ($CO_2, CH_4, etc.$) will be assigned to the Climate Change impact category. Finally, each emission is characterized. Based on simple linear models developed to predict an equivalent indicator value as a function of an emission, characterization factors are derived. If an emission is multiplied by a characterization factor, an equivalent indicator value is obtained. In the case of Climate Change and Global Warming Potential, all indicators are converted in $kgCO_2eq.$ (see Table 1.1)(2006a) (2022).

The results of the impact assessment are analyzed during the interpretation step. Important concerns are recognized, completeness, sensitivity, and consistency are assessed, and findings, limits, and suggestions are shown (2006a).

1.2.1 LCA in the building sector

The LCA technique outlined in ISO 14040 and 14044 is typically applicable across each sector. The LCA approach for buildings and building products is outlined respectively in the European Standards EN 15978 (2011) and EN 15804 (2022). EN 15804 provides Core Product Category Rules (PCR) for Environmental Product Declarations (EPDs) of building products or services; while EN 15978 outlines a method for calculating a building's environmental performance. The latter offers guidelines for reporting and communicating outcomes, and it applies to both new and existing buildings undergoing rehabilitation and retrofit work. The following steps make up the assessment's procedure:

- Determination of the assessment purposes (goal and intended use);
- Definition of the subject of the evaluation (functional equivalent, time frame for the reference study, system boundaries, and building model with physical

characteristics);

- Selection of data (building quantification, use of EPDs);
- Computation of environmental indicators (methods for calculating and aggregating concerns about the environment, effects, and issues);
- Report and communication of results;
- Verification;
- Completion of assessment.

In accordance with EN 15978, information on building products is required for the evaluation at the building level and, for this purpose, Environmental product declarations (EPDs) are an important source.

According to EN 15978 and EN 15804, the modular framework of buildings' life cycle stages is defined as in Figure 1.3.

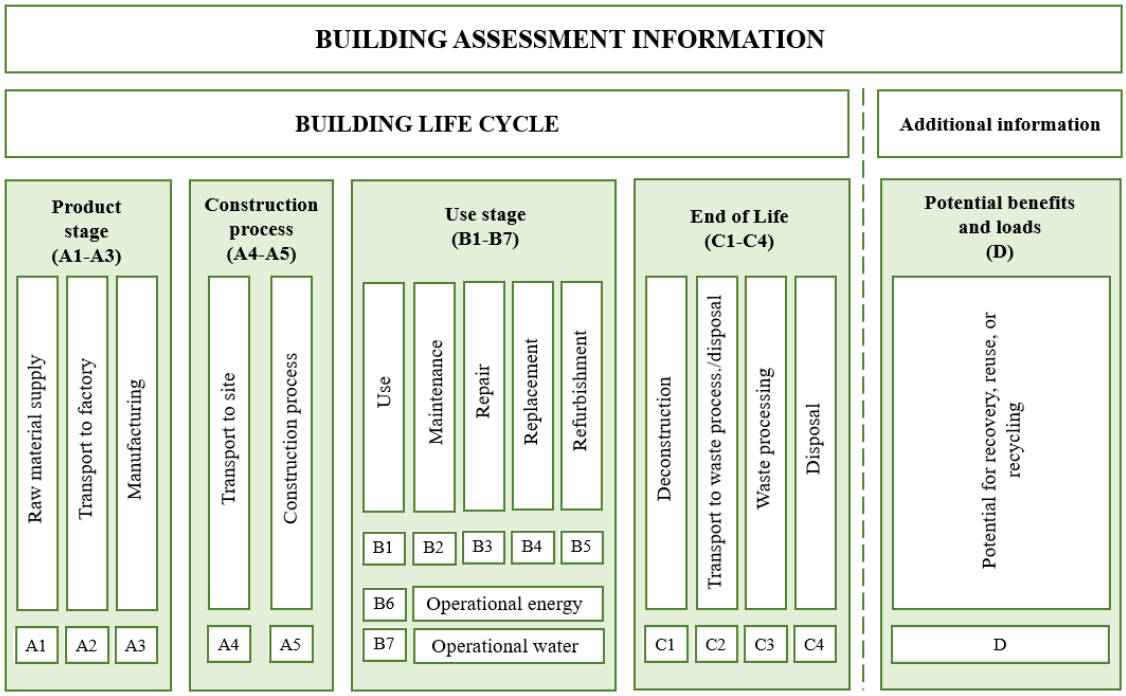

Figure 1.2: Life cycle stages of a building (adapted from EN 15978 2011)

The *product stage* is described in modules A1 to A3, which also include the extraction of raw materials (A1), transportation of resources to the manufacturing

site (A2), and production of construction goods (A3). These modules are regarded as being "cradle to gate" within the system boundaries. The transport of material, supplies, and equipment to the construction site (A4 and A5), as well as the actual construction activity (A5), are included in the stages of the construction process (A4 and A5).

The *use stage* (B1 to B7) includes the time between the end of construction and the building's deconstruction and/or dismantling. It is separated into the phases of usage of the building products and services (B1), maintenance (B2), repair (B3), replacement (B4), and refurbishment (B5). The replacement module (B4) consists of all the steps required to replace a building component at its specific end of service life with a new one, by restoring the initial functional, technical, and aesthetic quality of the building component (2022).
Repair (B3) should be interpreted as the replacement of a damaged component or a single portion due to vandalism or unexpected events. On the other hand, B4 ought to be given the assignment for the replacement of a whole building component. A refurbishment (B5) is a major change of an entire building section: it involves measures in which replacements and retrofit are occurring to enhance the overall building's technical performance.
The energy and water utilized during the use stage are taken into consideration in modules B6 and B7.
The *end-of-life stage* (C1-C4) addresses the effects of waste processing (C3), disposal (C4), waste transport (C2), and deconstruction (C1). The *environmental burdens and advantages* of reuse, recovery, or recycling are measured in module D.

According to EN 15804, environmental effects from modules A1 to A3, C1 to C4, and D must be estimated in all EPDs. All modules that are being considered must use the established indicators. Indicators for the description of resource usage (*input-related indicators*) and indicators for the description of environmental consequences (*output-related indicators*) are distinguished in EN 15804.
Each specified life cycle module must take into account the core indicators given in Table 1.1. If necessary, additional indicators can be declared. These later ones include indications for resource utilization, which each life cycle module must take into account. Information on waste classifications, output flows, and biogenic carbon content must also be included.

It might take a lot of time and effort to gather and evaluate data on how much energy and what kind of construction materials are used. When all necessary data was available in the past, LCA was frequently utilized as a post-design examination of buildings, such as when applying for a sustainable building certification (Rock et al. 2020). However, LCA should be used during the early design process to improve a building's environmental profile.

Based on the planning process phase, the EeBGuide (2015) organizes LCA studies into three categories based on the various degrees of detail that can be seen in the development of a building project: *screening*, *simplified*, and *complete* LCAs. The time and effort needed for LCA increase as the quality of the data does (see Figure 1.3). In the early stages of design, when precise data might not yet be available, a design engineer can quickly and easily do a screening LCA to assess design options. When more precise data is available, a comprehensive LCA can be used at a later stage of the construction process.

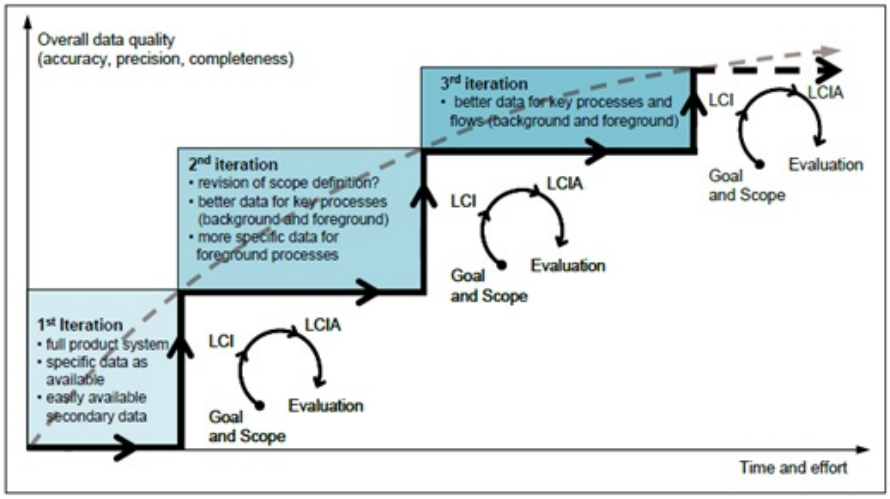

Figure 1.3: LCA as an iterative process (taken from the EeBGuide 2015)

Chapter 2

State of Art - Environmental Optimization Strategies

This Chapter presents an overview of the most potential methods used for environmental optimization.

It is essential to note that in the context of energy optimizations, the prior categories have been interpreted differently. As mentioned in Chapter 1.1, size optimization typically involves the sizing, and thus the choice of typology, of HVAC systems according to the amount of energy consumption and the degree of thermal comfort that is desired and needed; this achievement of indoor thermal equilibrium is frequently combined with the need to design openings (*envelope* optimization) of favorable size and with convenient thermal properties to balance heat gains and losses. The latter ones include losses through external walls and the ones resulting from ventilation. On the other hand, heat gains are due to solar radiation through the windows. The difference between losses and gains represents the amount of energy that must be provided by the installed heating system.
Clearly, the issue of window sizing is insufficient to yield an optimum solution. As a result, shape optimization, often in conjunction with size optimization, employs the orientation of the building as a design variable in order to maximize the structure's exposure to sunlight during the day and during the cold and temperate seasons.
Azimuth and *Window-to-Wall Ratio* are the parameters that show the most commonly in literature. The azimuth is defined as the angle formed by true North and

a line drawn from one location to the Sun. This angle changes as the Sun moves across the sky during the day, making it critical to properly orient, for example, solar panels and optimize their performance. The window-to-wall ratio, on the other hand, is a measure of the amount of window area on a building in relation to the total amount of exterior wall area and it can be differentiated for exposure.
Finally, similar considerations made for shape optimization are worthwhile in terms of topology optimization. Topological environmental optimizations have been discussed in the literature as a strategy to attain a certain architectural appeal of the optimal structure (2002b).

It has been noted that most of the research in the literature focuses on case studies of composite or reinforced concrete structures, with little focus on pure steel ones. To find a strategy that is also applicable to the latter, it has been discovered that in optimizations that use CO_2 equivalent emissions (or the Global Warming Potential, GWP) as an environmental indicator, the Objective Function is frequently presented as the sum of the product between construction and emission units. Quite often, instead of emission units, the cost of greenhouse gas emissions is found, which represents the monetary value of environmental damage caused by greenhouse gases emissions linked to the building. Typically, these data are acquired either from discrete national or regional databases or product-specific data sets with the support of professional LCA software.

2.1 Size optimization

Most of the papers identified in the literature belong to the size optimization category. In particular, numerous studies regard multi-objective optimizations that minimize costs and environmental indicators simultaneously.
The environmental effects of buildings are measured in terms of CO_2 equivalent emissions and energy use, which, as a matter of fact, correspond to the first groups of papers reported afterward.
Moreover, among size optimization, LCA-implemented strategies have been highlighted.

2.1.1 CO_2 emissions and embodied energy

Over a 50-year period, the structural frame of a building accounts for 20–30% of the total whole lifecycle GHG emissions. In addition to financial benefits, the employment of optimization techniques in the creation of a structural design can lower the consumption of materials whose extraction, fabrication, and transportation cause significant environmental harm.

As cross-section optimization is the most feasible type of optimization, several studies look either at the frame structures or at column/beam elements to evaluate the carbon and cost savings that may be obtained without modifying the floor system and the beam arrangement. Indeed, according to Drewniok et al. (2020), for an assumed 60-year lifespan, mass reductions of 35% in the steel structure can result in up to 5% total-life carbon savings. The authors developed a tool called The Lightest Beam Method (LBM), which selects the lightest beam from a concrete catalog of Universal Beams (UB) in line with European design regulations. According to each design constraint, the tool minimizes the needed section mass and then indicates which constraint is influencing the member. The reductions from steel floor beam optimization can range between 17% and 35% of the frame's initial embodied carbon. The research of Paya-Zaforteza et al. (2009), instead, outlines an approach for designing reinforced concrete (RC) building frames with a minimum amount of costs and of embedded CO_2 emissions, incorporating two single-objective functions optimized by a Simulated Annealing (SA) algorithm. The emissions of the building frame materials and costs are computed similarly by multiplying unit values and measurements of the materials. The Institute of Construction Technology of Catalonia's 2007 database was utilized to get the unit emissions for the study's concrete, steel, and formwork materials. When cost rather than emissions was the goal, the comparison of the solutions revealed a maximum 3.38% increase in CO_2 emissions. On the other hand, CO_2 solutions might raise the price by a maximum of 2.77%. These results support the hypothesis that both objectives were quite coincident and provide comparable results. Since prices are more susceptible to changes in market values than emissions, which depend on industrial processes, the CO_2 target function looks to be also more robust and environmentally favorable. In a similar way, other authors (e.g. Kaveh et al. 2017, Arpini et al. 2021, Camp et al. 2013, Park et al. 2014 and Santoro et al. 2020) performed optimizations using

discrete national databases for unit emissions and costs applied both to materials and construction units. In particular, Guimarães et al. (2022) formulated a design problem of concrete-filled composite columns with different types of sections. Steel was shown to be the most expensive and least eco-friendly material across all scenarios, accounting for more than 80% of the cost and emissions in columns without reinforcement and more than 70% in all other cases. Furthermore, longitudinally reinforced columns had reinforcing steel as the second most costly material, while concrete had the greatest CO_2 effect. Comparably, Yeo et al. (2015) and De Medeiros et al. (2014) performed a design optimization based on the CO_2 footprint of reinforced concrete (RC) structures and made an economic comparison with basic cost optimization. In the research of Yeo et al., the two single-objective functions were computed as the homogenized volume of the structure, obtained by using cost and CO_2 footprint ratio coefficients, which were simply the ratios of the cost/CO_2 footprint of steel and the one of concrete per cubic meter, multiplied by the cost and CO_2 footprint of concrete per cubic meter. The CO_2 footprint is reduced by 5% to 15% by optimizing the design to achieve the lowest possible carbon emissions. On the other hand, De Medeiros et al. suggested ways to reduce the environmental costs associated with the section of rectangular reinforced concrete columns utilizing the Harmony Search heuristic approach. The following environmental costs associated with reinforced concrete inputs are taken into account: carbon dioxide (CO_2), equivalent carbon dioxide (CO_2e), or global warming potential (GWP), energy consumption, and environmental scoring units, also known as Eco indicator. The optimized monetary solutions were likewise more favorable in terms of the environment, leading to the overall conclusion that the reduction of environmental costs is directly tied to the optimization of monetary costs.
An interesting and peculiar application on modular building systems (MSBs) was developed by Gatheeshgar et al. (2020). This type of system offers the benefits of high productivity, improved structural performance, and quicker construction times, and it is a practical answer for areas with rising housing demand. MBS may minimize the operating energy required in buildings due to its highly insulating and airtight design, helping to fulfill the rising need for environmentally friendly structures.

In the matter of tall buildings, a parametric research on environmental assessment was conducted by Mavrokapnidis et al. (2019) to compare five distinct cost-

optimized tall building typologies. The cross-sectional dimensions of structural elements serve as the design variables in the optimization problem. Then, a Life Cycle Assessment (LCA), also referred to as "cradle to grave", was conducted on the five cost-optimized outcomes to compare the various environmental profiles across tall structure typologies. The LCA computes the environmental effect from the acquisition of each material to the disposal and recycling. When comparing structural systems made of concrete and steel, it can be relieved that the latter needs approximately twice as much energy and produces twice as much CO_2 as concrete-based systems. However, steel constructions are most widely employed due to structural efficiency even if it has been demonstrated, through this study, that concrete works well for tall buildings, up to 60 stories.

The embodied energy content of buildings has drawn the attention of research, as well as the embodied carbon emissions, derived from industrial processes of building materials. In the study of Lagaros (2018) two actual test cases are illustrated, a high-rise building and an athletic stadium. For the high-rise structure, an environmental benefit of 11.2% and 12.7% in terms of energy consumption and Greenhouse gas (GHG CO_2 equivalent) emissions was achieved. The embodied energy is calculated as the sum of the initial embodied energy of design, which is a function of the quantity of building material and its unit energy content, and the recurring embodied energy, which is likewise a function of the structure's and material's life span.

Consequently, the realization of sustainable future designs relies heavily on reducing the embodied energy of building materials. In the work of Whitworth et al. (2020) a Matlab algorithm is presented to optimize a composite beam for tall structures for five different objective functions. The amount of material multiplied by the cradle-to-gate energy content of the material per unity quantity added to the energy utilized on-site for construction will be used to quantify only the initial embodied energy of the structure, which results to be reduced for each of the OFs.

The attention of various authors has been drawn to bridges, one of the most important civil engineering structures. However, because of the numerous design variables that characterized the structural problem, building a sustainable bridge is challenging.

To cover these difficulties, the study of Penadés-Plà et al. (2019) proposed the

use of metamodels, in particular the Kriging one, and of a simulated annealing (SA) algorithm. The structure under examination was a concrete box-girder pedestrian bridge and its design variables were the depth of the cross-section, the bottom slab and web inclination width, the top slab and external cantilever thickness, and the bottom slab and web slab thickness. This problem involves a single-objective optimization of the embodied energy of the structure, used as a representative criterion of its environmental impact. The embodied energy is computed as the summation of each unit of energy, obtained from the BEDEC ITEC database of the Construction Technology Institute of Catalonia, multiplied by the measured values of each element. Simple and combined solicitations, cracking, compression and tension stresses, and vibration are all structural constraints to check the serviceability and ultimate limit states (SLS and ULS). In terms of the best solution, the comparison demonstrates that Kriging raises the optimal energy by 2.54%.

Several multi-objective optimizations were proposed to demonstrate the strict relation between costs and CO_2 emissions in bridges' case studies. The objective functions were computed similarly for emissions and for costs, as unit emissions/prices multiplied by construction units. The values of CO_2 emissions for materials were taken from the same database of the previous single-objective problem also for Yepes et al. (2015) and Garcìa-Segura et al. (2016). In the case of Martínez-Muñoz (2022), a cradle-to-gate analysis for each unit of material multiplied by the amount of material used is performed for emissions' computation.

Also costs are acquired from discrete databases, such as the BEDEC ITEC one, or from surveys of precast structure constructors and subcontractors and updated to current values.

Metaheuristic methods, in particular, have done well in handling complex Steel–Concrete Composite Bridges (SCCBs) optimization. For example, in Yepes et al. (2015) a hybrid glow-worm swarm optimization (SAGSO) method is employed to combine the synergy effect of local search with simulated annealing (SA) and global search with glow-worm swarm optimization (GSO); while, in Martínez-Muñoz (2022), a hybrid k-means discrete (KMDA) approach that combines the Sine Cosine Algorithm (SCA), the Cuckoo search algorithm (CS), and the k-means unsupervised learning methodology were adopted.

Structural and safety (ULS and SLS) constraints imposed by advice from experts

and standards (CEN Eurocodes) are placed on the bridge design process as well as the problem's geometry and constructability criteria.
From these three studies, similar results have been obtained. In particular, it turned out that CO_2 emissions and cost are tightly associated. Specifically, a euro decrease in cost translates into a 1.75 kg reduction in CO2 emissions (2015). As long as cost and CO_2 emission criteria result in a decrease in material consumption, the results demonstrate that cost optimization is a solid strategy for achieving an environmentally friendly design.; when emissions are decreased, however, it does not always follow that costs are also optimized. This has to do with the fact that whereas material types vary in price, emissions are the same.

LCA implementation Implementing LCA as a method for planning environmentally acceptable buildings, and retrofittings that use less energy are commonly recognized as the most economical approach to reduce the environmental impact of buildings. They are also seen as a possible opportunity to make a substantial contribution to this cause. As a result, enhancing the energy efficiency of existing structures while limiting extra CO_2 emissions and costs has emerged as a critical issue and challenge in minimizing the life cycle effect of buildings. The case study building examined in Schwartz et al. (2016) is a recently refurbished council housing complex in Sheffield (UK). Two objective functions were minimized: the life cycle carbon footprint (LCCF) and the life cycle cost (LCC). The LCCF (kgCO_2) was computed as the summation of embodied carbon per material and the operational energy-related carbon (OERC), which is obtained by multiplying the predicted energy consumption values by the CO_2 emissions of the fuel. Similarly, LCC was calculated. The findings suggest that the best models have envelope components that reduce OERC or operating costs more than they do. For instance, the best models avoided using brick as an insulating layer and had the fewest windows possible because these materials cost more than the OERC or the money they save.
Similarly, the goal of the study of Mostavi et al. (2017) was to create a multi-objective design optimization model that would reduce life cycle costs and emissions (Global Warming Potential, GWP) while maximizing occupant satisfaction (thermal comfort) in a typical small office building in Pennsylvania (USA). This study revealed that making wise choices early in the design process might help designers

produce the best sustainable designs.
In the research of Van Cauteren et al. (2022), instead, the environmental life cycle assessment (E-LCC) and life cycle cost analysis are combined in two case studies of hybrid (steel/timber) truss structures. The findings demonstrate that any intermediate Pareto optimum design is a hybrid steel/timber structure in each situation. According to this, a hybrid steel/timber structure seems to be the best option for a designer who is focused on a sustainable building but constrained by the available financial means.
Other problems' formulations based on a combination of LCA and discrete structural optimization were given by Brütting et al. (2018, 2020a and 2020b). The author suggested looking into truss structures that were planned and built using reused materials that were selected from stocks of pre-existing supplies to significantly minimize material consumption and waste created by the construction industry.

2.1.2 Energy consumption

Building design must balance two basic yet opposing goals: energy usage and indoor climate. Even for highly experienced engineers, finding a design that fully exploits a situation while fulfilling both of these goals is difficult because of the enormous amount of factors and techniques involved. Global optimization methods, like genetic algorithms, can be used to greatly reduce energy usage while keeping a comfortable indoor environment (2010). Building envelopes make up the barrier separating a structure from the outside world, and their construction really determines the building's future energy needs for heating and cooling, which has a significant impact on how the structure behaves thermally. A multi-objective decision model proposed by Diakaki et al. (2010) enables the examination of a potentially infinite number of alternative measures and evaluates them by a set of criteria, such as the building's annual primary energy consumption, its annual carbon dioxide emissions, and the initial investment cost. Choices are made about space heating, cooling, and hot water distribution systems based less on their generating efficiency and more on the release of CO_2 emissions. The categories of systems with fewer CO_2 emissions are therefore favored, and from these categories, the systems with the highest generating efficiencies are chosen.
On the other hand, for retrofitting buildings, the research of Antipova et al. (2014)

is based on the combined application of multi-objective optimization and LCA concepts. It considers two objective functions: an environmental one, expressed as the total environmental impact associated with the quantity of natural gas and electricity used for space heating and cooling and water heating; and an economic indicator quantified by the total cost which includes the retrofit and operation (energy) cost. The retrofit measures contribute to a 10.7% decrease in the overall effect of the minimal environmental impact solution. This reduction is made possible by a 4% reduction in the impact of electricity and a 68% reduction in the impact of natural gas.

A process for applying sustainable design principles to both new construction and building retrofits has been outlined by Brunelli et al. (2016), in which five objectives have been identified: minimization of thermal energy consumption, electric energy consumption, Net Present Value (NPV) of the investment, emissions of CO_2, and maximization of comfort level.

Frequently, researchers in literature face the particular problem of optimal sizing of windows in a building to optimize lighting, heating, and cooling performances. This issue is typically dependent on climate, as in the single-objective optimization of Caldas and Norford (2002). The structure is investigated under two different locations, Phoenix and Chicago, and the problem was dependent also on the glazing used, the orientation of windows, and the type of use of the building. The objective function was expressed as annual energy consumption, which was computed as the sum of the energy spent in heating and cooling and the lighting energy. Suga et al. (2010), instead, proposed a multi-objective research for a window format that optimizes the lighting environment, energy consumption, initial cost, and draft (natural ventilation) performance, while maintaining a constant thermal environment.

Few studies have been recorded that compare the ideal envelope design with those specified in standards and regulations, taking into account the three Es: energy, economics, and environment. The study of Al-Saadi and Al-Jabri (2020) uses a life cycle cost (LCC) analysis in conjunction with the EnergyPlus simulation tool to optimize envelope design for houses in hot regions of Oman. This research also recommended solutions derived from regional thermal codes. As expected, design scenarios based on tight code requirements have a lower environmental effect.

A new multi-stage framework, instead, is proposed by Ascione et al. (2017), called

CASA. The recommended packages of energy retrofit measures (ERMs) are chosen using a multi-objective genetic algorithm (MOGA), which minimizes primary energy consumption (PEC), thermal discomfort hours (DH), and global cost for energy uses during building lifetime (GC). This approach provides significant benefits for both the private, as building lifespan expenses are reduced, and the public, as energy consumption and building environmental effects may be drastically reduced. For example, a decrease of around 14.3 tCO2-eq/a is achieved. On the other hand, Flager et al. (2009) evaluated the potential of Process Integration Design Optimization (PIDO) technologies to support more successful Multidisciplinary Design Optimization (MDO) processes in the Architecture, Engineering, and Construction (AEC) industry. Using MDO techniques integrated into PIDO software, some civil engineering sectors have surmounted comparable constraints, resulting in a shortened design cycle and better product performance.
Another interactive optimization framework built on MATLAB is created by Li et al. (2017) to make it easier to create performance optimization solutions. Using computer simulations and a basic building energy model, a performance comparison of three optimization strategies has been done. Three functions are chosen as the optimization application's objectives of a typical residential building in China: the total percentage of cumulative time with discomfort (TPMVD) over the whole year, the life cycle cost (LCC) corresponding to the total amount of costs during the building's lifespan and, the total carbon dioxide equivalent (CO_2-eq) which is the summation of the CO_2-eq emissions of each material and the electricity CO_2-eq emissions.

In the academic and professional worlds, interest in low-energy and zero-energy buildings is also growing. The EPBD defines two particular categories of Zero-Energy Buildings (ZEB), called "nearly-Zero Energy Buildings" (nZEB) and "Net-Zero Energy Buildings" (NZEB). In a ZEB, the actual yearly supplied energy for building operation is less than or equivalent to the on-site renewable exported energy, measured on a source energy basis. These structures are intended to work with less overall greenhouse gas impact on the environment than traditional structures.

It is feasible to see how literary studies differ based on the type of developed method (one article examines both single and multi-objective algorithms) (2015). The collection of works that uses multi-objective optimization, which is frequently

favored to single-objective algorithms, is unquestionably the most prevalent. The intricacy of a building's energy optimization is brought to light by this orientation.

When it comes to multi-objective optimizations, heuristic algorithms are used the most frequently, with the Non-dominated Sorting Genetic Algorithm predominating (NSGA II).

Another insightful analysis focuses on the following variables for the building's optimization:

- the building envelope (including the use of PCMs, the form and direction of the structure, and the walls, roofs, and layers' thermophysical characteristics) (e.g. Gilles et al. 2017, Ascione et al. 2016);
- Fixtures (window and door thermal characteristics, glass emissivity) (e.g. Ascione et al. 2016);
- HVAC and equipment (air conditioning systems, energy storage);
- Renewable Energy Sources (RES) plants (solar collectors, PV, wind turbines, bio-diesel generators) (e.g. Lu et al. 2015).

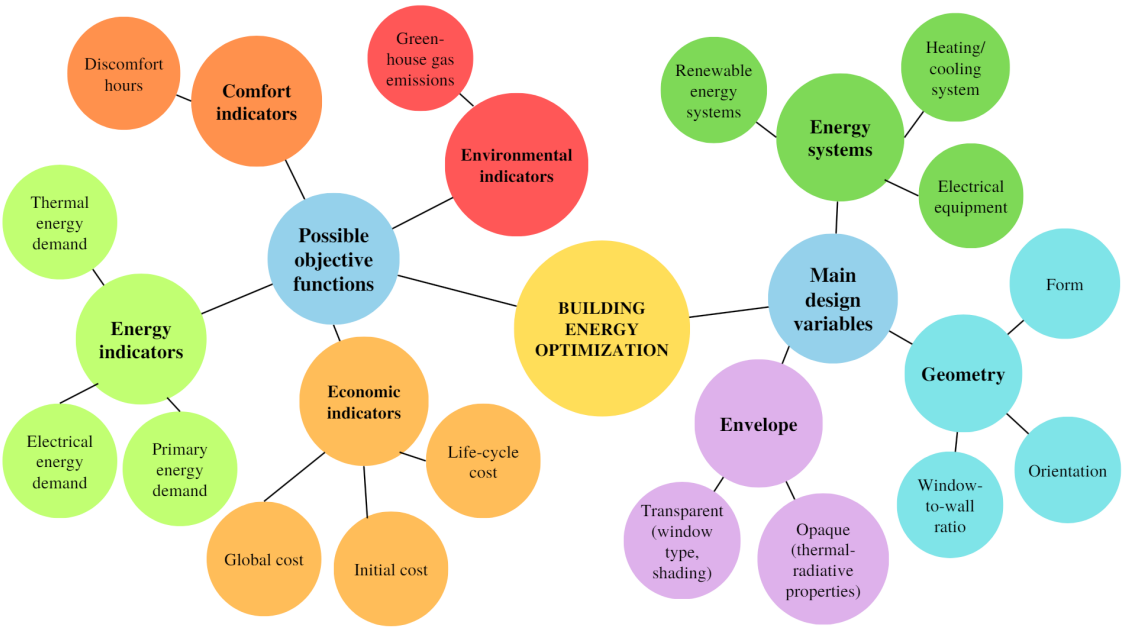

Figure 2.1: Building energy optimization: possible objective functions and main design variables.

Moreover, regarding the need for a global approach for ZEB, many performance indicators should be taken into account, including cost (Life cycle cost, LCC), thermal comfort, embodied energy, CO_2 emissions, energy usage, output of renewable energy sources, and durability (as in Gilles et al. 2017, where these main classes of objective functions were simultaneously analyzed).

Therefore, it is likely that the building industry is evolving toward sophisticated, robust optimization techniques that use a variety of criteria, many disciplines, and meta-models established through appropriate adaptive design of trials. Life cycle approaches emerge logically as a result of the decrease in yearly consumption, which has underlined the importance of taking into account the embodied energy related to building. When optimizing the design of ZEBs under these circumstances, the life cycle should be taken into consideration.

2.2 Shape optimization

It has been observed that shape optimization study tends to focus primarily on the issue of energy usage. Many studies fulfill the size optimizations as hybrids, as stated in the opening of the same Chapter 2, in order to best combine the energy, aesthetic, and functional requirements of the case studies.

2.2.1 Energy consumption

Because the building shape controls the size and orientation of the external envelope exposed to the outside environment, it may impact building performance in a variety of ways, including energy efficiency, cost, and aesthetics.

As the environmental implications of buildings are recognized, it becomes increasingly important to include environmental performance in building design. Green construction is a new design concept that demands the consideration of resource depletion and waste emissions over its whole life cycle. The building life's phases investigated are natural resource extraction, building material production, on-site construction, operation, and transportation associated with the aforementioned phases. Two studies of Wang et al. (2005a) and (2006) employed exergy as an environmental parameter to overcome common issues in the optimization process. The amount of work that a system can accomplish when brought into thermodynamic equilibrium

with its surrounding environment is known as *exergy*. The evaluation of exergy is dependent on both the status of the system under study and the circumstances of the reference environment, and it may be included in Life Cycle Assessment (LCA) to solve natural resource depletion characterization and valuation difficulties. The optimization models were set to minimize both life cycle cost (LCC) and life cycle environmental impact (LCEI). Using LCEI as an indicator for life cycle environmental performance, the optimization issue may be simplified by combining all examined impact categories into a single objective function. In particular, in the study of Wang, Rivard, and Zmeureanu, the study's variables were divided into four categories: shape (orientation, edge length, and bearing), structure (building structural system), envelope configuration (wall and roof types and layers) and overhang, which is a passive solar architectural feature put over windows to prevent direct solar radiation through the windows in the summer.
An alternative solution is proposed by Tuhus et al. (2010) to find a minimum optimized solution for four different cost functions (annual electricity use, annual gas use, annual total energy cost and life-cycle cost) to the problem of residential buildings envelope energy efficiency. Different building shapes were considered, including the rectangle, L-shape, T-shape, H-shape, U-shape, cross and trapezoid. The functions were optimized using the aspect ratio (ratio between width and height), the orientation and two characteristic shape parameters (normalized concerning width or height) for each configuration through a genetic algorithm (GA). It was found that the trapezoid and rectangle were consistently the best shapes. However, the reference square design offers the lowest life-cycle costs across all climates when all building envelope parameters are permitted to vary.

A high-performance, sustainable structure has been defined in modern buildings as one that uses the least amount of energy during each of the four major phases of a building's lifetime: material manufacture, construction, usage and maintenance, and end-of-life. Since many classic optimization approaches have only found limited application, the research of Brown et al. (2016) focuses on multi-objective optimization (MOO), which prioritizes structural efficiency and operational energy efficiency applied on three case studies of structures with long-span roofs (the enclosed arch of the Montreal Olympic stadium, the "PI" cantilever overhang of Suvarnabhumi Airport and the "x-brace" cantilever overhang of Qingdaobei Station). The goal

of structural optimization was to reduce the amount of steel necessary; while, energy optimization aimed to reduce the yearly operational energy of the building, which includes needs for lighting, heating, and cooling. Similarly, an intriguing multi-objective optimization was proposed by Quaglia et al. (2014) to minimize both structural performances and energy efficiency of an origami-inspired deployable shelter for military and disaster relief housing use. In particular, the Lever Shelter Module (LSM) was analyzed, which is made up of sandwich panels constituted by two fiber-reinforced polymer (FRP) rigid faces and a foam lightweight core. Two objective functions were formulated: the structural one was a deflection function computed as the maximum between the deflection in any direction of the two modules under self-weight, wind, and snow; the energetic one, instead, was the total thermal energy load for the modules obtained as the sum of heating and cooling loads. The design variables were constrained by demanding that the shelter can be packaged on a 463L pallet interfacing with Tricon containers. When compared to the minimal deflection result, the multi-objective optimization demonstrates a 12% reduction in thermal energy load while only marginally increasing deflections. It also demonstrates a considerable reduction in deflections when only increasing the thermal energy load by 12% compared to the minimal thermal energy load result.
A novel technique, called agent-based, was also explored by Yi and Malkawi (2009) to control building shapes by creating hierarchical relationships between geometry points. The agent-based representation begins with the establishment of hierarchical relationships between points (nodes) that represent and regulate the geometry. Three distinct major points are required: the center point, the agent point, and the child point. The center point acts as a pivot between agent and child points, while the agent point defines the position of the child ones. Lastly, child points are the points that control a surface, which construct the building form. The objective function minimized the heat flow between indoor and outdoor spaces, including targets, surface heat flow, heat gain, heat loss and volume.

Size and Shape Massive energy savings may be realized throughout the operational stages by implementing passive and active tactics. According to certain research, increased operational energy savings led to exponential increases in embodied energy. Over 45% of the lifespan energy in low-energy buildings might be attributed

to embedded energy usage, therefore from a lifecycle viewpoint, the embodied energy could outweigh the operating energy savings. It is consequently essential to reduce operational energy consumption while maintaining embodied energy performance. The optimal design of several building envelopes with local materials typical of climatic conditions in Africa's Sub-Saharan area was investigated in the study of Ansah et al. (2021). In the first step, the building geometry and renewable energy are optimized and used as the foundation to design the building model for assessing the trade-off between embodied and operational energy with different façades in the second stage. Similarly, depending on climate, Echenagucia et al. (2015) proposed an integrated strategy for the first phases of building design. The energy required to heat, cool, and light a case study was minimized by varying the number, position, shape and type of windows and the thickness of the masonry walls. The results of the search process can give designers important information that will help them make better-informed decisions. For instance, designers can choose the objective function they want based on the environment and the HVAC system they have chosen.

Several papers discuss multi-objective optimizations exploited in three sectors: the optimization of the building envelope to reduce Heating, ventilation and air conditioning (HVAC) usage as well as construction costs, the optimization of building form (windows sizing and positioning), and the optimization of HVAC system design and operation (e.g. Caldas and Norford (2003), Negendhal and Nielsen 2015, Wang et al. 2005b and Raphael 2011). In particular, the study of Marks 1997 aimed to optimize the dimensions of a structure with known volume and height in order to minimize building and annual heating costs. The problem is formulated in two ways, by making as first an optimization of a building of an arbitrary shape and secondly of a building on polygonal plans, both solved numerically by a computer system, called CAMOS. As a consequence of optimizing the design of the structure, construction and heating costs over the N-year period can be reduced by several to several dozen percent. Likewise, due to the enormous number of interactions between the elements that contribute to the overall behaviour of a structural solution, also the reasearch of Caldas et al. (2003) benefits from the use of computer simulations (DOE-2.1E) for the case study of the Alvaro Siza's School of Architecture. The use of this new generative system (GS) that combines a search technique (GA) and DOE-2.1E

showed that it may be used to change building geometry to make it better suited to its environment. Although the GS made several adjustments to each façade of the building, which may have resulted in a better-balanced use of daylighting, the building's overall artificial lighting usage did not decrease significantly. However, a significant gain in terms of heating and natural lighting is recognized due to the crucial role played by the overhangs: decreasing its depth results in greater beneficial south sun absorption in the winter and reduces heat loss sources simultaneously. An innovative comprehensive framework for building energy design, called Harlequin, has been suggested by Ascione et al. (2019). Because each façade can have a variable composition and thermal-radiative qualities depending on the exposure, the obtained solutions are called "Harlequin buildings". As a result, the proposed architectural solutions are referred to as "Harlequin" buildings because of how irregular their color and composition are, which is evocative of the well-known figure "Harlequin". The three objective functions to be minimized are: the annual percentage of discomfort hours over occupied hours (DH), the annual electrical energy demand for artificial lighting (EEDL), and the annual thermal energy demand for space conditioning (TEDSC). Depending on the chosen solution, considerable decreases in primary energy consumption (PEC), global cost (GC), and CO2-eq emissions can be made in comparison to a reference design. The maximum reductions are 12.3 kg/m^2 for CO_2-eq, 43.9 $kWhp/m^2$ for PEC, and 63.9 $/m^2$ for GC.

2.3 Topology optimization

The study revealed that the topology optimization's literature is still in urgent need of refinement. Pure topology optimization examples are completely absent from the current study, but few examples from hybrid optimization categories are provided.

Size and Topology The emphasis recently placed on reducing operating energy consumption has made it more crucial than ever to take into account building's embodied carbon. The research of Ching and Carstensen (2022) offers a two-material truss topology optimization technique to lower the designed structure's Global Warming Potential (GWP). Optimization occurs gradually and step by step. The first one is a hybrid typology and size optimization, applying only structural re-

strictions to timber and steel individually. The result is the ideal outcome of a stiffer framework made of steel only. The second stage restricts the admissible stresses of wood only and the structure by the environmental parameter GWP, resulting in an ideal construction made entirely of wood. The optimization again leads to a building made entirely of steel in the following phase, which keeps the environmental constraints in force but this time takes into account realistic values for stresses. The GWP ultimately limits the issue, and the stresses are changed to make steel and wood operate in tension and compression, respectively. The latter scenario results in a mixed optimum structure that enables to lower the GWP levels. The stress conditions in the materials must therefore be suitably adjusted in order to see a minimum increase in terms of environmental effect. The author recommends conducting the same analyses while taking into consideration a full LCA that also takes into account the transportation phases in order to balance the significant difference between structural (stiffness) and environmental (GWP) constraints.

Size, Shape and Topology In the study of Mensinger and Huang (2017) the preliminary structural design of a set of rectangular steel composite office buildings was done using a multi-objective optimization of costs and environmental impact. The cost is obtained by multiplying the weight of materials by their unit prices; while, the second one is called Environmental Product Declaration (EPD) and it is computed as a weighted summation of the Global Warming Potential (GWP), the Ozone Depletion Potential (ODP), the Photochemical Ozone Creation Potential (POCP), the Acidification Potential (AP), the Eutrophication Potential (EP) and the Primary Energy, both non-renewable (PEne) and renewable (PEe). The data related to these environmental criteria were taken from the Ökobaudat platform, which is a German standardized database for ecological evaluations of buildings. The outcomes of the optimization against the EPD value and the costs are the same or quite comparable.

Table 1 Literature review of environmental optimization strategies

Ref.	Year	**S**tatic **D**ynamic	Size	Shape	Topology	**S**ingle/**M**ulti Objective	ID-OF	Design criteria	Design variables
Marks et al.	1997	-	☑	☑	☐	**M**	Construction cost Annual heating cost	Geometric bounds	Building's form Wall geom. Window geom.
Caldas et al.	2002	**S**	☑	☐	☐	**S**	Annual energy consumption	Geometric bounds	Window geom.
Coley et al.	2002a	-	☑	☑	☑	**S**	Energy use	-	Wall geom. Roof geom. Window position Building form Building orientation
Caldas et al.	2003	-	☑	☑	☐	**S**	Annual energy consumption	Openings geom.	Window geom. Roof geom.

Table 1 Literature review of environmental optimization strategies

Ref.	Year	**S**tatic **D**ynamic	Size	Shape	Topology	**S**ingle/**M**ulti Objective	ID-OF	Design criteria	Design variables
Caldas et al.	2003	-	☑	☑	☐	**M**	Materials cost Annual energy consumption	Layer's material	Window geom. Window position Building geom.
Wang et al.	2005a	-	☐	☑	☐	**M**	Life cycle cost Life cycle environmental impact	Geometric bounds Glazing	Window geom. Window type Building orientation Envelope
Wang et al.	2005b	**S**	☑	☑	☐	**M**	Life cycle cost Life cycle environmental impact	Geometric bounds Layer's material Overhang depth	Window type Building orientation Building shape Envelope

Table 1 Literature review of environmental optimization strategies

Ref.	Year	**S**tatic **D**ynamic	Size	Shape	Topology	**S**ingle/**M**ulti Objective	ID-OF	Design criteria	Design variables
Wang et al.	2006	-	☐	☑	☐	**M**	Life cycle cost Life cycle environmental impact	Geometric bounds Window type	Window geome. Window type Building orientation Building shape Structural system Envelope Overhang depth
Flager et al.	2009	**S**	☑	☐	☐	**S/M**	Structural cost Energy cost	Geometric bounds Daylight performance	Cross-section Building orientation Building geom. Window-to-wall ratio
Paya Z. et al.	2009	**S**	☑	☐	☐	**S**	Materials cost Embedded CO_2 emissions	Limit states	Cross-section Material type

Table 1 Literature review of environmental optimization strategies

Ref.	Year	**S**tatic **D**ynamic	Size	Shape	Topology	**S**ingle/**M**ulti Objective	ID-OF	Design criteria	Design variables
Yi et al.	2009	-	☐	☑	☐	**S**	Heat flow indoor/outdoor	Geometric bounds Conduction, radiation, convection performance	Building form
Magnier et al.	2010	-	☑	☐	☐	**M**	Thermal comfort Energy consumption	Geometric bounds Heating/cooling performance	Envelope Window geom. HVAC system
Suga et al.	2010	-	☑	☐	☐	**M**	Glass cost Energy consumption Uniformity Draft performance	Daylight performance Uniformity on desk surface	Window geome. Glass type

Table 1 Literature review of environmental optimization strategies

Ref.	Year	**S**tatic **D**ynamic	Size	Shape	Topology	**S**ingle/**M**ulti Objective	ID-OF	Design criteria	Design variables
Tuhus et al.	2010	-	☐	☑	☐	**S**	Annual total energy cost Life cycle cost Annual electricity use Annual gas use	Geometric bounds	Aspect ratio Orientation Building geom.
Raphael	2011	-	☑	☑	☐	**M**	Cost Solar thermal load Lighting energy	Geometric bounds	Window geometry Shade dimensions
Camp et al.	2013	**S**	☑	☐	☐	**S**	Material cost CO_2 emissions	Geometric bounds Capacity checks Reinforcement ratio Deflection	Cross section Reinforcement area

Table 1 Literature review of environmental optimization strategies

Ref.	Year	**S**tatic **D**ynamic	Size	Shape	Topology	**S**ingle/**M**ulti Objective	ID-OF	Design criteria	Design variables
De Medeiros et al.	2014	**S**	☑	☐	☐	**S**	Cost CO_2 emissions Equivalent CO_2 emissions Global Warming Potential Eco indicator	Geometric bounds Reinforcement rate	Cross-section Reinforcement area
Antipova et al.	2014	**S**	☑	☐	☐	**M**	Total cost Total environmental impact	Type selection	Window type Solar panels type Envelope
Quaglia et al.	2014	**-**	☐	☑	☐	**S/M**	Deflection function Total thermal energy load	Geometric bounds	Wall geom. Roof geom.

Table 1 Literature review of environmental optimization strategies

Ref.	Year	**S**tatic **D**ynamic	Size	Shape	Topology	**S**ingle/**M**ulti Objective	ID-OF	Design criteria	Design variables
Park et al.	2014	**S**	☑	☐	☐	**S**	Material cost CO_2 emissions	Geometric bounds Reinforcement ratio Capacity checks	Cross section Material strength Reinforcement diameter
Yeo et al.	2015	**S**	☑	☐	☐	**S**	Materials cost CO_2 footprint	Serviceability Strength	Cross-section Reinforcement area
Yepes et al.	2015	**S**	☑	☐	☐	**M**	Materials cost CO_2 footprint	Limit states	Cross-section Reinforcement area
Lu et al.	2015	-	☑	☐	☐	**S**/**M**	Total cost CO_2 emissions Grid interaction index	Geometric bounds Power performance	Renewable energy systems dimensions

Table 1 Literature review of environmental optimization strategies

Ref.	Year	**S**tatic **D**ynamic	Size	Shape	Topology	**S**ingle/**M**ulti Objective	ID-OF	Design criteria	Design variables
Echenagucia et al.	2015	-	☑	☑	☐	**M**	Energy for heating, cooling, lighting	Geometric bounds	Window type, shape, position Glazing Wall thickness
Negendahl et al.	2015	-	☑	☑	☐	**M**	Capital cost of the façade Energy use Thermal overheating Daylight	Geometric bounds	Façade geometry Plan geometry
Brunelli et al.	2016	**S**	☑	☐	☐	**M**	Net Present Value of investment Thermal energy consumption CO_2 emissions Comfort level	Power performance Energy performance	Building footprint Renewable system Electric system Installation variables

Table 1 Literature review of environmental optimization strategies

Ref.	Year	**S**tatic **D**ynamic	Size	Shape	Topology	**S**ingle/**M**ulti Objective	ID-OF	Design criteria	Design variables
García-S. et al.	2016	**S**	☑	☐	☐	**M**	Materials cost CO_2 emissions	Limit states	Cross-section Material strength
Schwartz et al.	2016	**S**	☑	☐	☐	**M**	Life cycle cost Life cycle carbon footprint	Geometric bounds	Window type Envelope
Ascione et al.	2016	**-**	☑	☐	☐	**M**	Heating load Cooling load	Hours of discomfort	Window-to-wall ratio Glazing Envelope
Brown et al.	2016	**-**	☐	☑	☐	**M**	Embodied and operational energy	Geometric bounds	Roof geometry
Kaveh et al.	2017	**S**	☑	☐	☐	**S/M**	Materials cost CO_2 emissions	Geometric bounds Strength	Cross-section Material strength Reinforcement area

Table 1 Literature review of environmental optimization strategies

Ref.	Year	**S**tatic **D**ynamic	Size	Shape	Topology	**S**ingle/**M**ulti Objective	ID-OF	Design criteria	Design variables
Mostavi et al.	2017	**S**	☑	☐	☐	**M**	Life cycle cost Life cycle emission Thermal comfort	Geometric bounds Material selection	Envelope Door type Glazing system
Li et al.	2017	**S**	☑	☐	☐	**M**	Life cycle cost Total percentage of cumulative time with discomfort Equivalent CO_2 emissions	Geometric bounds Material selection	Envelope Window geom. Building azimuth
Ascione et al.	2017	-	☑	☐	☐	**M**	Global cost Primary energy consumption Thermal discomfort hours	Geometric bounds Operative performance	Envelope HVAC system Building geom.

Table 1 Literature review of environmental optimization strategies

Ref.	Year	**S**tatic **D**ynamic	Size	Shape	Topology	**S**ingle/**M**ulti Objective	ID-OF	Design criteria	Design variables
Gilles et al.	2017	-	☑	☐	☐	**M**	Life cycle cost Primary energy consumption CO_2 emissions Thermal comfort Compliance for hot water Boiler operating cycles Hours in solar collector	Geometric bounds Operative performance	Envelope Heating system
Mensinger et al.	2017	**S**	☑	☑	☑	**S**	Materials cost Environmental Product Declaration	Geometric bounds	Cross-section Slab thickness

Table 1 Literature review of environmental optimization strategies

Ref.	Year	**S**tatic **D**ynamic	Size	Shape	Topology	**S**ingle/**M**ulti Objective	ID-OF	Design criteria	Design variables
Lagaros	2018	**S**	☑	☐	☐	**S**	Materials cost Equivalent CO_2 emissions Energy consumption	Geometric bounds	Cross-section Slab thickness
Brütting et al.	2018	**S**	☑	☐	☐	**S**	Mass minimization Cut-off mass Embodied energy	Geometric bounds Buckling Stress capacity Deformation bounds Assignment of available stock elements	Cross-section
Penadés-P. et al.	2019	**S**	☑	☐	☐	**S**	Embodied energy	Limit states Cracking Stress Vibration	Cross-section Slab and web geometry

Table 1 Literature review of environmental optimization strategies

Ref.	Year	**S**tatic **D**ynamic	Size	Shape	Topology	**S**ingle/**M**ulti Objective	ID-OF	Design criteria	Design variables
Mavrokapnidis et al.	2019	**S**	☑	☐	☐	**S**	Materials and construction cost CO_2 emissions	Eurocode requirements Geometric bounds	Cross-section
Ascione et al.	2019	**-**	☑	☑	☐	**M**	Life cycle global cost Investment cost Equivalent CO_2 emissions Primary energy consumption	Geometric bounds Performance Type selection	Building geometry Envelope Energy systems
Gatheeshgar et al.	2020	**S**	☑	☐	☐	**S**	-	Eurocode requirements Geometric bounds	Cross-section Moment capacity

Table 1 Literature review of environmental optimization strategies

Ref.	Year	**S**tatic **D**ynamic	Size	Shape	Topology	**S**ingle/**M**ulti Objective	ID-OF	Design criteria	Design variables
Whitworth et al.	2020	**S**	☑	☐	☐	**M**	Structural optimizations Embodied energy	Limit states	Cross-section Shear and moment capacity
Drewniok et al.	2020	**S**	☑	☐	☐	**S**	-	Limit states Vibration Deflection	Cross-section Shear and moment capacity
Al-Saandi et al.	2020	**-**	☑	☐	☐	**S**	Life cycle cost Annual energy consumption	Regional guidelines Climate influence	Envelope Glazing Window-to-wall ratio
Santoro et al.	2020	**S**	☑	☐	☐	**S**	Material cost CO_2 emissions	Geometric bounds Brazilian standard checks	Cross section Reinforcement area

Table 1 Literature review of environmental optimization strategies

Ref.	Year	**S**tatic **D**ynamic	Size	Shape	Topology	**S**ingle/**M**ulti Objective	ID-OF	Design criteria	Design variables
Brütting et al.	2020a	**S**	☑	☐	☐	**S**	Mass minimization Cut-off mass GHG emissions	Geometric bounds Stress capacity Deformation bounds Assignment of available stock elements	Cross section
Brütting et al.	2020b	**S**	☑	☐	☐	**S**	Mass minimization Cut-off mass Environmental impact	Geometric bounds Stress capacity Deformation bounds Assignment of available stock elements	Cross section

Table 1 Literature review of environmental optimization strategies

Ref.	Year	**S**tatic **D**ynamic	Size	Shape	Topology	**S**ingle/**M**ulti Objective	ID-OF	Design criteria	Design variables
Ansah et al.	2021	-	☑	☑	☐	**M**	Photovoltaic power generation Embodied energy Operational energy	Geometric bounds Climate influence	Building orientation Window-to-wall ratio Envelope Window type HVAC system Photovoltaic system
Arpini et al.	2021	**S**	☑	☐	☐	**S**	CO_2 emissions	Brazilian standard checks	Slab dimensions Formwork type Profile dimensions Degree of beam-slab interaction

Table 1 Literature review of environmental optimization strategies

Ref.	Year	**S**tatic **D**ynamic	Size	Shape	Topology	**S**ingle/**M**ulti Objective	ID-OF	Design criteria	Design variables
Martínez-M. et al.	2022	**S**	☑	☐	☐	**M**	Materials cost CO_2 emissions	Limit states Eurocode requirements	Cross-section Material strength
Guimarães et al.	2022	**S**	☑	☐	☐	**M**	Materials cost CO_2 emissions	Brazilian standard checks	Cross-section Moment of inertia Plastic section modulus
Ching et al.	2022	**S**	☑	☐	☑	**S**	Compliance Global Warming Potential	Geometric bounds Stress	Cross-section
Van Cauteren et al.	2022	**S**	☑	☐	☐	**M**	Life cycle cost Environmental Life Cycle cost	Geometric bounds	Cross-section

Chapter 3

Case study 1: Space frame roof

3.1 Structural typology: Space frame

Space structures — also known as space frames or space frame structures — are truss-like, materially effective, rigid constructions made of beams (two-force members) joined at nodes.

The Paris Universal Exposition served as a turning point for an important evolution in structural design, and so the history of this structural typology began with the technical and innovative resonance that happened between the XIX and XX centuries. When **Alexander Graham Bell** developed his ground-breaking prototype aircraft frame designs, based on the tetrahedron and introducing the first rod-node connections, he had no idea that numerous spatial truss configurations would eventually be the subject of patent applications.

Since the 1950s, **Richard Buckminster Fuller** has made a significant contribution to industrial prefabrication, particularly with regard to three-dimensional buildings, in an effort to simplify the geodesic domes of his design.

Throughout the ensuing ten years, studies on new joint systems and their application to fundamental geometries were being conducted by **Konrad Wachsmann** at the University of Southern California, and this has sparked a great deal of interest in space structures from some of the most renowned architects and academics. The *Mero-Trigonal* node, which is still one of the most widely sold systems in the world today, was then invented by **Max Mengeringhausen**. Furthermore, the Frenchman **Stephane Du Chateau**'s Spherobat method was used to build a variety of

constructions.

The ability to merge science and technology with the economy, markets, and profit has only been conceivable in the modern era. This happened due to the introduction of new procedures for creating space systems, new methods for creating nodal connections, and the scientific organization of new calculation and verification codes related to the advancement of computer capabilities.

These frames are utilized in engineering designs for a variety of purposes, including industrial structures, warehouses, bridges, exposition halls, stadiums with great span distances, shopping complexes, and airports. On average, the structure's skeleton is visible as in the Stansted Airport (Foster + Partners) in London (UK) and the Palau Sant Jordi (Arata Isozaki) in Barcelona (ES).

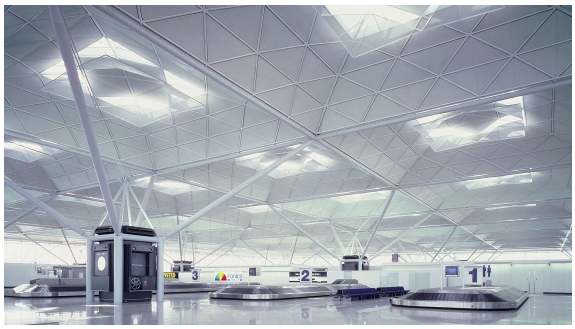

Figure 3.1: Stansted airport structural system

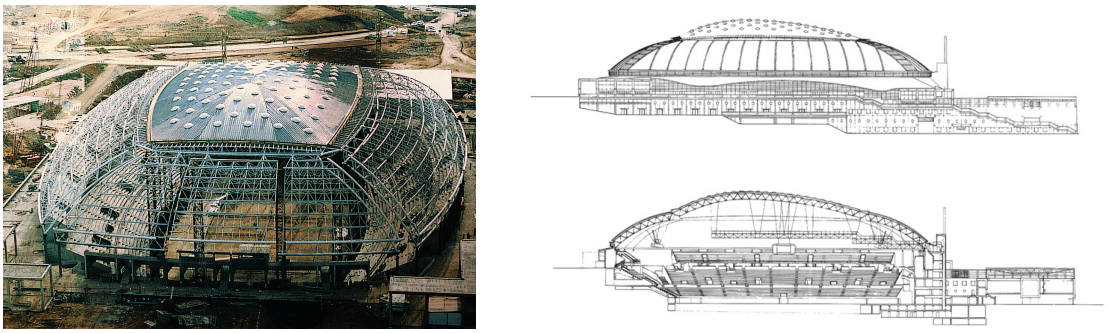

Figure 3.2: Palau Sant Jordi sporting arena structural system

Whereas space structures are frequently used in architectural construction as statically supporting structures that mimic planned geometric shapes or support desired freeform surfaces (Jiang et al. 2017), they are hidden in many notable structures. For instance, the Heydar Aliyev Cultural Center in Azerbaijan, built by

Zaha Hadid, has an underlying space structure as can be seen in Figure 3.9.

Figure 3.3: Heydar Aliyev Cultural Center underlying structural system

For the creation of roofing load-bearing structures, the spatial reticular system therefore appears to be the most suited among the current systems for a number of reasons, including the following:

- a highly standardized, high-quality production that is totally prefabricated in the workshop;
- the assurance of high precision on site due to the extremely low manufacturing tolerances;
- the development of reticular systems that are extremely near to theoretical designs and that significantly reduce parasitic effects.

Different systems can be distinguished under the definition of "space frame" based on two grouping strategies (2020):

1. **Curvature classification**
    - *Spherical domes.* Tend to need a lot of support, either from outside of the construction or via the use of additional pyramidal or tetrahedral modules inside the structure.
    - *Barrel vaults.* Normally does not need any additional support of the sort mentioned above, but it does have a cross section as an additional source of inner support.

- *Space plane covers.* A structure made up of several planar supporting structures which act as plates. The diagonals support the entire structure, and the horizontal bars sustain the weight.

2. **Arrangement classification**

- *Triple-layered grid.* The three levels of the space frame components are parallel to one another. Structures are flat and connected by diagonal bars.
- *Double-layered grid.* Diagonal bars connect two levels of elements that are parallel to one another.
- *Single-layered grid.* A single layer of elements that make up the structure's surface.

Due to its flexibility and semi-automatic control of the design and manufacturing phases of the rods and nodes, the spatial reticular system enables the creation of thousands of individually unique and distinctively different geometries that would otherwise be unachievable. Particularly, steel's spatial reticular structures are distinguished by their high expressive and compositional flexibility as well as their capacity to evenly distribute stresses on individual rods and on external restraints.

3.1.1 Conditions of equilibrium

Six conditions of static equilibrium may be found for a three-dimensional structure at each location in the structure and at each support. These are the six statics equations:

$$\sum F_x = 0, \sum F_y = 0, \sum F_z = 0 \tag{3.1}$$

$$\sum M_x = 0, \sum M_y = 0, \sum M_z = 0 \tag{3.2}$$

When six external restraints are imposed on a three-dimensional structure, it is considered to be externally determinate because the six equations of static equilibrium may be used to predict these restraints.

In a pin-jointed three-dimensional space frame with i nodes, including the supports, $3j$ equations of equilibrium may be derived, since each node provides the

relationships:

$$\sum F_x = 0, \sum F_y = 0, \sum F_z = 0$$

Reticular structures may be viewed from a static-kinematic perspective as a collection of points materials (internal hinges) with three degrees of freedom (two in the plane), connected by rods that govern their distance from one another and, as a result, each represents an internal pendulum constraint. The system is then prevented from moving when it is conceived of as a single rigid body by external constraints. Then, a reticular system is said to be isostatic (kinematically determined) if the total number of degrees of freedom, which is three times the number of nodes (two in the plane), equals the sum of the number of members, m, and the number of external constraints, r.

$$\textit{Statically determinate} \text{ when } (m + r) = 3j$$
$$\textit{Statically indeterminate} \text{ when } (m + r) > 3j$$

Then, by resolving the forces at the nodes, the member forces in a pin-jointed space frame may be determined as it is shown in Figure 3.4, where there is a total of i members with a common node *0*.

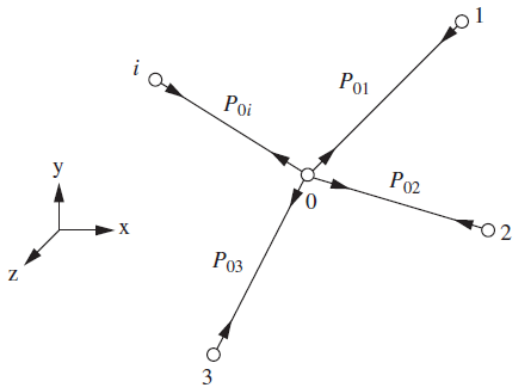

Figure 3.4: Member forces

If no external force is applied at node 0, resolving along the three coordinate axes leads to:

$$\sum P_{x0i} = 0, \sum P_{y0i} = 0, \sum P_{z0i} = 0 \tag{3.3}$$

The spatial trusses must be viewed from a static perspective as a discretization of the continuous element. A structural arrangement that relies primarily on its

resistance to bending actions is more stressed than one that relies on axial forces. All bending actions may be converted into traction or compression forces by decomposing the continuum into hinge nodes and truss components.
As previously mentioned, the choice of support devices is crucial. Indeed, the behavior of the structure can be either a plate or a beam depending on the arrangement and the typology of constraints.

The geometry of the modules that make up this structural typology is another factor that has a direct impact on the equilibrium prerequisites.
The modules of spatial reticular structures are generally composed of polyhedrons that are schematized into "rod" and "node" components. In the specific instance of this study, the module is *semi-octahedral* (see Figure 3.5, which is regarded as labile from a static point of view since one of its faces is not triangular.

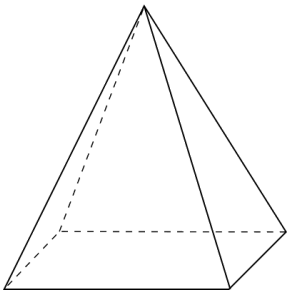

Figure 3.5: Semi-octahedral module

Figure 3.6: Double layered structure with semi-octahedral module in real structures

In this regard, a structure made up of a series of aligned semi-octahedrons with tetrahedrons interposed (Figure 3.7a), restrained externally to the end nodes, is labile because of internal constraints. In a particular load condition involving only vertical loads (Figure 3.7b), it is isostatic. On the other hand, when a structure is

made up of at least two unimodular structures placed side by side (Figure 3.7c), it becomes isostatic under any load scenario.

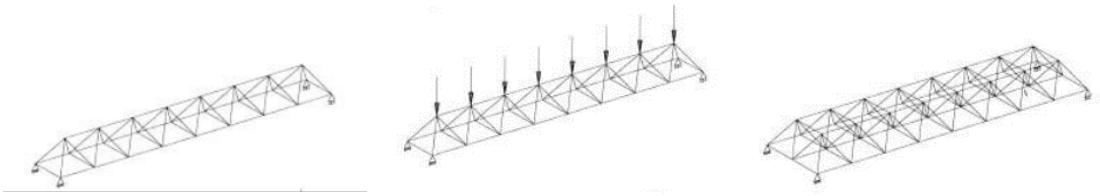

(a) (b) (c)

Figure 3.7: Isostatic and labile configurations

The chosen arrangement for the case study is shown in Figure 3.6. The space frame in a double-layer grid has greater open space between the top and bottom layers, which is advantageous for installing any kind of mechanical or electrical utility systems throughout the building. It is, therefore, well suited for industrial use. Moreover, all components of double-layer grids can only withstand tension or compression since their hinged joints have no moment torsional resistance. The effect of bending or torsional moment is negligible, even in connections built with relatively stiff joints.

3.2 Parametric design

A digital model is created using parametric modeling (also known as parametric design), which uses a set of pre-programmed rules or algorithms known as *parameters* to produce the model's elements automatically rather than manually. The ability of parametric design to capture and shape complex geometries and structures via the interplay of elements makes it one of the most highly debated design methodologies among architects and engineers worldwide.

An early example of parametric design is **Antoni Gaudí**'s model of upside-down cathedrals, in which the artist used hung ropes to form outstanding catenary arches. For the purpose of analyzing spatial relationships, **Luigi Moretti** established a series of equations in the 1960s. In 1962, he applied these equations to generate the urban plan for Rome, becoming the first architect to use the term *parametric architecture*. As an outcome, projects with outstanding innovation and structural expressiveness, such as those by **Félix Candela**, **Pier Luigi Nervi**, and **Frei Otto**,

are frequently referred to as parametric in reference to the technical calculations that played a crucial role in their development.

Parametric modeling has traditionally been utilized for fairly specific design tasks. For instance, the Beijing National Stadium, built for the 2008 Summer Olympics, utilized sophisticated parametric modeling tools to create a stadium geometry that was optimal for athletic events and would also work well as a soccer stadium after the Olympics. Similar to this, the geometry of the Shanghai Tower was created parametrically using the modeling program Grasshopper, allowing the link between shape, design, and wind to be determined. One of the several parametric structures designed by renowned architect **Frank Gehry** is the "Fish" or Peix Olímpic in Barcelona, Spain. Gehry is well-known for taking organic shapes to the next level, even developing a structure that resembles a crumpled paper bag. The most creative and prolific exponent of parametric architecture is widely recognized to be **Just Zaha Hadid** (1950–2016), a well-known architect and designer. Fluid shapes creep inside and around the architectural volumes in her projects, which include the Vitra Fire Station in Weil am Rhein (1990–1994), the Hoenheim-Nord modal interchange station in Strasbourg (1999–2001), the MAXXI Museum in Rome (2010), and the Aquatics Center of London (2007–2012). Sometimes these architectural volumes adopt geometrical configurations, but on other occasions appear more properly organic.

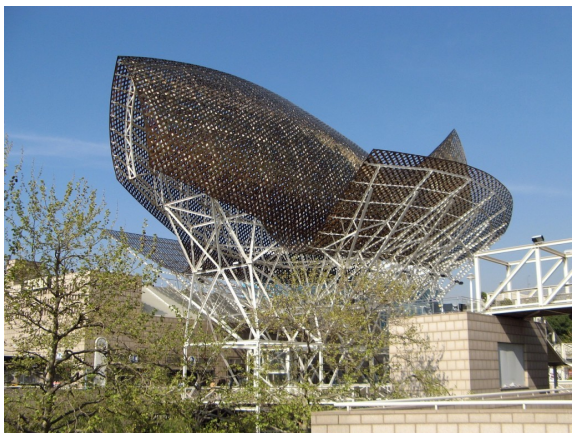

Figure 3.8: Peix Olímpic, Spain

Parametric modeling has really entered projects recently via the scripting interfaces of software packages. Examples of such software include the aforemen-

(a) Vitra Fire Station, Germany

(b) MAXXI Museum, Italy

Figure 3.9: Zaha Hadid parametric projects

tioned software Grasshopper, developed by Bentley Systems' Generative Components, Robert McNeel & Associates', and Revit Autodesk's Dynamo. The brilliant Italian architect and designer **Arturo Tedeschi**, who is also well-known for publishing works on Grasshopper modeling 2018, is another figure worth noting in this context. His body of work spans a variety of application areas, including conventional architecture and the industrial design world (furniture, vehicles, installations, products), where each project is distinguished by ostentatious and fashionable shapes.

3.2.1 Software adopted

In this thesis, a specific flow diagram was employed along with the following tools for the optimization process:

- **Rhinoceros 3D** (2010), developed by McNeel&Associates in 2008. It is a 3D modeling tool that is frequently used during the preliminary design stage. Its ability to depict extremely complex forms and structures makes it more efficient than other CAD software.
- **Grasshopper 3D**, a graphical algorithm editor tightly integrated with Rhino's 3D modeling tools which uses visual programming to parameterize geometries. The plug-ins included in the tool increase its usability and effectiveness. The following are the primary ones employed in this work:
  - **Karamba 3D** (2013), to perform Structural Finite Element Analysis (FEA) for spatial trusses, frames and shell structures;

– **LunchBox**, developed by Nathan Miller, for exploring mathematical shapes, paneling, structures, and workflow and for reading Excel data;

– **Octopus**, an optimizator for single/multi-objective problem formulations, developed by Robert Vierlinger and his team, at the University of Applied Arts in Vienna. Octopus provides two global metaheuristics techniques to obtain Pareto-optimal solutions:

  * Strength Pareto Evolutionary Algorithm 2 (SPEA2)
  * Hypervolume Reduction Algorithm (Hype Reduction)

  The population size and maximum number of generations must be properly defined. Both of them rely on the problem's complexity, particularly the ability of several solutions to exist at once and sustain many alternatives that lead to a more precise optimal solution. The method must be connected to multiple design variables that were previously created as well as to the Objective Function that has to be minimized in order to begin the optimization process.

Figure 3.10: Software employed in the research

As a result, Grasshopper was used to parametrically model the geometry of the construction. Then, it was transformed, utilizing Karamba3D components, into FEM elements while assigning cross-sections, loads, and supports. Finally, the Octopus optimizator has been coupled to the design variables and objective function. Utilizing LunchBox, LCA input data as well as optimization process outcomes have been integrated and exported.

3.3 Model definition and validation

The goal is to simultaneously optimize the size, shape, and topology of a steel space frame construction. As first, the roofing structure has been developed in a

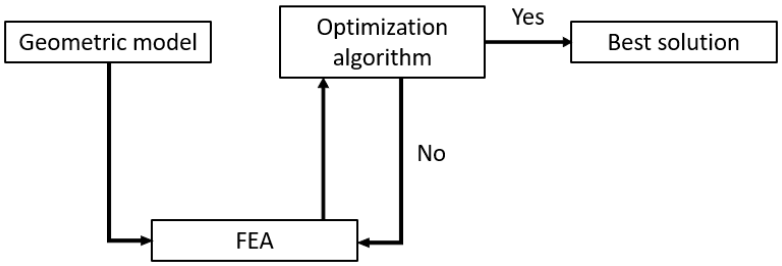

Figure 3.11: Flow diagram of the problem

parametric manner, taking into account its structural demands in terms of the best amount of components, both beams and connections, starting with a total span length of 60 meters in the x direction and of 30 meters in the y direction.

In the first phase of the work, an algorithm was implemented to enable the creation of the roof's geometry in a way that made each of its components variable, i.e., modifiable both in terms of the height of the truss, H, and of the number of elements in the x and y directions (*divisions x, divisions y*) as well as the length of the spans in the two directions (*delta x, delta y*), as a consequence.

As anticipated in section 3.2.1, the parametric modeling software Grasshopper was used to create the geometric model. Specifically, the initial step, which consisted of constructing nodes and connecting rods of the considered geometry, was accomplished using code. In practice, Grasshopper provides the option of employing the required script objects of several programming languages (Python, C++, Visual Basic), allowing for the recall of all the software's parameters and components. In this instance, it was chosen to employ the *Python* component, which was then used to create the geometric code (the script is provided in Appendix A.1).

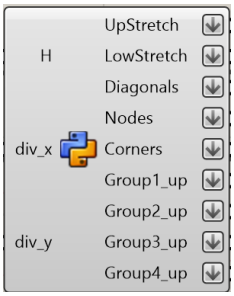

Figure 3.12: Component for Python script integration

Comparatively to the other software components, the chosen one is very flexible

and enables the designer to select the quantity and types of input parameters in accordance with the logic of the script code; as a result, the outputs obtained can also be selected arbitrarily in accordance with the desired goal.
The following design parameters, set in meters, $[m]$, have been used to generate the geometric model of the roof:

- H: truss height;
- Div_x: number of elements in x direction;
- Div_y: number of elements in y direction.

The two dimensions of the building design that are referenced in the upper layer, L_x and L_y, are fixed values that were wisely selected and stated inside the code.
The following relationships, as well as additional structural verifications, have provided bounds within which the geometric design variables have been confined:

- **Pre-dimensioning rule** for the upper bound of H

$$\frac{H}{L} = \frac{1}{15} \tag{3.4}$$

  It is computed with respect to the largest dimension of the building (L_x). For structural and constructibility considerations, a lower bound of 1 m is selected.

$$1 \leq H \leq \frac{L}{15} \quad [m] \tag{3.5}$$

- **Number of subdivisions**
  The length of the bar elements, Δ, has been restricted to the following values for structural, constructability, and assembly reasons:

$$1 \leq \Delta \leq 10 \quad [m] \tag{3.6}$$

  As a result, the following is the outcome for the number of subdivisions in the two directions:

$$\frac{L_x}{\Delta_{max}} \leq div_x \leq \frac{L_x}{\Delta_{min}} \tag{3.7}$$

$$\frac{L_y}{\Delta_{max}} \leq div_y \leq \frac{L_y}{\Delta_{min}} \tag{3.8}$$

The spherical connections between the elements are pre-dimensioned a priori with a diameter of 30 cm but are not considered in the static analysis.
Since all nodes are considered to be equal, the single node's verification and dimensioning were not of the utmost significance. The effect would thus have been the same for the purposes of determining the structural and environmental OF, but scaled by a coefficient associated with the connection's weight. The above intention is further strengthened by the usage of standardized spherical hinges, as shown in Figure 3.6. In other words, since the connections in these systems are not sized ad hoc, what matters is the quantity of connections rather than their type. The nodes' assumed diameter matches the design parameters based on experience or common practices for this kind of structures.

Instead, the results represented in Figure 3.12 are the components of the overall geometry and the groups of beams needed for the application of linear loads in a further step (see Figure 3.19):

- *UpStretch*, which contains the lines constituting the upper layer;
- *LowStretch*, which contains the lines constituting the lower layer;
- *Diagonals*, corresponding to all the diagonals connecting the two layers;
- *Nodes*, containing all the nodes in the geometry;
- *Corners*, which contain the four extreme nodes of the lower layer, corresponding to the position of the supports;
- *Group1_ up*, *Group2_ up*, *Group3_ up*, *Group4_ up*, corresponding to clusters of beams to manually impose the areas of influence for load application.

As a result, Figure 3.13 depicts how the geometry is constructed in the software, where the input parameters are variables defined through *Number sliders*; while Figure 3.14 depicts the geometry that is generated. The variables that were previously defined are detailed visually in Paragraph 3.4.1.

The next stage was to convert the lines into beam elements after the model's geometric objects had been constructed. This was done so that FEM analyses could be performed and the behavior of the structure studied.

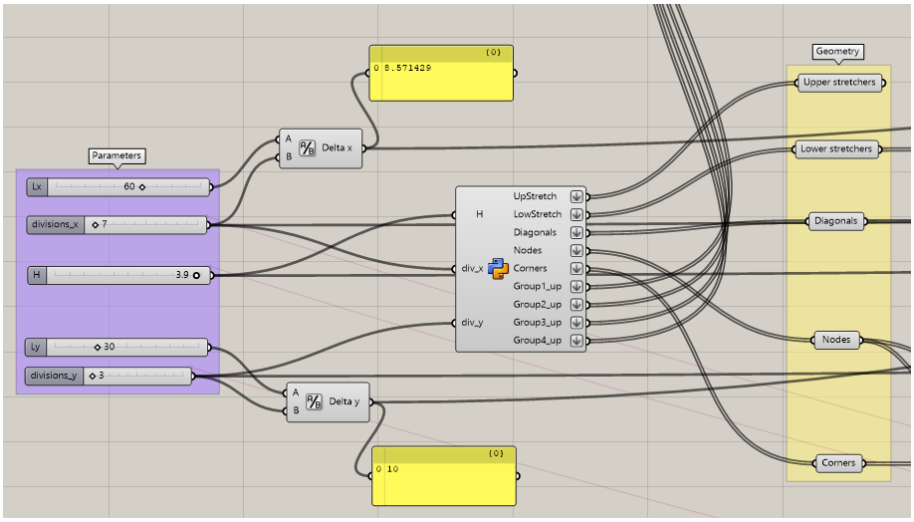

Figure 3.13: Geometry parameterization

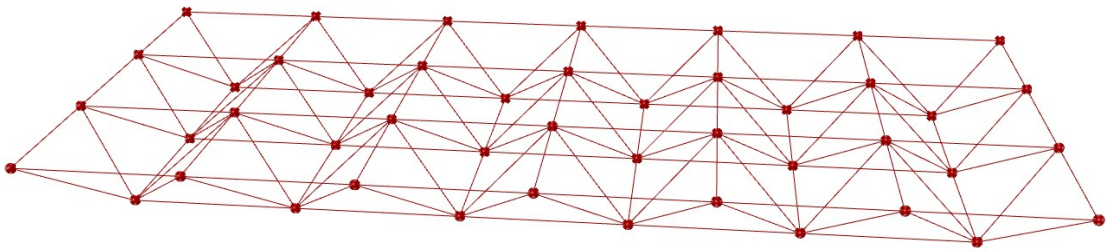

Figure 3.14: Geometric model of the structure

3.3.1 Finite element analysis with Karamba3D

Due to its quick interaction with Grasshopper and potential for lower robustness than commercial software, Karamba3D produces results that are more suited than those of other FE tools while drastically cutting down on overall computing time. The Grasshopper-created parametric model immediately sends data to the Karamba *solver*, which then sends the results of the analysis to the Optimizer.
For example, the elements made using Grasshopper's basic geometry are then transformed into FEM components and constructed by specifying the assigned cross-sections, material, joints, supports, and loads applied.

Each line element of the geometric model has, as previously mentioned, been converted into a beam element by Karamba3D using the component *LinetoBeam*. The line geometry from Grasshopper has been entered into this object, which then

transforms it into elements that may be placed as input for the *Assemble* component, which takes all the details about the components and their interactions as input and produces a model ready to perform the structural analysis.

When the *Bending* option in the LinetoBeam component is toggled to true, the rigid link works as a beam element. Releases at the start/end positions of beams are then used to define the truss components in a second step.

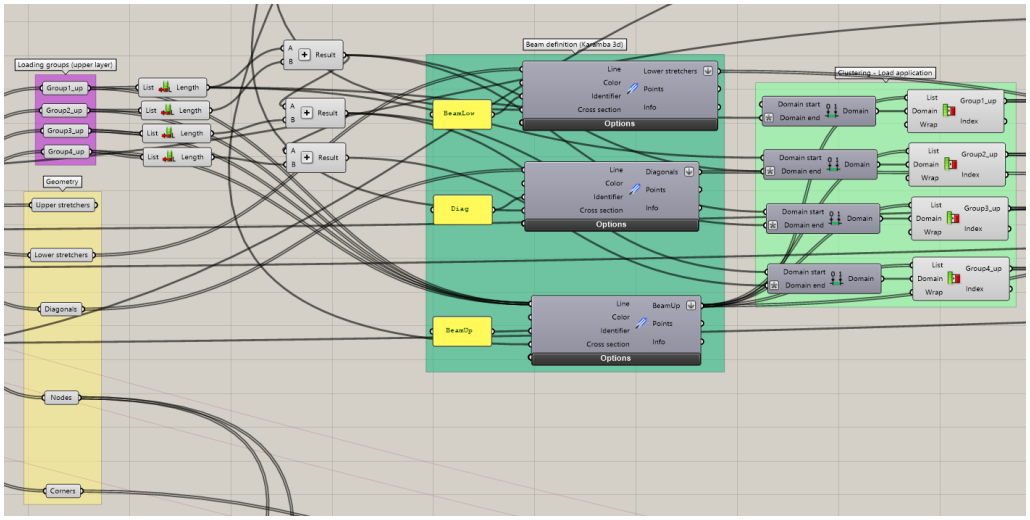

Figure 3.15: Karamba3D beams and beam groups definition

Materials and cross-sections

In Karamba 3D, there are essentially two techniques for defining materials. The first step entails selecting a material from a list of pre-selected options; the second involves manually determining the material's characteristics.
The first approach employs a *Material Selection* component (see Figure 3.16). The values are taken by default from the material table that comes with Karamba 3D if no material list is given. Additionally, this component features a drop-down menu from which materials may be chosen according to their family and name.

As was already indicated, structural steel type S355 was selected.
The Karamba3D list for the cross sections has been used as a guide in this instance. Particularly, certain choices have been taken. After moving the initial list of 221 European circular hollow sections into Excel, a narrow window was chosen. The type of cross-section used is an EN10219-2 CHS standard section, and a total of 177

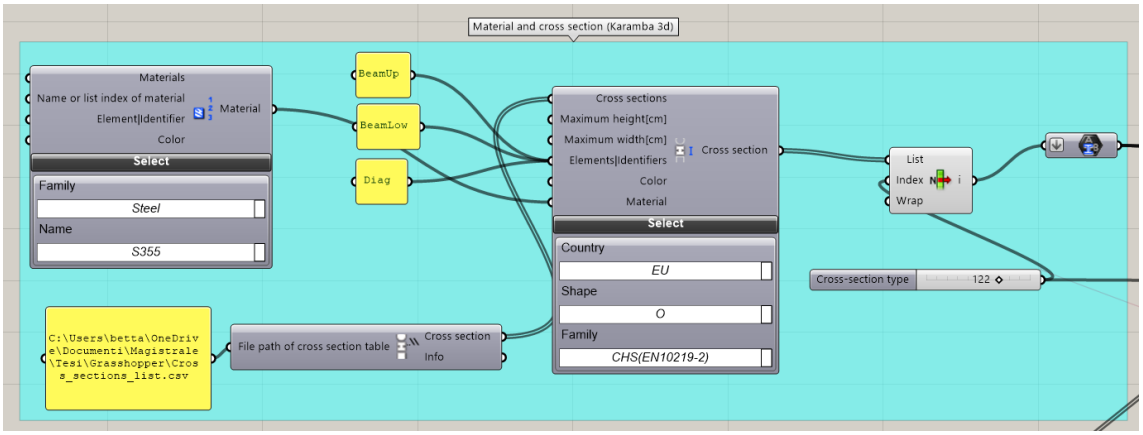

Figure 3.16: Materials and cross-sections

sections, sorted by ascending cross-sectional area, were taken into account.
This sample was obtained with the assumption that the project will only include Sections of Classes 1, 2, and 3 (see Eurocode 3, 1993), avoiding Class 4 cross-sections where local buckling would occur before the cross-section reached yield stress in various locations.
Class 4 tubular sections can be distinguished as shown in the table in Figure 3.17, taken from EN 1993-1-1.

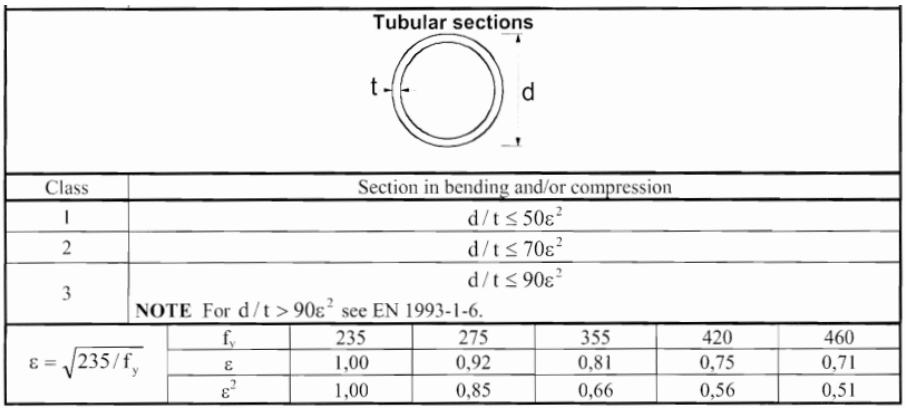

Class	Section in bending and/or compression					
1	$d/t \le 50\varepsilon^2$					
2	$d/t \le 70\varepsilon^2$					
3	$d/t \le 90\varepsilon^2$ **NOTE** For $d/t > 90\varepsilon^2$ see EN 1993-1-6.					
$\varepsilon = \sqrt{235/f_y}$	f_y	235	275	355	420	460
	ε	1,00	0,92	0,81	0,75	0,71
	ε^2	1,00	0,85	0,66	0,56	0,51

Figure 3.17: Tubular sections' maximum width-to-thickness ratios for compression parts (1993)

As a result, the elements of the original list for which the following relationship occurred have been eliminated:

$$\frac{d}{t} \geq 90\epsilon^2 \tag{3.9}$$

where ϵ depends on the type of steel.

All beams in this initial attempt have the same cross-section, which is selected by the optimizer.

Boundary conditions: supports and joints

To fine-tune supports, the Karamba 3D's *Support* component (see Figure 3.18) has been used. In general, the support component offers three translational (T) and three rotational (R) degrees of freedom in global directions by default, or, if that is not feasible, according to a user-defined local plane.

Four fixed supports have been constructed for this project and properly positioned with the lower layer's four corners.

The *Beam-Joints* component was utilized to create a joint. In addition to identifying joints and assigning hinges to the elements, this component also maintains track of geometrical connections. A list of degrees of freedom and vectors containing the translational and rotational spring stiffness can also be assigned, as in Figure 3.18.

By use of this component, releases at the ends of each beam have been specified as truss elements. These elements can only transfer axial forces and bending moment in y direction by means of the hinges made between the beams.

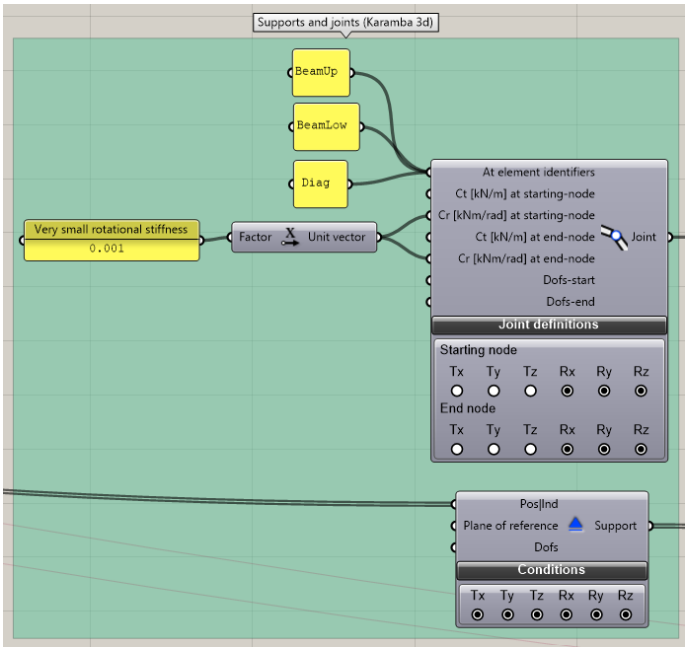

Figure 3.18: Supports and joints

When doing static analysis, the absence of a support condition or joint agent, or an incorrect description of them, leads to a very significant displacement or the inability to assess the structure with a rigid body movement.

Loading application

In accordance with Eurocode, the structure has only been subjected to gravity loadings considering the ULS combination. Regrettably, switching between combinations is not permitted in Karamba3D and it is not automatically computed, therefore only the following one has been manually set:

$$\gamma_{G1} \cdot G_1 + \gamma_{G2} \cdot G_2 + \gamma_P \cdot P + \gamma_{Q1} \cdot Q_1 + \gamma_{Q2} \cdot \psi_{02} \cdot Q_2 + ... \tag{3.10}$$

where G1, G2, and Q_{ki} are respectively the permanent structural loads, permanent non-structural loads, and variable loads. Instead, based on the nature of the loads,γ is set as a coefficient of amplification. The following loads (see Table 3.1), together with their related coefficients of amplification, have been taken into consideration in this case study.

Load type	**Load value**	γ
G_1	Self-weight [kN]	1.3
G_2	1.57 kN/m^2	1.5
Q_1	1.23 kN/m^2	1.5

Table 3.1: Gravitational loads applied to the structure

Karamba3D automatically calculates and applies the self-weight of all the beams (G1); however, in order to apply the corrugated sheet load (G2) and the snow load (Q1), the exact beams to which the loads should be applied must be identified.

Due to the structural typology, an area of influence should be taken into account while applying distributed vertical loads to the upper layer. The method for applying the load is based on the clustering of the beams shown in Figure 3.19. The groupings are as follows when referring to the outputs of the Python code:

- *Group1_ up*, containing the lines of the upper layer highlighted in blue;
- *Group2_ up*, containing the lines of the upper layer highlighted in pink;

- *Group3_up*, containing the lines of the upper layer highlighted in light blue;
- *Group4_up*, containing the lines of the upper layer highlighted in yellow.

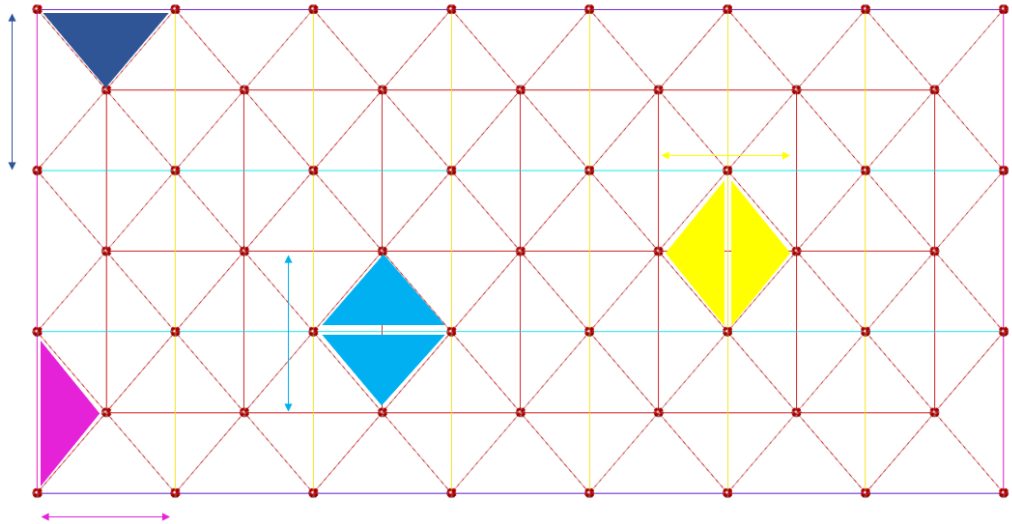

Figure 3.19: Top view with highlighted beams for load application and their respective area of influence

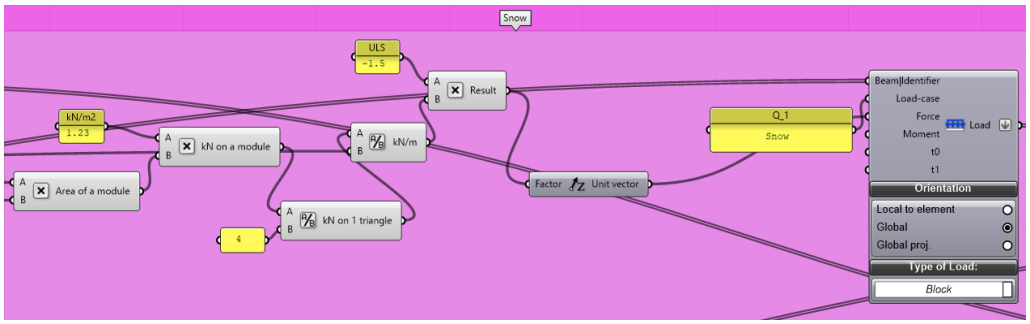

Figure 3.20: Example of snow linear load application for one group

Each beam is loaded according to the area of the triangles shown in Figure 3.19, following the geometric pattern generated by the truss typology.

The load applied to the beams is calculated by multiplying the Load Value by the area of a single module (kN). Then, this load is divided by 2 for the internal components and by 4 for the components that lie on the perimeter. Distributed linear loads in kN/m are subsequently calculated by dividing the result by the span in the opposite direction (see Figure to identify the clustering technique, the areas

of influence, and the interaxis by colors). In particular, the load analysis's values are an indirect function of the design variables div_x and div_y.

As is common in such structural typology, the loads were first imposed as point-loads at the nodes. However, the decision to apply distributed loads on beams was made since, in the prior case, the beams were only bearing their own weight and were not sufficiently loaded for bending. Axial stress values increased as a result.

Model assembly and analysis of structural model

The geometrical inputs, support conditions, and load have been assembled together to create the finite element model. The element name, load status, support condition, cross-section, and material properties are the specific inputs to the component *Assemble model*. This component prepares the model for evaluation. Karamba3D will then use the chosen algorithm to analyze these sets of elements.

The used component, *Analyze*, computes the deflections of a specified model using first-order theory. When the structure is loaded in first-order (linear static) analysis, it is assumed that the stiffness of the structure remains constant and unaffected by changes in the geometry of the structure. It's crucial to make sure that deflections are small given the size and span of the structure.

Verification and results output

The extraction and visualization of structural analysis results were made possible by additional components like *Beam View* and *Model View*. The output of individual beams can be seen in *Beam View*, whereas the shape of the model after deformation can be seen in *Model View*. The findings for axial stresses and utilization ratios can be viewed in both color and numerical from there.

To guarantee that Karamba 3D performs the structural checks and verifications accurately agreeing to Eurocode 3, the inside code of the plug-in has been reviewed. The design strategy takes account of normal force, biaxial bending, torsion, shear force, and combined actions. So, in order to check whether a given beam cross-section is adequate, Karamba3D applies a strategy for steel beams agreeing to EN 1993-1-1. The interaction values for the cross-section forces get calculated concurring to Appendix B of the Code (2013).

The unfavorable effect of compressive normal forces in a beam can be taken under consideration globally or locally on the level of individual members. The strategy applied in this case study works on the member level. A vital precondition for this strategy to provide valuable results is the assurance of a reasonable buckling length of an element. For this, a simplification is applied: beginning from the endpoints of an element, the buckling length is determined as the distance between the neighbor nodes (2013).

The design strategy applied in Karamba3D takes also lateral torsional buckling into consideration.

The check for local buckling uses the classification of cross sections into classes 1 to 4 concurring to EN 1993-1-1. Class 4 cross-sections are vulnerable to neighborhood buckling, due to the cross-section list has been constrained, as stated in Section 3.3.1.

Utilization of Elements is a further component that was frequently employed to ensure that structural verification calculations were accurate. It is required in order to determine the level at which each component is utilized. It allows users to determine whether or not Karamba3D includes checks for buckling. As raised in Figure 3.21, this component necessitates the definition of two partial resistance factors: one for the resistance of cross-sections, γ_{M0}, regardless of class; and the other for the resistance of members to instability based on member checks, γ_{M1}. By default, the values are both set to 1, however it has been decided to move them to 1.05 instead, as indicated in NTC2018 (2018) in Tab. 4.2.VII.

Due to some approximations generated by the internal checks of the Karamba3D plug-in (see Karamba3D manual, 2013) and due to the internal procedure's rounding up of the steel's yielding resistance from 355 MPa to 360 MPa, it was necessary to confirm the accuracy of the results using a more accurate FEM software. The outcomes of Grasshopper were compared using SAP2000 in terms of solicitations and utilization ratio, namely actions and verifications.

The software's plug-in limit in the automatic computation of load combinations is worth mentioning once again. This is required to go into the details of the conservative method used to determine the Demand/Capacity ratio.
The main issue with Karamba3D is that, aside from visualizing the applied load, each load case's numerical results are generated separately. The outputs for each

load scenario should be added together in order to obtain the results for the load combination that was manually defined first.

An inaccurate computation of the sum of the effects is the root of the difficulty with summing the outcomes in terms of D/C ratios. Nevertheless, it has been established that a conservative design may be achieved by summing up these ratios for each load case to get the overall one for each beam, as can be seen from the percentage differences in Table.

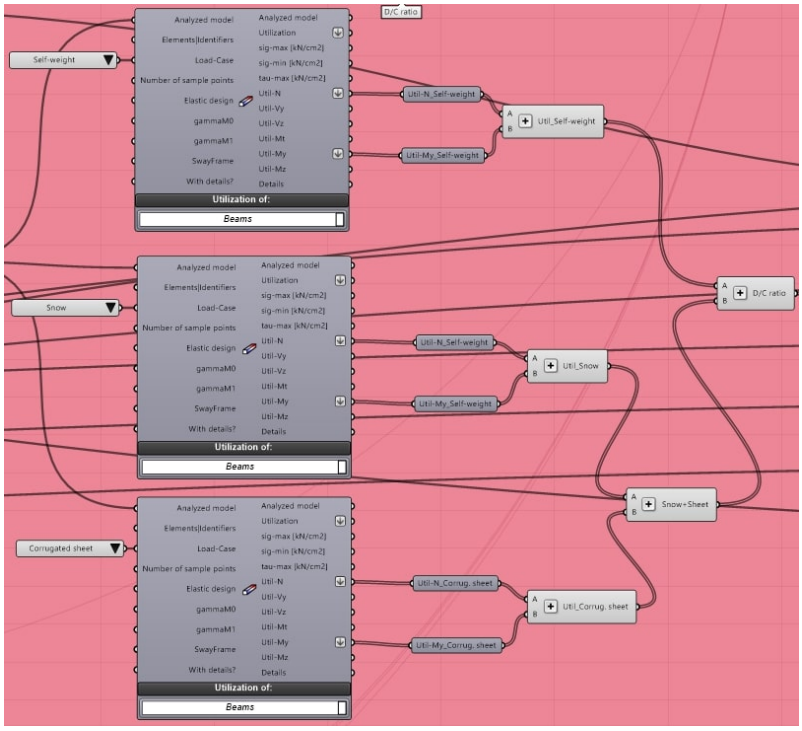

Figure 3.21: Demand/Capacity ratios calculation

It should be noted that the aforementioned component's "Utilization" primary output provides a value that is the highest value discovered for each beam in relation to the worst load case and to the most significant demand between N and M. As can be seen in Figure 3.21, in order to properly take into account the check against buckling, the "Util" values relating to N and M are summed up for each beam before summing the results for each load scenario.

After the latter has been pointed out, a comparison of the outputs of the two FEM solvers can be seen in Figure B.1 and B.2. Particularly in Figure B.2, SAP2000's outcomes only display the utilization factor of each beam using a color scale from light blue to red, which corresponds to a range between 0 and 1. In contrast, the

Model View component in Grasshopper does not take buckling checks into account when displaying utilization factors, so red and blue beams represent compressed and stretched elements, respectively. However, by observing the compression trend of the beams, it is feasible to recognize the similarities to the SAP2000 results.

To be more specific, Table 3.2 reports a sample of numerical results from each of the two solvers along with their percentage difference. The compared beam is highlighted in the aforementioned figures in Appendix B.

CHS	**Karamba3D**		**SAP2000**		**%D**	
	N [kN]	**D/C [-]**	**N [kN]**	**D/C [-]**	**N**	**D/C**
457x10	-3020.17	0.715	-3017.14	0.721	0.10%	0.83%
406.4x8	-2640.29	0.927	-2643.12	0.940	0.11%	1.38%
355.6x10	-2775.08	0.919	-2777.08	0.930	0.07%	1.18%
323.9x12	-2840.44	0.909	-2844.98	0.918	0.16%	0.98%
323.9x10	-2698.80	1.024	-2702.03	1.036	0.12%	1.16%
273x12.5	-2727.11	1.102	-2729.79	1.115	0.10%	1.17%
244.5x12.5	-2641.09	1.203	-2645.44	1.134	0.16%	5.74%

Table 3.2: Numerical results from Karamba3D and SAP2000

It is clear from the presented example that the analysis outcomes lead to layouts with large cross-sections and wide spans. Despite this, the aforementioned checks have proven that the analysis of the model takes effects of local instability into account with this first raw model. Reasonable spans and cross-sections will be taken into account in the real case study.

Additionally, a sensitivity analysis has been done to examine how changes in the parametric roof's height affect the choice of the best cross-section since they result in greater beam bending moment absorption.

3.4 Optimization problem

Once the model is put together, the solver will run structural analyses on each configuration, and from the results, the Objective Function may be implemented. The formulation of the analysis in detail is covered in the part that follows, but for now a flow chart in Figure 3.23 summarizes its essential framework. The individuals

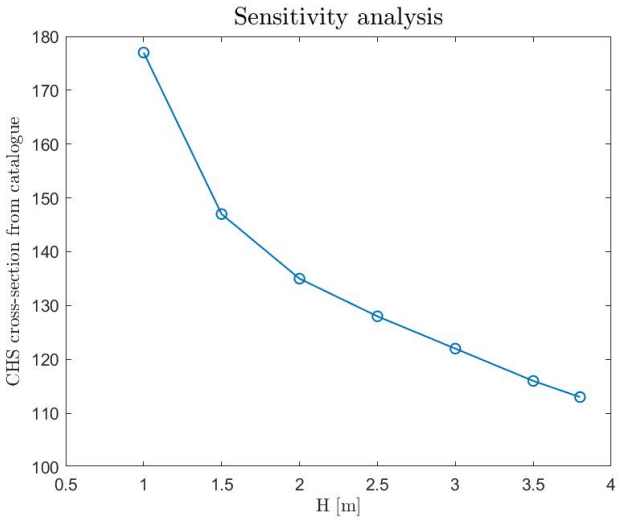

Figure 3.22: Sensitivity analysis

get created throughout each generation by altering the design variables and enforcing structural verifications in accordance with Eurocode 3 until the optimal arrangement is attained.

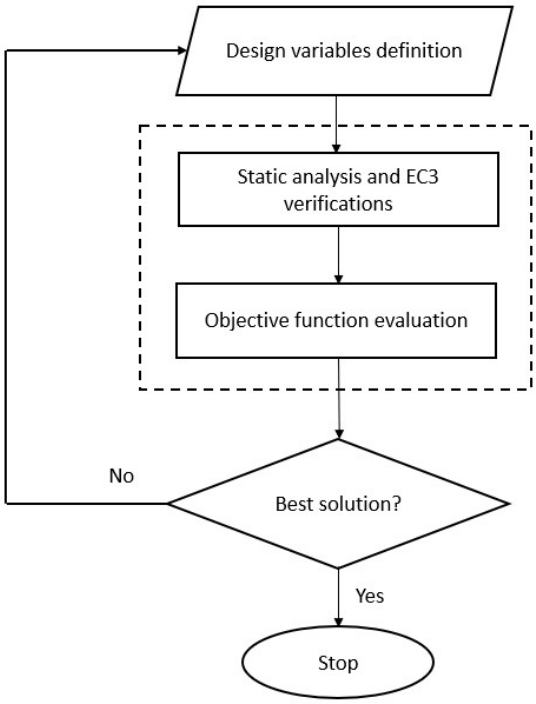

Figure 3.23: Flow chart of the optimization process

As was already mentioned, the goal of the thesis work is to create a space frame structure on which a finite element analysis will be performed. This structure will be initially optimized for mass while varying both the height of the structure and the number of elements in terms of beams and nodes along the development of the spans L_x and L_y. On top of a procedure of this kind (topological optimization), shape and size optimizations were also carried out, allowing for the simultaneous optimization of the cross-sections of the beam elements.

The three optimization types were accomplished by utilizing the *Octopus* Grasshopper plug-in.

Table 3.3 outlines the key parameters and settings used in the optimization algorithm.

Table 3.3: Optimization Algorithm Parameters and Settings

Parameter	Value
Maximum Iterations	200
Population Size	200
Mutation Probability	0.2
Crossover Probability	0.8
Convergence Threshold	0.001
Selection Mechanism	Tournament Selection
Penalty Functions	ϕ_1, ϕ_2
Optimization Approach	Penalty-Based
Algorithm Integration	SPEA-II (Octopus Plug-in)

A single-objective optimization problem, i.e., a problem with just one function to be optimized, constitutes the assignment.

The formulation of the objective function highlights the distinction between beam elements and nodes and it is stated as follows:

$$minf(\mathbf{x}) = \rho \overbrace{\sum_{i=1}^{N} A_i l_i \cdot \phi_1}^{\text{Elements}} + \overbrace{M_{node} \cdot \phi_2}^{\text{Connections}} \quad [ton] \tag{3.11}$$

subjected to

$$\frac{N_{Ed} \cdot \gamma_{M1}}{\chi_y \cdot N_{Rk}} + k_{yy} \cdot \frac{M_{y,Ed} \cdot \gamma_{M1}}{\chi_{LT} \cdot M_{y,Rk}} + \frac{M_{z,Ed} \cdot \gamma_{M1}}{M_{z,Rk}} \leq 1 \tag{3.12}$$

from EC3 6.3.3(4)-6.61 (1993) and to

$$\mathbf{x}_{i,min} \leq \mathbf{x}_i \leq \mathbf{x}_{i,max} \tag{3.13}$$

where

- N is the total number of beam elements in the truss;
- ρ is the density of steel grade S355;
- $\mathbf{x}$ is the vector of design variables;
- M_{node} is the mass of a single node;
- ϕ_1, ϕ_2 are the penalty functions.

For completeness, the whole Equation 3.12 has been reported. When steel beams are subjected to traction, it does not include buckling verifications.

Penalty functions

At the element level, truss structures frequently experience buckling instability. As can be seen in the aforementioned paragraph, there is an item called *Utilization* that provides details regarding the fulfillment of the combined bending and axial compression requirements. In general, one of the key aspects that has to be looked into is how slender the compressed elements are. The slenderness is commonly taken into account for the verification of buckling stability and is defined as:

$$\lambda = \frac{l_0}{\rho} \tag{3.14}$$

where l_0 is the effective length and ρ is the least cross-section radius of gyration.

The verification relating buckling problem recommends employing a reductive coefficient, χ, which accounts for the Euler's critical load (see Eq. 3.12). Particularly, this factor establishes the extent of a bar's compressive stress capacity that may be applied before the bar is expected to buckle and it depends on the non-dimensional slenderness, $\bar{\lambda}$, and on an imperfection factor α.

From a theoretical perspective, the buckling phenomena must take into consideration both the supporting conditions and the slenderness of the components. With

the exception of the four corner fixed supports, all of the elements in the current setting have pinned connections at their ends, however, the lengths vary depending on the configurations.

In this research, the number of elements having an acting stress to buckling strength ratio greater than one has been calculated. This penalty in the evaluation of the OF has been amplified by multiplying the number of unfeasible beams, n_k, by a coefficient K_1. Its formulation is expressed as follows:

$$\phi_1 = 1 + n_k \cdot K_1 \tag{3.15}$$

where $K_1 = 1.1$, so that the number of unfeasible elements is increased by its 10%. If no unfeasible beams are found, $\phi_1 = 1$, thus no penalization is applied.

The OF highlights the model's two primary structural elements individually, as shown in Eq. 3.11. The second penalty omits structural inspections since an in-depth analysis of the connections is not considered part of this task. The number of nodes is simply increased by an amplification factor K_2 of 10% in ϕ_2, as shown below:

$$\phi_2 = N_{nodes} \cdot K_2 \tag{3.16}$$

3.4.1 Clustering approach

This preliminary single-objective optimization has been applied to several configurations in order to assess the most appropriate clustering strategy by varying the number of elements belonging to the same class of component (e.g. same cross-sectional property). However, a huge number of different items should be discouraged aiming to detect a balanced compromise between the design efficiency and the structural complexity expressed in terms of manufacturing, assembly, and practical need in situ. In this way, the minimization of the overall complexity is achieved complying with the structural response and the imposed safety conditions. In addition, achieving the best cross-sectional clustering is necessary to obtain a meaningful decrease in the total mass of the space frame.

As mentioned in Paragraph 3.1, due to its distinctive architectural characteristics, the space truss has been acknowledged as a superior structural form for obtaining also huge spans when compared to the plane truss. Such a structure is characterized

by interconnected members with a standard sectional shape located in the upper and lower chords and diagonal directions, where the global structural stiffness can be significantly increased in comparison to planar structures and the loads are distributed more evenly in three dimensions. Specifically, the generated geometry is allowed to produce modules that are square or rectangular. This allows the system to investigate different loading pathways.
In conclusion, adopting an efficient clustering strategy leads to feasible design solutions in terms of constructability in situ and minimization of the structural and economic final cost.

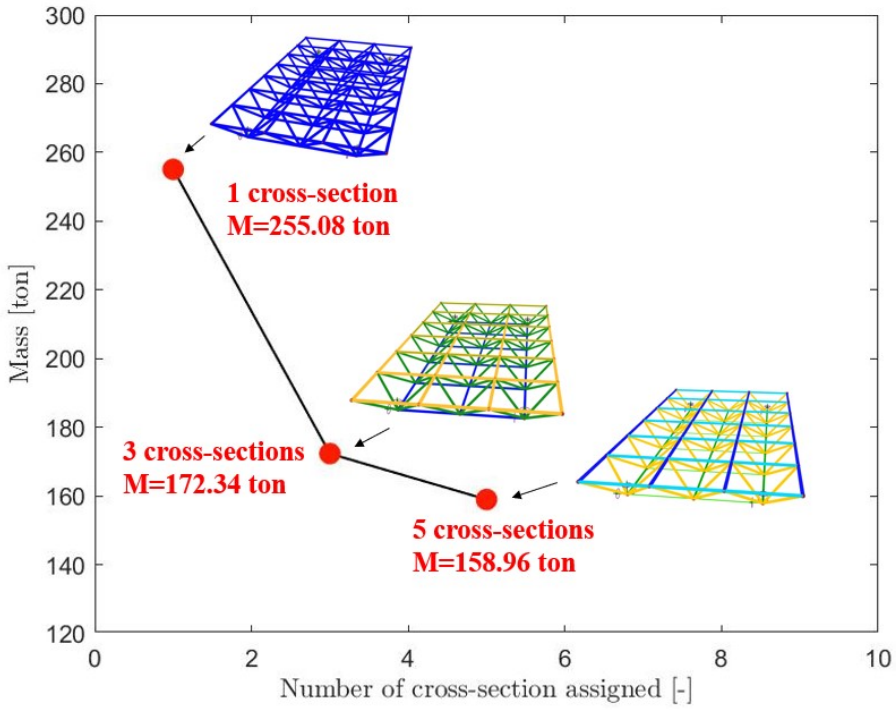

Figure 3.24: Comparison between configurations with respect to mass minimization

As expected, if the entire structure were configured with a single cross-section, all of the beams would need to be able to withstand the maximum stresses encountered by the most distressed elements. Consequently, a significant increase of the least weight is observed. The first investigated setup corresponds precisely to this first scenario, which is used as a benchmark. On the other hand, if the optimizer is free to select a distinct cross-section for each set of elements, the overall structure would have the lowest weight while having the most sophisticated design (see Figure 3.24).

Design variable	**Description**	**Bounds**
$x_1 = H$	Height of the roofing structure	$0.5 \div \frac{L}{15}$
$x_2 = div_x$	Number of divisions in x direction	$6 \div 60$
$x_3 = div_y$	Number of divisions in y direction	$3 \div 30$
x_4	Section for all elements in the model	$0 \div 176$ CHS profiles' index from list
x_4	Section for the upper chord	$0 \div 176$ CHS profiles' index from list
x_5	Section for the lower chord	$0 \div 176$ CHS profiles' index from list
x_6	Section for the diagonals	$0 \div 176$ CHS profiles' index from list
x_4	Section for the upper chord - beams in x direction	$0 \div 176$ CHS profiles' index from list
x_5	Section for the upper chord - beams in y direction	$0 \div 176$ CHS profiles' index from list
x_6	Section for the lower chord - beams in x direction	$0 \div 176$ CHS profiles' index from list
x_7	Section for the lower chord - beams in y direction	$0 \div 176$ CHS profiles' index from list
x_8	Section for the diagonals	$0 \div 176$ CHS profiles' index from list

Table 3.4: Design variables of the three configurations: red - Topology, Shape, Size; green - Cross-sections assignation 1st configuration; yellow - Cross-sections assignation 2nd configuration; cyan - Cross-sections assignation 3rd configuration

The design variables, x_i, involved in the optimization were presented in the earlier Section 3.3 and are compiled in Table 3.4.

Different colors have been used to differentiate the design variables. While the remaining colored portions of the table indicate the additional cross-section assigna-

tion variables for each of the three configurations, the first ones may be categorized as Topology, Shape, or Size variables. Figures 3.25, 3.26 and 3.27 provide a graphic representation of them in their already optimized arrangement.

Configuration A

As already pointed out, the first configuration relates to the scenario when all beams are supposed to have the same cross-section.

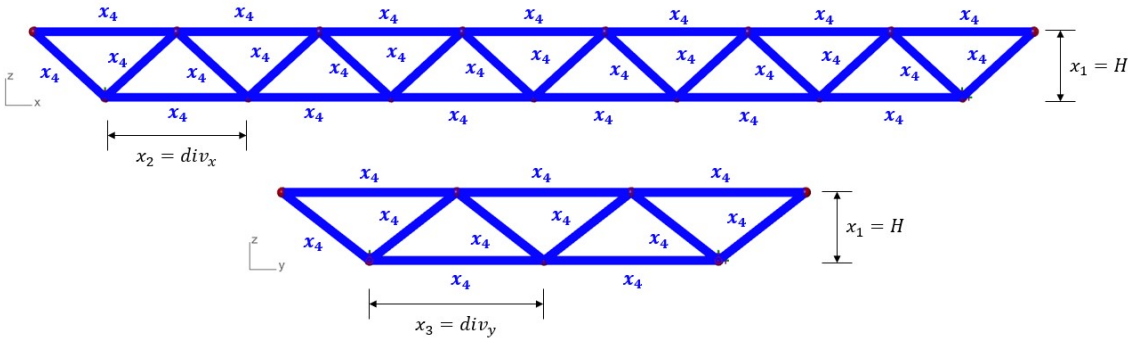

Figure 3.25: Schematic representation of the design variables of Configuration A

Configuration B

The second arrangement emphasizes a more practical method of cutting down on material waste. The optimizer is called to differentiate the cross-section's size depending on the upper chord, lower chord, and diagonal macro-groups of beams.

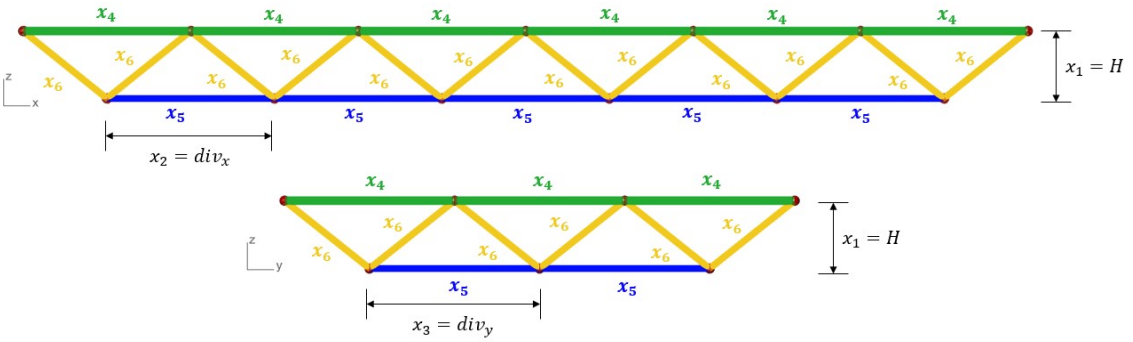

Figure 3.26: Schematic representation of the design variables of Configuration B

Configuration C

The third configuration is an improvement over the second, distinguishing between longitudinal and transversal elements - respectively along x and y axes - within the two layers.

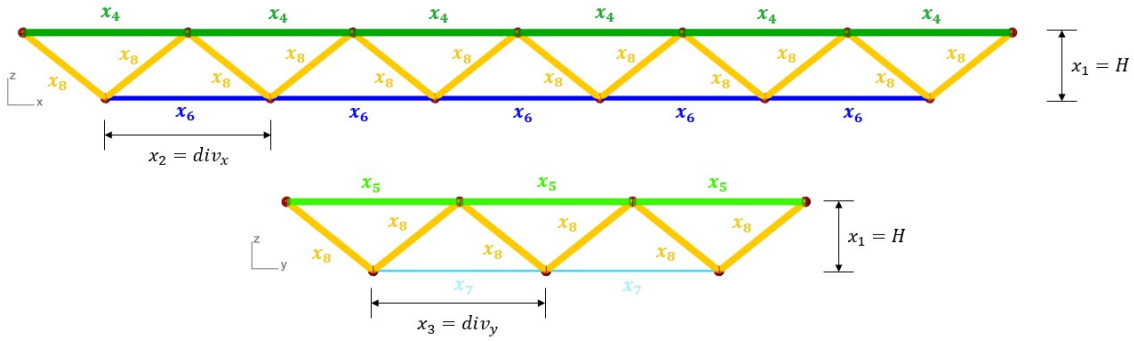

Figure 3.27: Schematic representation of the design variables of Configuration C

3.5 Results and discussion

The outcomes of the structural optimization process are highlighted in this section with particular reference to the three previously mentioned scenarios.
For the sake of comparison, a mass minimization has been carried out. In order to improve the structural response for an upcoming real-case application, an investigation was needed to calibrate the model and identify the optimum clustering approach.

In the Appendix B.2, a perspective view of the optimal structure for the three configurations is presented (front and lateral views are shown in Figures 3.25, 3.26 and 3.27).

A summary of the best design variables is displayed in Table 3.5 along with the best results in Table 3.6.

Table 3.6 allows to see that there are slight numerical discrepancies between OF and Mass. This is because connections are subjected to a fixed penalty. Since the structural penalty of the best solution is equal to 1, no unfeasible individual has been selected.

As expected, though the geometrical features of the structures, e.g. H, div_x, and

Design variable	Unit	Conf. A	Conf. B	Conf. C
$x_1 = H$	m	3.9	4	4
$x_2 = div_x$	-	7	6	6
$x_3 = div_y$	-	3	3	3
x_4	mm	CHS 457x12.5	CHS 508x12	CHS 508x12
x_5	mm	-	CHS 219.1x12	CHS 355.6x10
x_6	mm	-	CHS 323.9x10	CHS 323.9x12
x_7	mm	-	-	CHS 168.3x5
x_8	mm	-	-	CHS 323.9x10

Table 3.5: Design variables of the optimized configurations (see Table 3.4 for references)

	OF [ton]	Mass [ton]
Conf. A	259.78	255.08
Conf. B	176.42	172.33
Conf. C	163.05	158.96

Table 3.6: Results of the optimized configurations

div_y, remain the same among all the configurations, significant mass losses can be attributed entirely to the increase of the different components.

More in detail, the mass of the clustering technique B has decreased by around 32% as compared to Configuration A. Configuration C revealed an extra 8% more in reduction by slightly improving the model.

As depicted in Figure 3.28, for all the investigated configurations, the optimal solution is achieved already at the first iteration for values of subdivisions along x and y direction equal to $div_x = 6$ and $div_y = 3$ resulting in a modular span equal to $\Delta = 10m$. Additionally, the total height of the truss structure reaches early the optimal value equal to $H = 4,0m$ These configurations, where the minimum number of connections have been adopted, are preferred by the optimizer when larger cross-sections have been assigned to each structural component.

Charts showing the best individual identified at each iteration, together with its mass and the its unfeasibility proportion, have then been reported 3.28.

The unfeasibility proportion's purpose is to provide an estimate of the percentage of unfeasible individuals produced in each generation. The internal configuration

of the algorithm within the Octopus plug-in (selection, crossover, and mutation operators) and the structural verifications are key factors for the computation of the proportion.

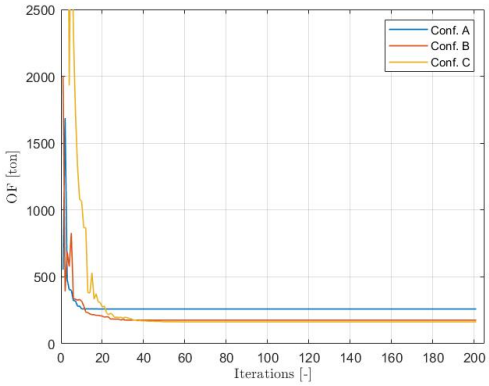

(a) Best individual at each iteration (OF)

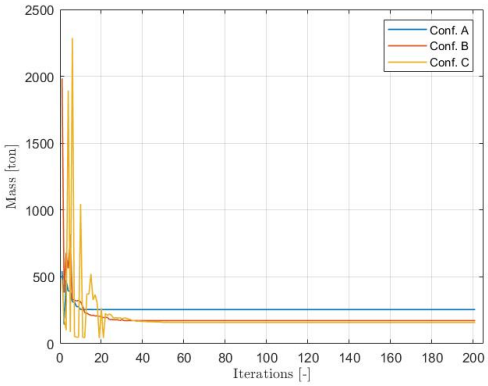

(b) Mass of the best individual at each iteration

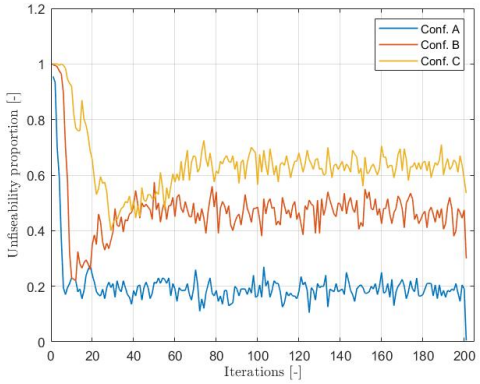

(c) Unfiseability proportion

Figure 3.28: Best results of each configuration

For Configurations A and B, this is readily apparent, however in C, the initial generations show a slightly different tendency. This is as a result of the best individuals in the first generated populations still having some unfeasible components that end up as null. The unfeasibility proportion chart, however, consistently demonstrates how Octopus continually produces a large number of unfeasible individuals at each iteration in order to enhance the analysis, while keeping a significant number of acceptable ones.

The optimal proposed solutions show significant differences from real-world applications: typically, common practice involves a far greater number of rods with

element length no more than 5 m. While it has been shown that the obtained is structurally verified, other options are considered due to road transport problems or difficulties in assembling (welding or bolting) many pieces on site. In spite of this, the lengths that the optimizer generated meet the requirements for either complexity for the on-site assembly and erection phases or transportability (maximum length of the transport rods equal to 12 m).

Given the aforementioned reasons and the notable reduction in mass attained, Configuration C is considered the best clustering strategy for Case Study 2, which will be covered in the upcoming Chapter.

Chapter 4

Methodology - Case study 2: Industrial building

The study that has been shown thus far has only been at the level of the roofing structure, but the goal is to apply this theoretical process to a much larger structure. As a result, the building under investigation in this Chapter will be parametrically modeled and optimized using the prior case study's methodology. The investigation will show how the structural objective function may perform under more difficult and demanding circumstances. The environmental OF is currently introduced to perform a multi-objective optimization that aims to reduce the structure's mass as well as the CO_2 equivalent emissions due to its elements' materials and life-cycle processes (specifically, GWP total according to EN15804+A2 2022).

4.1 Parametric model

The potential of the parametric design was also used in this case to generate the geometry of the structure. The modules of the double-layered space frame structure, which make up the design of the coverage, are still producing a certain number of repetitions with a spacing, Δ, in both x and y directions. This spacing will act as an indirect variable in the issue. In particular, the goal is to optimize the depth between two grids, the number of elements, and the appropriate cross-sections.

The structure's overall size is fixed at 60 meters in x direction and 30 meters in

y direction, as before, allowing for tighter or wider modules. The roofing system, in particular, is identical to that of the prior case study, with components identified as upper chord, lower chord, and diagonals. In addition, columns are introduced with a height set to 8 meters.

The main dimensions are provided in Figures 4.1 and 4.2, where the same color legend of the previous case has been maintained.

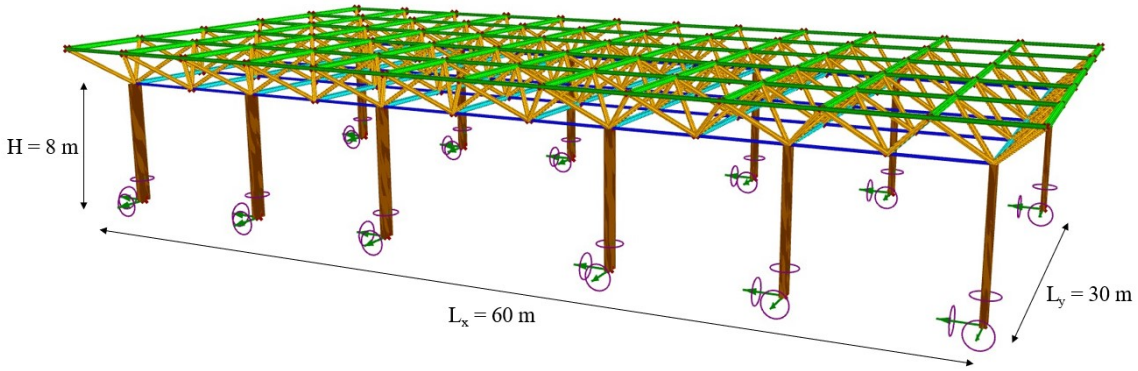

Figure 4.1: Industrial building parametric scheme

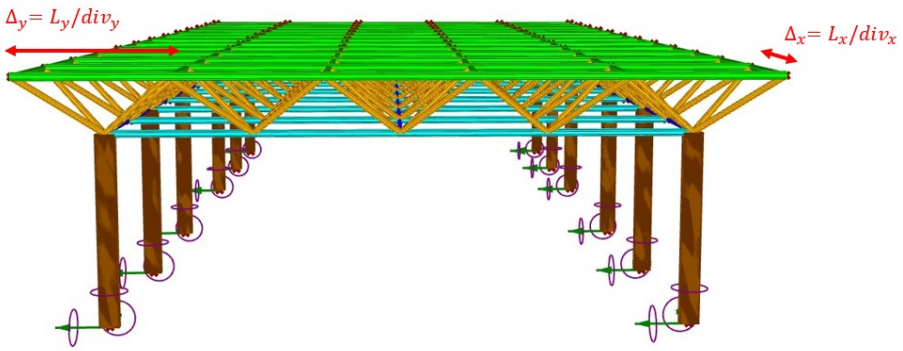

Figure 4.2: Industrial building parametric scheme - Front view

Columns have been connected to the lower chord. The initial and last elements are attached to the furthest corners of the bottom grid while looking at the side along the x-axis, where a row of six columns has been constructed. In relation to an xz plane located at $\frac{L_y}{2}$, the row has been mirrored on the other side.

These elements' spacing has been parametrically determined. Due to the geometric configuration of the space truss, it is not easy to use an identifiable symmetry to reflect the components along the considered axis. Specific intervals have been

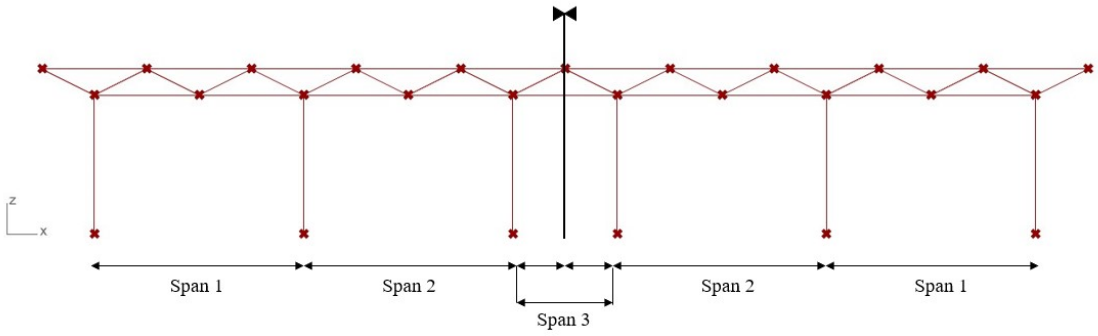

Figure 4.3: Columns positioning approach

defined to determine where to place the vertical elements since variations in the number of divisions during optimization make it difficult to position the columns at a location with given coordinates.

The suggested approach is shown in Table 4.1 below, where two intervals are designated for each span length between the columns. The first interval applies when the lower chord's number of subdivisions in the x direction ($div_x - 1$) is an even number, whereas the second case applies when the number is an odd one. After that, the outcomes are mirrored, as seen in Figure 4.3.

Span	**Intervals [m]**
Span 1	$10 \div 13$
	$6.5 \div 12$
Span 2	$10 \div 13$
	$6.5 \div 12$
(Span 3)/2	$5 \div 7.5$
	$4 \div 6$

Table 4.1: Intervals calculation to place vertical elements

Then, fixed supports are positioned at the base of the building's 12 total columns.

4.1.1 Materials and cross-sections

The next step is to use Karamba3D to convert the model into actual beam elements, as done for the roof. The coverage system's cross-section assignment and clustering have been carried out just as previously. For the cross-sections assigned to the

roof, a typological differentiation has been made, giving the optimizer the option of selecting either open or closed sections. Instead, reliable cross-section profiles have been designated to the column components. In summary, the selections are as follows:

- **Upper chord**: CHS or IPE section (Longitudinal beams - Dark green; Transversal beams - Light green in Fig. 4.1)
- **Lower chord**: CHS or IPE section (Longitudinal beams - Blue; Transversal beams - Light blue);
- **Diagonals**: CHS or double L-section, modeled in Karamba3D as T-section, or rectangular glulam section (reported graphically in dark yellow);
- **Columns**: solid rectangular section (represented in brown).

The cross-sections assigned to the diagonals will be used to assess two scenarios. In the first scenario, all roofing beams will be treated as steel sections; in the second one, the optimizer is allowed to assign glulam sections to diagonal elements as well. In Chapter 4.3, such instances will be further examined.

The items that belonged in class 4 were removed from the given catalogs of Karamba3D steel cross-sections, as indicated in Section 3.3.1. Next, a narrow interval of sections has been selected for each element to aid the optimizer and ensure that there are always balanced percentages of feasible and unfeasible items. Similar to the scenario prior to that, a sensitivity analysis has been done to achieve this goal.

Again, structural steel grade S355 is designated for the first components, while the columns are made of glued laminated timber (glulam) class GL28h.

Glued laminated timber

The glued laminated timber is a kind of structural engineered wood product made of layers that have been joined using durable, structural adhesives such that all of the grain runs parallel to the longitudinal axis.

It is fascinating to compare steel with glulam since they may both be employed in the same kind of load-bearing systems. Compared to glulam, steel is both more

homogeneous and stronger and this allows for the creation of thinner structures. Steel, however, has a far greater production-related environmental effect than timber. For instance, steel has a production phase carbon dioxide footprint that is approximately twice as high (from the data taken from Ökobaudat).

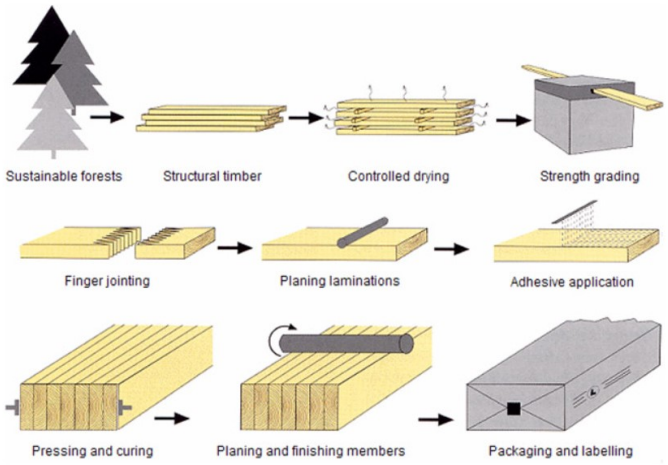

Figure 4.4: Glulam manufacturing stages

The size of a tree is not a constraint on the dimensions of glulam members since a number of smaller pieces of timber are laminated together to form a single huge structural component. Figure 4.4 shows the major stages of glulam manufacturing. Additionally, glulam may be produced in a wide range of shapes, and because of its adaptability, it can be utilized for both beams and columns. Because of the laminating method, which enables the use of timber for considerably longer spans, greater loads, and more complicated forms, it has a significantly lower embodied energy than reinforced concrete and steel (Gross 2013).

The glulam elements are identified by the acronym "**GL xx y**" where *GL* stands for glued laminated, *xx* corresponds to the characteristic flexural strength in N/mm^2 and *y* identifies the type of laminated.
In accordance with the harmonized product standard EN 14080 (2013), laminated wood can be made up of:

- layers with the same resistance: homogeneous laminated timber "**GL xx h**";
- layers with different resistance classes: combined laminated timber "**GL xx c**".

4.1.2 Analysis of loads

The loads placed on the structure are assessed and accurately stated in this section. Because Karamba 3D can only take into account a single combination of loads, as was stated in section 3.3.1, the Ultimate Limit State (ULS) analysis has also been taken into account in this situation. Here, both gravitational and horizontal loads were taken into account. Because of this, the following combination has been used:

$$\gamma_{G1} \cdot G_1 + \gamma_{G2} \cdot G_2 + \gamma_P \cdot P + \gamma_{Q1} \cdot Q_1 + \gamma_{Q2} \cdot \psi_{02} \cdot Q_2 + +\gamma_{Q3} \cdot \psi_{03} \cdot Q_3 ... \quad (4.1)$$

Gravitational loads

The following ones have been considered:

- **Permanent Structural, or Dead, Load** (G_1)
  The self-weight of each component of the structure is known as the Dead Load. It is automatically calculated in Karamba3D, thus just the coefficient of the load combination is required.

- **Permanent Non-Structural Load** (G_2)
  It refers to the corrugated sheet that is used to cover the building's roof. The length of influence must be multiplied by 0.05 kN/m^2, which is the standard load taken into account for the corrugated sheet.

- **Maintenance Load** (q_k)
  The Eurocode offers specific indications to determine the value of qk. The building's roof, where the loads are applied, specifically falls under category H, which is reserved for coverages that are only accessible for maintenance. The same recommendation can be found in the reference National Code, "Norme tecniche per le costruzioni" (NTC2018 2018), because it is presumed that the building is located in Turin (Italy). The selected value in Figure 3.19 is $q_k = 0.5\ KN/m^2$.

- **Snow Load** (q_s)
  According to the Eurocode and to the National code, the general formula for the snow pressure is:
  $$q_s = q_{sk} \cdot \mu_i \cdot C_E \cdot C_T \quad (4.2)$$

Cat.	Ambienti	q_k [kN/m^2]	Q_k [kN]	H_k [kN/m]
A	**Ambienti ad uso residenziale**. Sono compresi in questa categoria i locali di abitazione e relativi servizi, gli alberghi. (ad esclusione delle aree suscettibili di affollamento)	2,00	2,00	1,00
B	**Uffici**.			
	Cat. B1 Uffici non aperti al pubblico	2,00	2,00	1,00
	Cat. B2 Uffici aperti al pubblico	3,00	2,00	1,00
C	**Ambienti suscettibili di affollamento**			
	Cat. C1 Ospedali, ristoranti, caffè, banche, scuole	3,00	2,00	1,00
	Cat. C2 Balconi, ballatoi e scale comuni, sale convegni, cinema, teatri, chiese, tribune con posti fissi	4,00	4,00	2,00
	Cat. C3 Ambienti privi di ostacoli per il libero movimento delle persone, quali musei, sale per esposizioni, stazioni ferroviarie, sale da ballo, palestre, tribune libere, edifici per eventi pubblici, sale da concerto, palazzetti per lo sport e relative tribune	5,00	5,00	3,00
D	**Ambienti ad uso commerciale**.			
	Cat. D1 Negozi	4,00	4,00	2,00
	Cat. D2 Centri commerciali, mercati, grandi magazzini, librerie…	5,00	5,00	2,00
E	**Biblioteche, archivi, magazzini e ambienti ad uso industriale**.			
	Cat. E1 Biblioteche, archivi, magazzini, depositi, laboratori manifatturieri	≥ 6,00	6,00	1,00*
	Cat. E2 Ambienti ad uso industriale, da valutarsi caso per caso	—	—	—
F-G	**Rimesse e parcheggi**.			
	Cat. F Rimesse e parcheggi per il transito di automezzi di peso a pieno carico fino a 30 kN	2,50	2 x 10,00	1,00**
	Cat. G Rimesse e parcheggi per transito di automezzi di peso a pieno carico superiore a 30 kN: da valutarsi caso per caso	—	—	—
H	**Coperture e sottotetti**			
	Cat. H1 Coperture e sottotetti accessibili per sola manutenzione	0,50	1,20	1,00
	Cat. H2 Coperture praticabili	secondo categoria di appartenenza		
	Cat. H3 Coperture speciali (impianti, eliporti, altri) da valutarsi caso per caso	—	—	—
*	non comprende le azioni orizzontali eventualmente esercitate dai materiali immagazzinati			
**	per i soli parapetti o partizioni nelle zone pedonali. Le azioni sulle barriere esercitate dagli automezzi dovranno essere valutate caso per caso			

Figure 4.5: Values for live loads for various categories of buildings - Table 3.1.II NTC2018

where:

- q_{sk} is the reference value of the snow load on the ground which depends on local climate conditions and exposure of the site and on its elevation. Zone 1 corresponds to the building's assumed construction location of Turin. With Turin located at an elevation of $a_s = 239$ m above sea level, q_{sk} can be calculated as $q_{sk} = 1.39[1 + (\frac{a_s}{728})^2] = 1.54kN/m^2$.
- μ_i is a roof shape coefficient and it depends on its inclination. Since the roofing structure is plane ($\alpha = 0$), $\mu_i = 0.8$
- C_E is the exposure coefficient and it is related to the topography of the zone. Because there isn't much snow removal on the structure caused by

the wind in this instance, a coefficient equal to 1 is applied.

– C_T is the thermal coefficient and it takes into account the reduction in snow load, due to its melting, caused by heat loss from the building. It is typically assumed equal to 1.

The final value of the snow load is $q_s = 1.23kN/m^2$.

The assessment of the area of influence is identical to that described in Section 3.3.1.

Horizontal loads

- **Wind Load** The external surface of the structure with greater span experiences lateral pressure due to wind load. As for the other loads, Eurocode advises consulting the National code to ascertain wind pressure, as it is influenced by the building site once again. According to NTC2018 (Chapter 3.3), the wind pressure is evaluated as follows:

$$p = q_b \cdot c_e \cdot c_p \cdot c_d \tag{4.3}$$

where:

– $q_b = \frac{1}{2}\rho v_r^2$ is the reference kinetic pressure where ρ is the air density equal to 1.25 kg/m^3 and $v_b = v_{b,0} \cdot c_a$ is the wind speed dependant on the site of the structure. Looking at Table 3.3.I of NTC2018, the parameters can be determined by referring to Zone 1. The final outcome for q_b is 0.391 kN/m^2.

– c_e is the exposure coefficient and it depends on the topography of the ground, on the location, and on the height of the building. It is computed as follows:

$$\begin{gathered} c_e(z) = k_r^2 \cdot c_t \cdot ln(\frac{z}{z_0}) \cdot [7 + c_t \cdot ln(\frac{z}{z_0})] \quad for \quad z \geq z_{min} \\ c_e(z) = c_e(z_{min}) \quad for \quad z < z_{min} \end{gathered} \tag{4.4}$$

Specifically, $c_t = 1$ is the topography coefficient, while k_r is the class of roughness defined in Table 3.3.III of NTC2018 reported in Figure 4.7. A

Tab. 3.3.I -*Valori dei parametri* $v_{b,0}$, a_0, k_s

Zona	Descrizione	$v_{b,0}$ [m/s]	a_0 [m]	k_s
1	Valle d'Aosta, Piemonte, Lombardia, Trentino Alto Adige, Veneto, Friuli Venezia Giulia (con l'eccezione della provincia di Trieste)	25	1000	0,40
2	Emilia Romagna	25	750	0,45
3	Toscana, Marche, Umbria, Lazio, Abruzzo, Molise, Puglia, Campania, Basilicata, Calabria (esclusa la provincia di Reggio Calabria)	27	500	0,37
4	Sicilia e provincia di Reggio Calabria	28	500	0,36
5	Sardegna (zona a oriente della retta congiungente Capo Teulada con l'Isola di Maddalena)	28	750	0,40
6	Sardegna (zona a occidente della retta congiungente Capo Teulada con l'Isola di Maddalena)	28	500	0,36
7	Liguria	28	1000	0,54
8	Provincia di Trieste	30	1500	0,50
9	Isole (con l'eccezione di Sicilia e Sardegna) e mare aperto	31	500	0,32

Figure 4.6: Table 3.3.I of NTC2018 for $v_{b,0}$, a_0 and k_a

Tab. 3.3.III - *Classi di rugosità del terreno*

Classe di rugosità del terreno	Descrizione
A	Aree urbane in cui almeno il 15% della superficie sia coperto da edifici la cui altezza media superi i 15 m
B	Aree urbane (non di classe A), suburbane, industriali e boschive
C	Aree con ostacoli diffusi (alberi, case, muri, recinzioni,....); aree con rugosità non riconducibile alle classi A, B, D
D	a) Mare e relativa fascia costiera (entro 2 km dalla costa); b) Lago (con larghezza massima pari ad almeno 1 km) e relativa fascia costiera (entro 1 km dalla costa) c) Aree prive di ostacoli o con al più rari ostacoli isolati (aperta campagna, aeroporti, aree agricole, pascoli, zone paludose o sabbiose, superfici innevate o ghiacciate, ...)

Figure 4.7: Table 3.3.III of NTC2018 for k_r

Class B is chosen because the building is meant to be used for industrial purposes. Then, the exposure category must be selected referring to the table reported in Figure 4.8. Lastly, Table 3.3.II of the National code can be entered based on the selected parameters to obtain the corresponding remaining factors of Eq. 4.4. In conclusion, for $z < 8m$ the final value of c_e is 1.55, while for $for \quad z \geq 8m$ c_e is computed parametrically in Grasshopper according to the variations of the depth of the truss during the optimization process.

– c_p is the pressure coefficient which depends on the typology and geometry of the building and on its orientation with respect to wind action. According

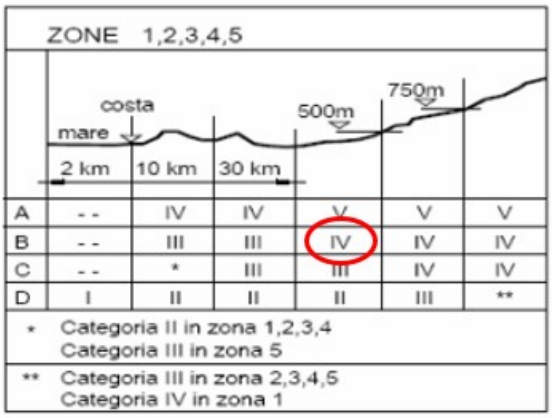

Figure 4.8: Fig. 3.3.2 of NTC2018 to determine the exposure category

Tab. 3.3.II - *Parametri per la definizione del coefficiente di esposizione*

Categoria di esposizione del sito	K_r	z_0 [m]	z_{min} [m]
I	0,17	0,01	2
II	0,19	0,05	4
III	0,20	0,10	5
IV	0,22	0,30	8
V	0,23	0,70	12

Figure 4.9: Table 3.3.II of NTC2018 to determine k_r, z_0 and z_{min}

to the National code, the values of c_p shown in Figure 4.10 can be used for walls.

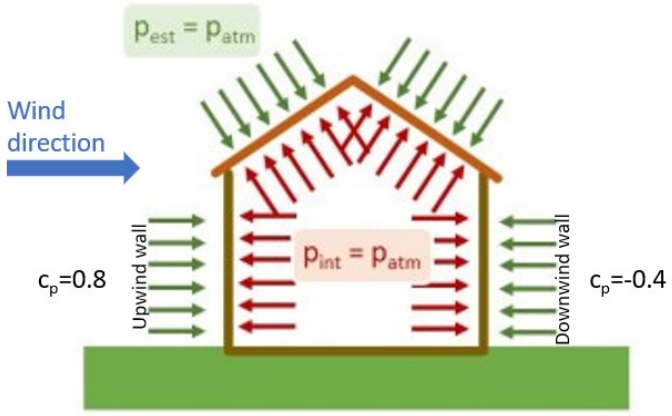

Figure 4.10: Pressure coefficient on walls

Regarding the plane roof, the upwind/downwind bands should be geometrically individuated as in Figure 4.11. To the individuated upwind strip a coefficient

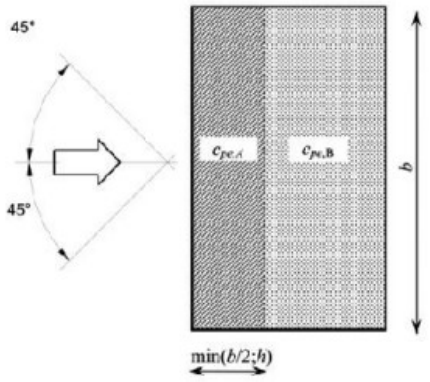

Figure 4.11: Wind application on plane coverage - Fig. C3.5.5 of NTC2018

$c_p = -0.8$ must be applied, while to the remaining downwind zone c_p can assume both negative and positive values equal to ± 0.2. Due to the impossibility of running different combinations on Karamba3D, in a first attempt only the negative value was taken into account. In a second instance, due to internal conflicts in Karamba3D when managing configurations with thousands of elements, it has been chosen to conservatively apply a unique pressure coefficient to the roof equal to -0.8.
The following table provides the final values of wind pressure acting on the longest side of the building obtained through Eq. 4.3:

	c_p [-]	p $[kN/m^2]$
Upwind wall	0.8	0.48
Downwind wall	-0.4	-0.24
Upwind/Downwind roof	-0.8	Depends on c_e

Table 4.2: Wind pressure values

It should be underlined that just the wind-induced external pressure has been considered. This choice is justified by the assumption that the building is airtight and has no openings. However, in order to account for internal pressure and take into account any openings, it would also be essential to take into account the coefficients c_{pi}, which depend on the area covered by the openings.

Additionally, it should be emphasized once more that the inability to create automatic load combinations on Karamba3D forces the selection of a single configuration,

which is equivalent to the setup with the previously mentioned coefficient choice and the wind blowing perpendicularly to the longest side in only one direction.

As was previously said for the vertical actions, an appropriate area of influence needs to be precisely determined when applying the wind load. Both transversal and longitudinal elements experience wind pressure on the roof, and the extent of each element's influence area depends on their relative distance. More specifically, the design variables div_x and div_y indirectly determine the length of influence considered in the study for both internal and external beams, as shown in Figure 4.12.

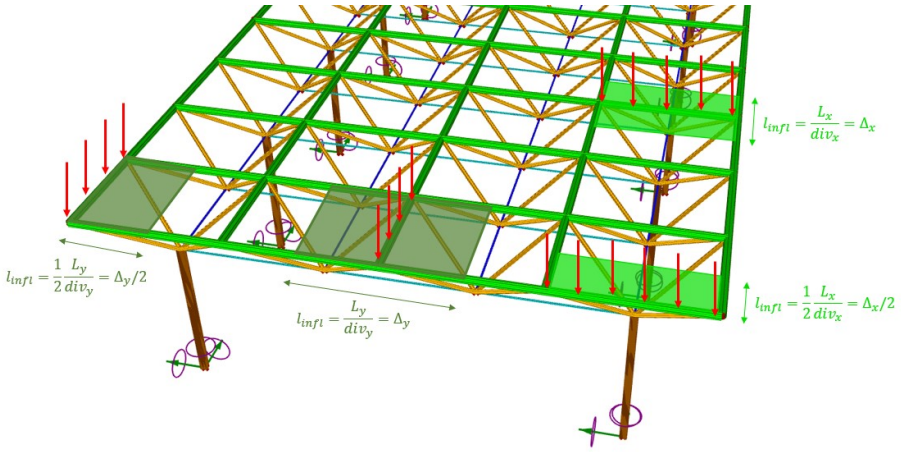

Figure 4.12: Length of influence for internal and external beams of the roof

Additionally, as seen in Figure 4.13, wind pressure is also applied to columns in the x direction and the length of influence is computed based on the mutual distance between vertical elements.

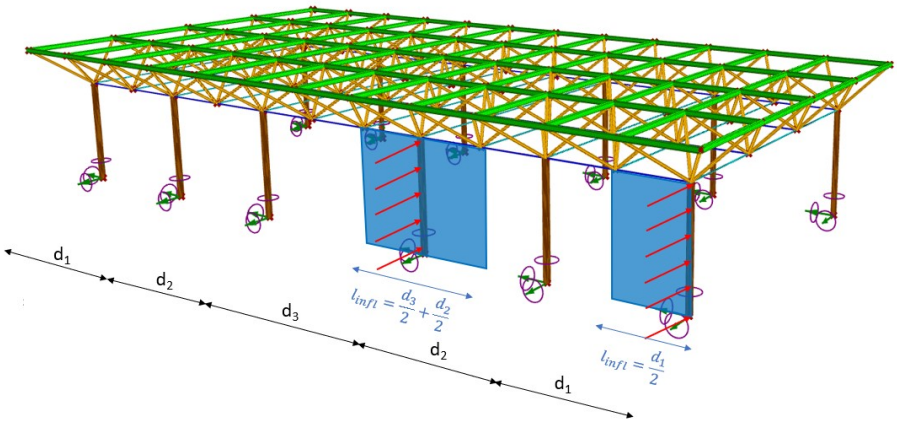

Figure 4.13: Length of influence for internal and external columns

Combination of loads

The final stage is to allocate the coefficients of the load combination to each of the loads once they have all been thoroughly examined. It has been taken into consideration the heaviest load combination due to the previously mentioned limits of Karamba3D. To be able to optimize the bending moment, the Maintenance Load has been chosen as the main variable load. Consequently, the wind action and the snow load have been considered as secondary variable loads with the appropriate ψ_{0j} coefficient. Considering Eq. 4.1 and tables 2.5.I and 2.6.I of NTC18, the following partial and combination coefficients have been imposed:

Load	**Value [kN/m^2]**	γ	ψ
Perm. Struct. Load, G_1	Computed by Karamba3D	1.3	-
Perm. Non-Struct. Load, G_2	0.05	1.5	-
Maintenance Load, q_k	0.5	1.5	-
Snow Load, q_s	1.23	1.5	0.5
Wind Load, p	Depends on c_p and c_e	1.5	0.6

Table 4.3: Loads on the structure and combination coefficients

4.1.3 Boundary conditions: supports and joints

The entire building is supported by the base points of the columns, which are fixed to the ground to prevent translation and rotation. Pinned connections have been specified with respect to the joints between components. A pinned connection is not moment-resistant, but it can withstand stresses that are both vertical and horizontal. They do not permit translation in any direction, only rotation of the structural part.

4.2 Life Cycle Analysis integration

As already pointed out, the case study for this work includes an integrated (structural and environmental) design that could potentially control the structure's emissions during the early phases of design. The goal of the analysis is to reduce the Global Warming Potential total (GWP_{tot} - hereafter referred to as GWP - where $GWP_{tot} = GWP_{fossil} + GWP_{biogenic}$. GWP_{luluc} is neglected) impacts associated

with the construction and dismantling of an industrial steel-timber space frame structure. Due to a lack of information on the building's performance, the usage stage is disregarded.

To establish the system boundaries, there are four common options:

- **From Cradle to Grave** (A–B–C+D): comprehensive examination covering raw material procurement, energy production chain, transportation, usage, and end of life (recycling or disposal);
- **From Cradle to Gate** (A1-A5): stages of use, disposal, and recycling are not considered;
- **From Gate to Grave** (B-C+D): from product usage through its end of life;
- **From Gate to Gate** (A4-A5): the production phase is the only one that is regarded.

The investigation of renovation measures is out-of-scope of this work. Therefore, a "cradle-to-grave" strategy is taken with the exception of the usage stage. The system boundaries can be described as follows:

- **A1-A3**: provision of construction materials and raw materials, transportation, fabrication, and production of integrated building materials;
- **A5**: includes all impacts and aspects related to any losses during the construction process stage of installation and assembly;
- **C+D**: End of Life. The possibility of reuse as a primary material is simulated for the end of life of steel systems; while energy recovery is foreseen for timber.

Taking into account stage A4 for this analysis is irrelevant since the distance between the fabrication facility and the building's construction site is assumed to be fixed.

Data has been gathered for each component of the structure, which is made up of glulam columns, steel connections, and steel/glulam beams.

With a lifetime of 50 years (design working life category 4 of EN1990 - Eurocode, 2002) without the occurrence of earthquakes and structural performances determined by the design strategy, the net floor area (NFA) [m^2] has been selected as

the *functional unit*. Since this is not the instance of a comparative analysis, the functional unit selection is shallow. Nevertheless, the final indicators produced from the optimization process should be divided by the functional unit in order to obtain values that may be utilized for benchmarking and future comparative analyses.

Any process that results in a building product is referred to as "materials." The only indicator taken into account for this analysis is the Global Warming Potential (GWP), which is computed in the following simple form::

$$GWP_{total} = GWP_{A1-A3} + GWP_{A5} + GWP_{C+D} \quad [kgCO_2 - eq.] \tag{4.5}$$

where:

- GWP_{total} is the GWP over the whole life cycle;
- GWP_{A1-A3} is the GWP due to the production stage;
- GWP_{A5} is the GWP due to installation/assembly stages;
- GWP_{C+D} is the GWP due to the End of Life.

The LCA analysis in this study is not carried out using any particular external program. The goal is to perform a LCI based on information and quantities retrieved from Grasshopper and to match the latter with public environmental impact data as described right after.

Production: A1-A3

To compute the environmental impacts associated with constructing the truss structure, LCA datasets is gathered for manufacturing processes and components. LCA datasets can be obtained from product and producer-specific EPDs (Structural steel sections, 2018), if available. Otherwise, generic LCA datasets are selected from the Ökobaudat (2019). Generic datasets include average information and have a wider validity. For instance, they can be applied in situations when only the material is specified without product and producer specifications (Glulam, Stainless steel screws, End of Life of Steel sections and screws). The sphera LCA (fka GaBi) database (2011) was used to model processes related to off-site prefabrication and on-site construction works (open steel section, cutting, and welding operations).

For each component or material, the derived quantities are multiplied by the GWP provided by the matched dataset. If the quantities derived in Grasshopper are expressed in a unit different from the reference unit provided by the environmental datasets, a unit conversion is performed. Environmental datasets provide, moreover, data aggregated by lifecycle module according to EN15798. Therefore obtained results can be also consistently aggregated by lifecycle phase.

Since building-related data will change throughout the optimization process (see Figures C.1, C.2 for LCA Excel-reader tool integrated into Grasshopper), only LCA data are included in the Table 4.4 for the production stage. A presentation of the corresponding results is scheduled for Chapter 5.

Materials (A1-A3)	GWP_{A1-A3} $[kgCO_2 - eq./ton]$
Closed steel profile	1125
Open steel profile	3151.13
Stainless steel screw	4103
Glulam element	-1294.468

Table 4.4: LCA data for production stages

Installation/Assembly: A5

The GWP associated with the installation phase is applied only to steel profiles. In particular, Table 4.5 shows the different items considered in the final value of GWP_{A5}. The GWP connected to these processes is expressed with a unit of 1 meter. The perimeter of the cut or welded section is meant to be computed since this operation is carried out at the cross-sectional level.

Process A5	GWP_{A5} $[kgCO_2 - eq./m]$
Steel laser cutting	1.02E-04
Steel laser welding	0.169
Welding seam 1m	0.648
SUM	0.817

Table 4.5: LCA data for installation/assembly

End of Life and credits: C+D

The composition of the structure, which is based on the quantity of steel and timber material installed, affects the GWP related to the end-of-life (C) and credits (D). As previously said, steel is intended to be treated to be retrained as primary steel for a second cycle (which is not taken into consideration in this case); instead, glulam is given an ending process of incineration with subsequent thermal energy recovery. LCA data is reported in Table 4.6.

Materials (C+D)	GWP_C $[kgCO_2 - eq./ton]$	GWP_D $[kgCO_2 - eq./ton]$
Closed steel profile	0.6821	-393
Open steel profile	0.6821	-393
Stainless steel screw	2.785	-1326
Glulam element	1606.002	-872.127

Table 4.6: LCA data for End of Life and credits

4.3 Optimization problem

The optimization for the industrial building application is based on the roofing truss formulation. Additionally, in order to carry out a multi-objective optimization that fully utilizes the capabilities of the Octopus optimizer, the environmental objective function formulation is provided.

Two scenarios, as previously stated, will be examined. Initially, only vertical elements made of glulam material are introduced. Afterward, a truly mixed steel-timber structure is added as an optimally feasible solution to investigate the possibilities of adding timber elements. This is accomplished by allowing the optimizer to select between glulam and steel cross-sections for diagonal components.

The first step should be to define the relevant design variables. Effectively, except for the new variable for columns glulam cross-sections, the number of variables remains identical to that of Configuration 3 of Chapter 3.4 for the roofing structure. Furthermore, in order to provide the optimizer with a feasible research space consistent with the practical design solutions, a suitable list of different classes of cross-sections (open and closed) and their geometric properties as well as the maxi-

mum and minimum boundaries of the total height have been adopted.

Table 4.7 highlights the differences between the two scenarios that were taken into consideration, namely in terms of the interval of cross-sections that were allocated to diagonal elements.

Design variable	Description	Bounds
$x_1 = H$	Height of the roofing structure	$1 \div 3$
$x_2 = div_x$	Number of divisions in x direction	$6 \div 40$
$x_3 = div_y$	Number of divisions in y direction	$3 \div 20$
x_4	Section for the upper chord - beams in x direction	$0 \div 170$ CHS/IPE profiles' index from list
x_5	Section for the upper chord - beams in y direction	$0 \div 170$ CHS/IPE profiles' index from list
x_6	Section for the lower chord - beams in x direction	$0 \div 170$ CHS/IPE profiles' index from list
x_7	Section for the lower chord - beams in y direction	$0 \div 170$ CHS/IPE profiles' index from list
x_8	Section for diagonals	$0 \div 170$ CHS/Half HEA profiles' index from list (**Scenario 1**) $0 \div 201$ CHS/Half HEA/Glulam sections' index from list (**Scenario 2**)
x_9	Section for columns	$0 \div 150$ Glulam sections' index from list

Table 4.7: Design variables of the industrial building: red - Topology, Shape, Size; cyan - Cross-sections assignation

In Scenario 2, x_8 counts 31 extra cross-sections (rectangular glulam ones) in comparison to Scenario 1. To make this decision, only cross-sections that were dimensionally consistent with the standardized node used for this case study were picked from the catalogue utilized for columns. Furthermore, by selecting cross-seccataloging an aspect ratio less than 1.5, the chosen range was established.

As previously stated, with respect to the roof-only optimization case, the optimizer is allowed to choose between different classes of sections (opened or closed) and different materials (steel and wood) through the implementation of a binary variable according to Table 4.8.

Cross-section type	**Shape variable**
Closed steel section (CHS)	0
Open steel section (IPE/Half HEA)	1
Solid rectangular glulam section	2

Table 4.8: Shape variable definition

After all the establishment of the optimization parameters, space frame optimization, which entails the modules of the industrial building will be done simultaneously with respect to size, shape, and topology.

Focusing on the Objective Functions formulation, the structural OF (OF_1)is the same as the one used for the analysis of the truss structure, explained in section 3.4 with the equation 3.11:

$$minf(\mathbf{x})_1 = \overbrace{\sum_{i=1}^{N} \rho_i A_i l_i \cdot \phi_1 \cdot \phi_3}^{\text{Elements}} + \overbrace{M_{node} \cdot \phi_2}^{\text{Connections}} \quad [ton] \tag{4.6}$$

subjected to

$$\frac{N_{Ed} \cdot \gamma_{M1}}{\chi_y \cdot N_{Rk}} + k_{yy} \cdot \frac{M_{y,Ed} \cdot \gamma_{M1}}{\chi_{LT} \cdot M_{y,Rk}} + \frac{M_{z,Ed} \cdot \gamma_{M1}}{M_{z,Rk}} \leq 1 \tag{4.7}$$

from EC3 6.3.3(4)-6.61 (1993); to

$$\frac{\sigma_{c,0,d}}{k_{c,y} \cdot f_{c,0,d}} + k_m \cdot \frac{\sigma_{c,0,d}}{f_{m,y,d}} + \frac{\sigma_{m,z,d}}{f_{m,z,d}} \leq 1 \tag{4.8}$$

from EN 1995-1-6.3.2 (2004) and to

$$\begin{aligned} \delta_{max} &\leq \frac{L}{200} \quad for\ steel\ elements \\ \delta_{max} &\leq \frac{L}{150}\ to\ \frac{L}{300} \quad for\ timber\ elements \end{aligned} \tag{4.9}$$

respectively from NTC2018 and EN 1995-1-7.2.

In addition to steel elements' verifications, Eq. 4.8 includes structural checks for glulam components and further constrains the problem. Given that Karamba3D is limited to codes based on Eurocode 3, structural checks for timber have been incorporated through the use of a Python component. The script is documented in Appendix A.2.

It covers components that experience compression solely or combined with bending. Around the axis with the maximum slenderness ratio, the stability of these components is tested.

Buckling has a greater impact when the slenderness rate is high. The elements' slenderness and straightness (0.1 for Glulam) are taken into account by the parameters $k_{c,y}$ and $k_{c,z}$. The critical load, which is determined using the Euler buckling cases, in turn affects the slenderness. The prescribed buckling length factor varies depending on the kind of element and support conditions. Specifically, $\beta = 1$ is assumed for pinned-pinned supports (beams), and $\beta = 0.7$ for pinned-fixed ones (columns). k_m instead is a cross-sectional parameter, which is set equal to 0.7 for rectangular cross-sections.

With respect to the penalties, ϕ_1 and ϕ_2 correspond to those in Case study 1 (see Section 3.4). The only difference is that the utilization ratios derived from the Python script for glulam components are also fed into ϕ_1. The new penalty ϕ_3 is expressed as follows and relates to Serviceability Limit States (SLS) restrictions on the maximum deflection:

$$\phi_3 = 1 + (\delta_{max} - \delta_k) \tag{4.10}$$

where $\delta_{max} = 15\ cm$ is calculated from Standard codes and δ_k is the maximum displacement of the considered configuration.

In contrast to ϕ_1, which operates at the element level, ϕ_3 is applied to the configuration that the optimizer is examing. In fact, δ_{max} is calculated in relation to the building's shortest side, which acts as the check's binding dimension. In this instance as well, the penalty function ensures that ϕ_3 equals 1 when the maximum vertical deformation is less than that allowed by Eurocodes, validating the SLS check.

Furthermore, the environmental OF (OF_2) is now presented. The function has

the same form as OF_1 and is expressed as follows:

$$minf(\mathbf{x})_2 = \overbrace{\sum_{i=1}^{N} \rho_i A_i l_i \cdot GWP^{tot}_{beam/column} \cdot \phi_1 \cdot \phi_3}^{\text{Elements}} + \overbrace{M_{node} \cdot GWP^{tot}_{node} \cdot \phi_2}^{\text{Connections}} \quad [kgCO_2 - eq.] \quad (4.11)$$

where $GWP^{tot}_{beam/column}$ and GWP^{tot}_{node} are obtained as explained in Section 4.2. To provide a representative and comparative result for the considered building, the objective function's outcome, deprived of the penalties, is then divided by the Net Floor Area (NFA).

In contrast to Case study 1, since two materials are taken into account this time, the density, ρ, is included in the summation for both OF_1 and OF_2. Specifically, $\rho_{steel} = 7850\, kg/m^3$ for steel grade S355, whereas $\rho_{glulam} = 470\, kg/m^3$ for glulam 28h are adopted.

To guarantee that structurally feasible configurations are derived from both functions, the penalties imposed to OF_1 are also applied to OF_2.

Table 4.9 outlines the key parameters and settings used in the optimization algorithm.

Table 4.9: Optimization Algorithm Parameters and Settings

Parameter	Value
Maximum Iterations	100
Population Size	200
Mutation Probability	0.2
Crossover Probability	0.8
Convergence Threshold	0.001
Selection Mechanism	Tournament Selection
Penalty Functions	ϕ_1, ϕ_2, ϕ_3
Optimization Approach	Penalty-Based
Algorithm Integration	SPEA-II (Octopus Plug-in)

Chapter 5

Results - Case study 2: Industrial building

The outcomes of the industrial building optimizations have been summarized here, with a focus on differentiating between the two scenarios.

5.1 Scenario 1

By allowing single objectives to be improved simultaneously, a multi-objective optimization approach expands on the concept of optimization and produces a range of trade-off solutions that are considered equally optimal. More specifically, Figure 5.1 displays the whole spectrum of individuals. The feasible decision space is identified by zooming in, and the Pareto-optimal front, i.e. the non-dominated set inside this space, is brought to light (see Figure 5.7).

Usually, there isn't an acceptable solution in multi-objective optimization that minimizes each function at once. As a result, focus is placed on the Pareto optimum solutions mentioned above, i.e. solutions that cannot be enhanced in any one of the objectives without compromising at least one of the others.

The goal of resolving a multi-objective optimization issue is to assist a decision maker in identifying the most favored Pareto optimum solution based on subjective preferences when decision-making is prioritized. Based on the decision maker's preference information, many philosophies can be used to find the most desired

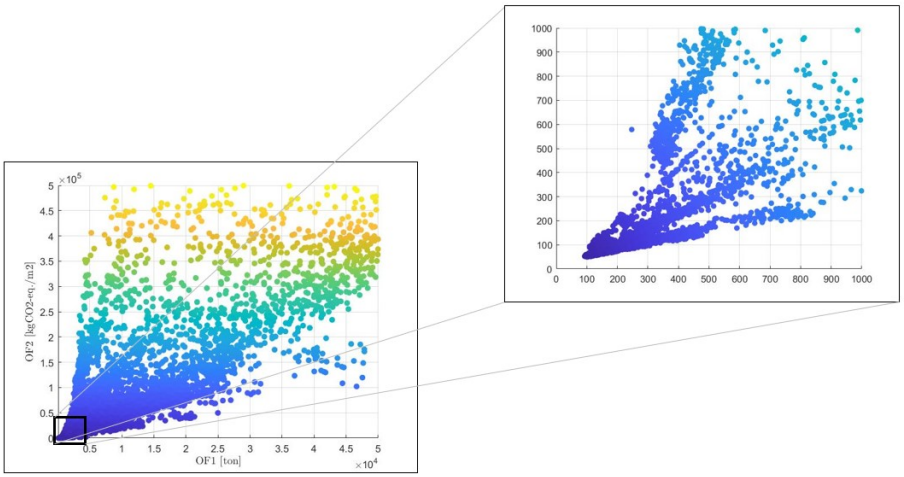

Figure 5.1: Spectrum of individuals of Scenario 1 (Population size: 200 - Generations: 100)

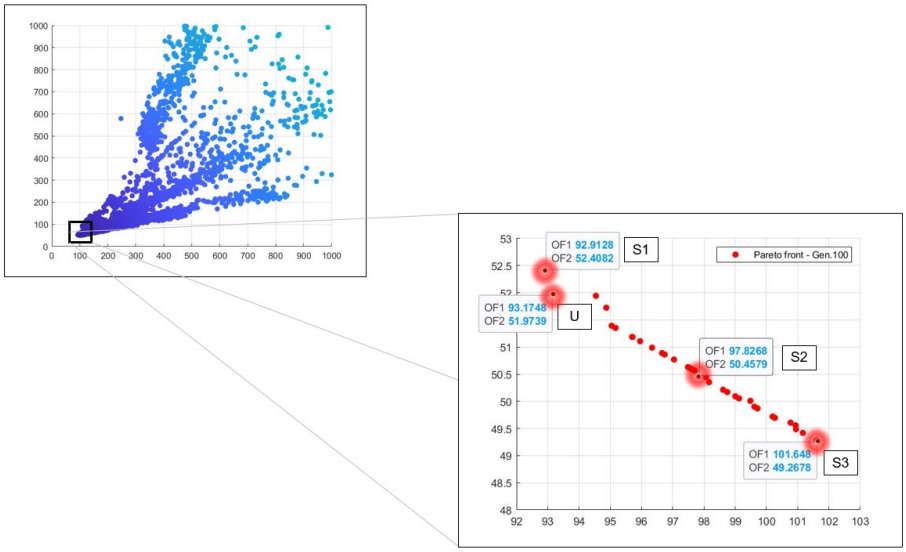

Figure 5.2: Zoom on the Pareto-optimal front of Scenario 1

outcomes.

The *Utopia point* (U-point), which can be identified by finding the intersection of the maximum/minimum value of one objective function with the maximum/minimum value of the other objective function (2018), is the mathematically optimal solution inside the optimal Pareto front (see Figure 5.3). The optimum outcome can be found by seeking the lowest Euclidean distance between the U-point and the non-dominated frontal solutions. This is the method applied in this instance and

the calculation is done as follows:

$$d = min\sqrt{(x_i - x_U)^2 + (y_i - y_U)^2} \tag{5.1}$$

where x_i, y_i are the coordinates of the i non-dominated solution and x_U, y_U are the coordinates of the Utopia point.

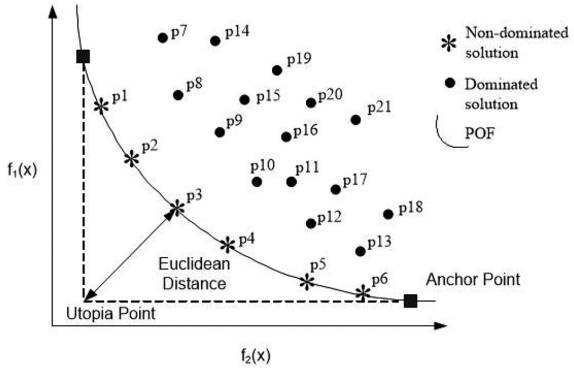

Figure 5.3: Utopia point determination (taken from 2018)

As shown in Figure 5.7, three additional alternatives (the solutions at the front's extremes and the intermediate solution, which is the one closest to the mean value) have been considered in order to look into potential variability within the optimal Pareto front.

The results in terms of optimized design variables and OF are shown in Table for simplicity's sake.

The values of the penalties for the solutions under consideration are reported in Table 5.2 for completeness. The fact that the structural penalties equal 1 indicates that there are no unfeasible elements and that the maximum acceptable deflection requirement is met, respectively. As said, ϕ_2 is constant and reliant on the configuration's node count. The outcomes in Table 5.1 are filtered out of the penalties' values.

The same geometric properties may be observed in all of the optimized configurations. This is clear by looking at the OFs: the environmental and the structural ones differ from the utopian solution by a maximum of 5% and 8%, respectively. The optimal design for the U-point solution is reported in Figure 5.4 for representativeness, since there is visually no noticeable difference between the configurations. In Appendix C.2, front and lateral views are provided.

	U-point solution	S1	S2	S3
OF_1	93.17	92.91	97.83	101.65
OF_2	51.97	52.41	50.46	49.27
H	3	3	3	3
div_x	6	6	6	6
div_y	3	3	3	3
Up long.	CHS 355.6x6.3	CHS 406.4x6	CHS 355.6x6.3	CHS 355.6x6.3
Up transv.	CHS 406.4x6	CHS 406.4x6	CHS 406.4x6	CHS 406.4x6
Low long.	CHS 139.7x3	CHS 114.3x2.5	CHS 114.3x2.5	CHS 114.3x2.5
Low transv.	CHS 139.7x3	CHS 114.3x3	CHS 139.7x4	CHS 139.7x5
Diagonals	CHS 219.1x5	CHS 219.1x5	CHS 219.1x5	CHS 219.1x5
Columns	GL130x874	GL215x456	GL215x988	GL265x1102

Table 5.1: Results of the best solutions for Scenario 1

	U-point solution	S1	S2	S3
ϕ_1	1	1	1	1
ϕ_2	50.6	50.6	50.6	50.6
ϕ_3	1	1	1	1

Table 5.2: Penalties results for Scenario 1

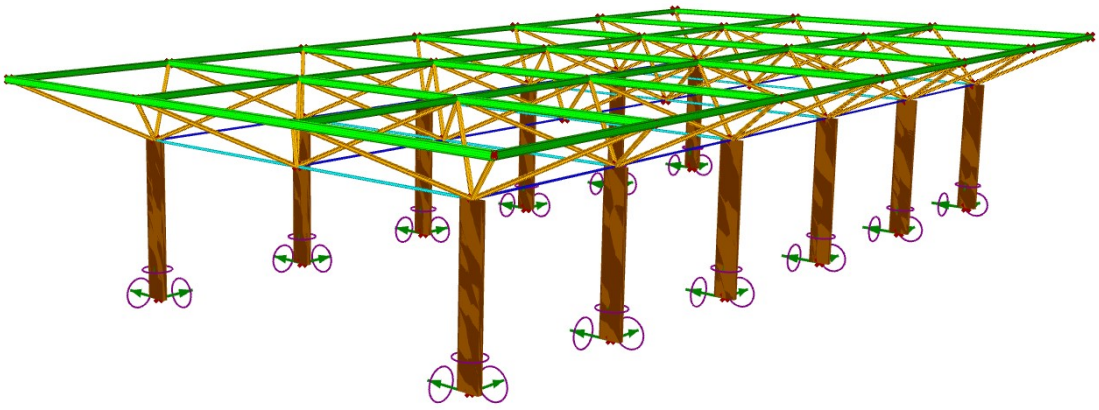

Figure 5.4: Configuration of the optimized industrial building - U-point solution

This relatively small variation results from how the cross-sections are assigned. Specifically, the diagonals' assigned cross-section is the same. This may be because diagonals in this type of structure essentially operate as a bridge to balance the

load imposed on the chords. On the contrary, slight differences in terms of assigned sections can be observed with specific regard to upper and lower chords.
Instead, the system observes a distinct cross-section assigned to columns. This is accurate to achieve a satisfactory equilibrium between the two OFs. Based on the findings presented in Section 4.2, steel has a significantly higher environmental effect than glulam. Consequently, the presence of more timber leads to a better reduction in OF_2.
With respect to the shape variable that was defined for this case study, it can be determined that for each cluster of beams, closed steel sections are favored. This may be because, in comparison to open sections, CHS sections offer stronger torsional strength and high structural capacity in both directions.

In terms of the geometric layout, meaning the number of divisions in both x and y directions, the optimizer primarily prefers to operate with fewer modules, or more accurately, with the lowest values conceivable within the range (6 in the x direction and 3 in the y direction). This decision can be justified by the fact that as the number of divisions rises, so does the number of components. Naturally, this has a significant effect on the structure's overall mass as well as the associated emissions. The height of the roof, H, is the other geometric variable and it is equal in all optimal designs to 3 m. Because the value in this instance trends toward the upper bound of the variable's range, the tendency is contrary to the one of the divisions. The distribution of stresses among the elements is aided by this choice.

After the introduction and analysis of each result, the various components can be distinguished in order to give the outcomes some additional thought. In particular some observations may be performed by examining Figure 5.5. Evidently, the number of nodes and the GWP associated with connections are constant as each of the four designs has a 6x3 divisions configuration. These components need precise manufacturing techniques, which result in a larger embodied carbon footprint, even if they are composed of the same material as beams and have a comparable mass.

The differences for beams conform to the previously described relatively small fluctuations. In order to enhance the numerical comprehension of the discrepancies, the percentage difference between S1, S2, and S3 in relation to the U-point solution for each component is provided in Table 5.3. There is no distinction between GWP and Mass results since they share the same percentage differences due to the

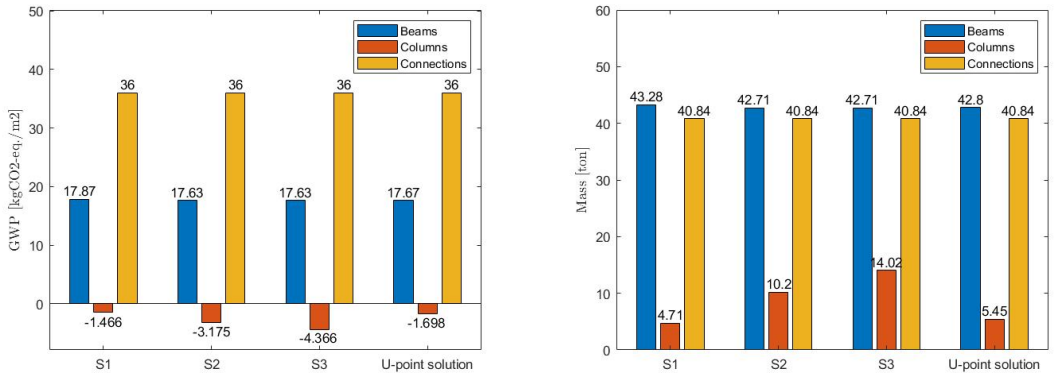

(a) GWP (b) Mass

Figure 5.5: GWP and Mass outcomes for each component

proportionality between the two.

	S1	**S2**	**S3**
Beams	1.14%	-0.22%	-0.22%
Columns	-14%	87%	157%
Connections	0%	0%	0%

Table 5.3: Percentage difference for each component with respect to optimal U-point solution

Major improvements are observed in the columns: as predicted, a larger cross-section, so higher mass, yields more compelling results, particularly in S3, which is the solution that minimizes the environmental OF the greatest amount at the expense of the structural one.

Axial stress and bending moment diagrams have been presented in Appendix C.2 so that the structural characteristics of the optimized construction may be seen in detail.

Instead, the displacements of the structural components are given here (see Figure). Higher displacements are shown in red. The structure has undergone a maximum displacement of 13 cm, which is less than the maximum limit required by SLS criteria.

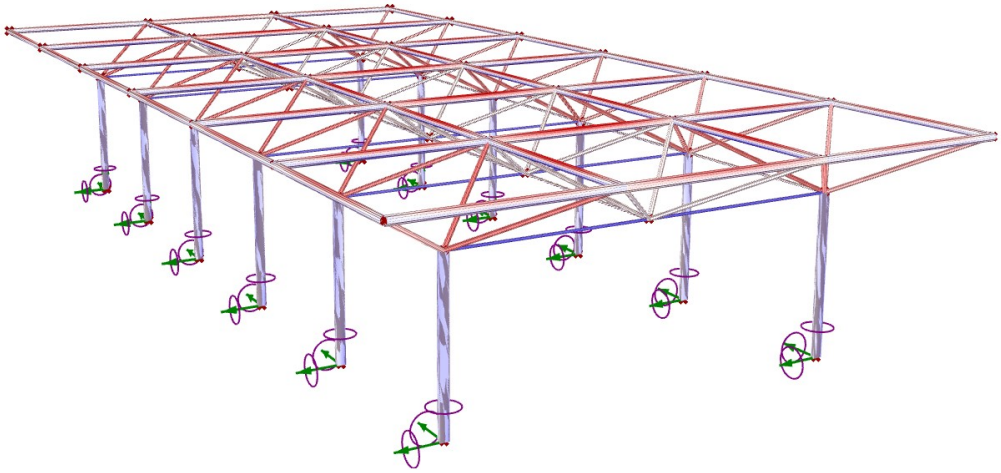

Figure 5.6: Displacements of U-point optimal solution

5.2 Scenario 2

The second scenario differs from the first as it introduces a more extensive cross-section list for diagonal members, which includes glulam sections, as was previously discussed in Chapter 4. This decision is the product of an in-depth examination of the potential benefits related to mass and GWP reduction.

In Figure 5.7, from the whole spectrum of individuals, a zoom on the Pareto-optimal front is reported.
In this instance, the front displays a nearly parabolic tendency, succeeded by a linear branch with greater population density.

The Utopian point method is used in this instance as well to determine the Pareto-optimal front's best solution. Once more, three further solutions are examined: the front's two extremes and a compelling intermediate solution.
The results in terms of optimized design variables and OF are shown in Table 5.4. For completeness, the values of the penalties for the solutions under consideration are reported in Table 5.5 for completeness.

The structural penalties, ϕ_3 and ϕ_1, equaling 1 means that the maximum allowable deflection requirement is satisfied and there are no elements that are not feasible. This means that also in this case, both penalties are operating as intended. Meanwhile, ϕ_2 is constant and depends on the number of nodes of the arrangement.

It is possible to detect quite comparable geometric features in any optimal ar-

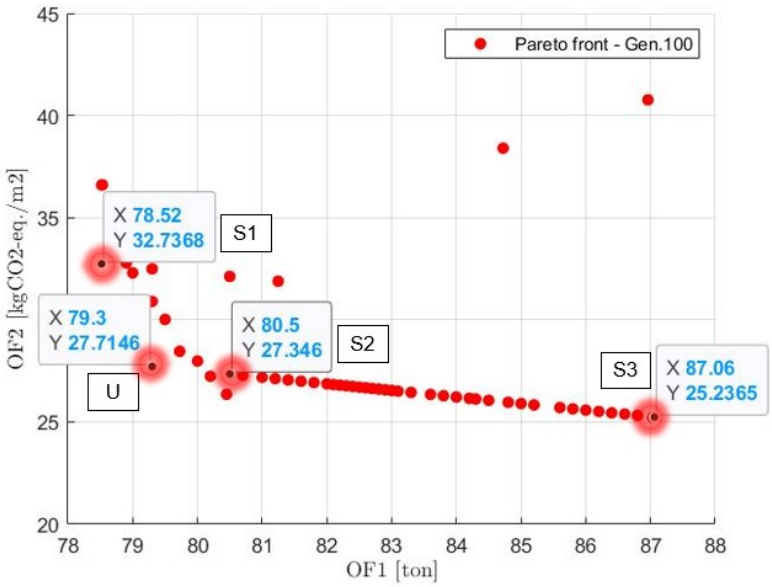

Figure 5.7: Zoom on the Pareto-optimal front of Scenario 2

	U-point solution	**S1**	**S2**	**S3**
OF_1	79.3	79.3	80.51	87.06
OF_2	27.71	32.74	27.35	25.24
H	3	3	3	3
div_x	6	6	6	6
div_y	3	3	3	3
Up long.	CHS 355.6x6.3	CHS 355.6x6.3	CHS 355.6x6.3	CHS 355.6x6.3
Up transv.	CHS 406.4x6	CHS 406.4x6	CHS 406.4x6	CHS 406.4x6
Low long.	CHS 114.3x2.5	CHS 114.3x2.5	CHS 114.3x2.5	CHS 88.9x3
Low transv.	CHS 139.7x4	CHS 139.7x4	CHS 139.7x4	CHS 114.3x5
Diagonals	GL 365x570	GL 365x418	GL 365x570	GL 365x570
Columns	GL215x608	GL215x532	GL315x494	GL215x1368

Table 5.4: Results of the best solutions for Scenario 2

	U-point solution	**S1**	**S2**	**S3**
ϕ_1	1	1	1	1
ϕ_2	50.6	50.6	50.6	50.6
ϕ_3	1	1	1	1

Table 5.5: Penalties results for Scenario 2

rangement. The OFs make this evident: the structural and environmental ones deviate from the utopian solution by a maximum of 9% and 15%, respectively. The small discrepancy arises once more from the assignment of the cross-sections.

The U-point solution's optimal design is presented in Figure 5.8 for representativeness, as there isn't a discernible visual difference between the configurations. Front and lateral views are included in Appendix C.3.

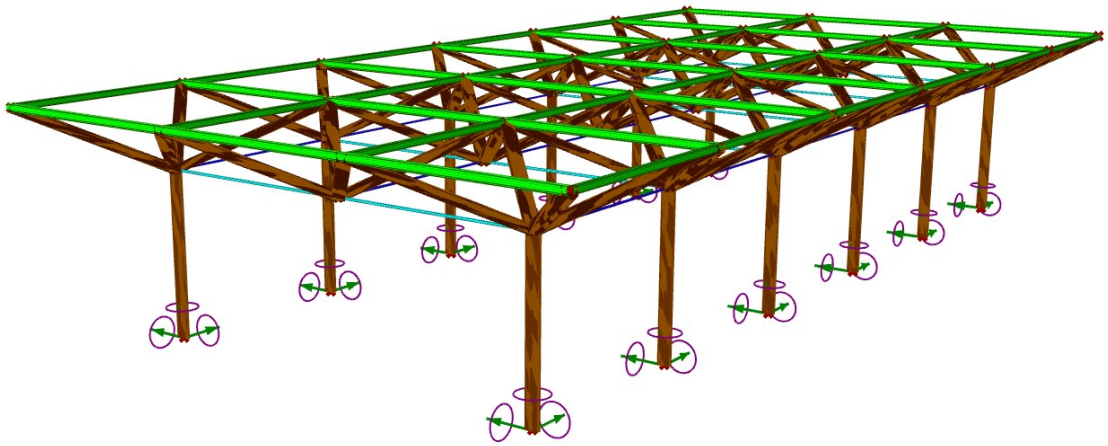

Figure 5.8: Configuration of the optimized industrial building - U-point solution

It is evident from both the graphic representation and the table of the design variables that the primary innovation of this scenario is that the optimizer selected only mixed-material configurations with glulam diagonals. This could be because wood has a density that is significantly lower than that of steel, which aids in the creation of lightweight solutions.

Inside the configurations, the steel components are comparatively equal. This may be because the optimizer identified elements that operate at their maximum capacity, validating the structural specifications.
Conversely, there are slight discrepancies in the designated sections, particularly concerning diagonals and columns. This is correct in order to bring the two OFs into an appropriate equilibrium. Thus, more wood results in a more effective decrease of OF_2.
In relation to the shape variable, closed steel sections are preferred for each chord cluster, whereas rectangular glulam sections are assigned to diagonals. For steel elements, the use of closed sections rather than open ones can be justified as in Section 5.1.

Regarding the geometric arrangement, in particular the amount of divisions in both the x and y directions, the optimizer again favors operating with 6 divisions in the x direction and 3 in the y direction. In terms of roof height, H, all optimal designs have a height of 3 m.

After the findings are introduced, by looking at Figure 5.9, each component may be distinguished once again to give the results some more consideration, just as for Scenario 1.

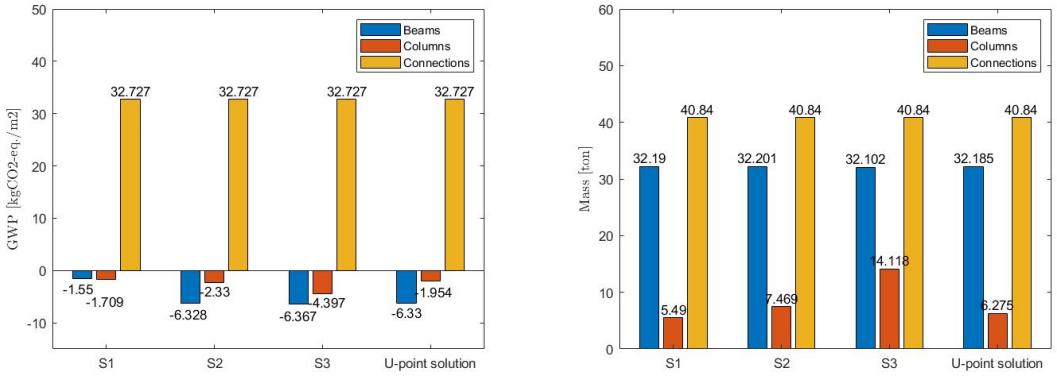

(a) GWP (b) Mass

Figure 5.9: GWP and Mass outcomes for each component

Since each of the four designs has a 6x3 divisions layout, both the number of connections and the GWP associated to them remain constant. Due to its production-related carbon impact, nodes' contribution continues to be significant.

In beams, remarkable tendencies are observed. This contribution is significantly impacted by the optimizer's decision to employ wood sections. The GWP associated with beams in Scenario 1 was predominantly positive, but in this instance, the presence of timber diagonals is robust enough to reduce the embodied energy associated with these components.

Furthermore, even when larger sections are allocated to columns, the gain associated with diagonal elements is greater than that of columns since diagonals are quantitatively six times more than vertical elements.

To further clarify the numerical understanding of the differences within the results, Table 5.6 presents the percentage difference between S1, S2, and S3 with respect to the U-point solution for each component.

	Mass			**GWP**		
	S1	S2	S3	S1	S2	S3
Beams	0.01%	0.05%	-0.26%	75%	0.04%	-0.55%
Columns	-12.50%	19.04%	125%	12%	-19%	-125%
Connections	0%	0%	0%	0%	0%	0%

Table 5.6: Percentage difference for each component with respect to optimal U-point solution

Appendix C.3 contains axial stress and bending moment diagrams that provide for a detailed view of the optimized construction's structural characteristics. Because Karamba3D does not allow for the setting of multiple scales of representation, the bending moment diagrams presented in the Appendices for both Scenarios only display the bending moment acting on the upper chord. This does not imply that the diagonal and lower chord elements are not bent.
Rather, the structural component displacements are shown here in Figure.

The largest displacement that the structure has experienced is 14 cm, which is less than the maximum displacement that the SLS criterion demands.

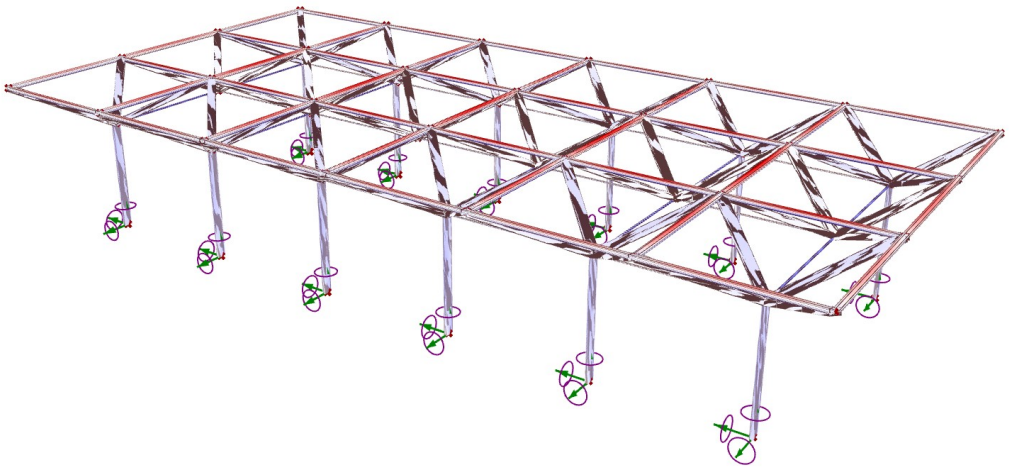

Figure 5.10: Displacements of U-point optimal solution

Chapter 6

Conclusions and future developments

The integration of LCA analysis into an optimization tool for the best design of 3D spacial trusses is the primary objective of this Thesis. Aiming at the definition of a consistent approach for the early design stages, the constructability aspects go hand-in-hand with mass and embodied impact reduction.
Two different case studies have been investigated: the first mainly focused on detecting the best clustering strategy of the elements for the minimum structural cost and assemblage complexity. At this stage, in fact, we wondered which solution the optimizer would choose between a huge number of nodes and slender components or, on the contrary, fewer subdivisions with heavier sections; while the second has been inspired by real-world similar large structures in which the simultaneous structural efficiency and environmental impact aspects have been addressed by considering two types of material, i.e. steel and wood.
In both case studies, the definition of the model, the assembly phase, and the load evaluation have been clearly described. Only wind action has been calculated because of their critical effect on this type of structure.

Starting from the roof-level-only analysis, an optimization procedure has been implemented aiming to identify the impact of constructability issue, as the number of nodes on the overall weight, for different clustering strategies of the elements. By imposing a specific penalty for the number of nodes, the optimal design has been

obtained with the minimum number of nodes and final sizing of the steel according to European standard regulation.

It is interesting to observe that the number of nodes is dramatically reduced as well as the number of components constituting the structure due to the significant weight of the connections. For all the investigated scenarios, independently of the number of different sections considered, the least weight configuration has been obtained for the minimum value of subdivisions equal to 6 and 3 along the x and y axes, respectively. The only exception has been reported by configuration A for which the number of subdivisions along the x direction has grown to 7 due to the assumption of only one section assigned to all the elements. However, it is worth noting that the connection plays a crucial role already at the structural cost level.

As expected, by increasing the number of different cross-sections, the total weight of the trussed roof decreases while the number of subdivisions as well as the number of nodes remain constant at the minimum value.

Making a comparison with real-world applications of similar structures, it can be observed a significant difference in terms of the arrangement of the final truss layout. Designers usually prefer solutions with a higher number of nodes and slender elements. On the contrary, the optimal solution provided by the optimizer seems to move toward the opposite trend.

Most significant changes can be observed when it moves toward the second case study. Despite the previous approach, the optimization problem has been focused on the simultaneous minimization of structural and environmental costs of a complex building. The latter has been obtained by implementing the LCA analysis for the definition of the considered activities and the calculation of the corresponding $CO_2 - eq.$ emission.

In the first scenario, a multi-objective optimization has been performed and the Pareto front of optimal solutions has been pointed out. Steel sections only have been considered by maintaining a proper penalty in order to reduce the overall structural complexity expressed in terms of the number of nodes.

Four different optimal designs have been identified as the best solutions among all the sets of optimal solutions that live in the Pareto front. Due to the nature of the Pareto Front representation, the choice of the best solution depends on the sensibility of the designer and/or the final task of the community. The 4 selected solutions

represent the best configurations in terms of minimum structural cost, environmental cost, or as the optimal compromise between these two fighting aspects.

As in the previous weight-only optimization case, all the selected best configuration has been obtained when the minimum number of subdivision has been imposed. Moreover, the importance of the connection on the total OF has been observed again. As reported in Figure 5.5, the total GWP and total mass is entirely governed by the number of nodes. Specifically, for the assessment of the total environmental cost, the GWP related to connections is higher than the sum of the contributions of beams and columns. The same trend has been recognized for the evaluation of the structural cost for which the weight of the connections only is comparable with that of the elements composing the roof. Differently from the first scenario, timber elements could be chosen by the optimizer for diagonals and columns. For this reason, ULS timber elements' structural verification has been implemented as well as SLS requirements verification for the maximum deflection. Additionally, the positions of the columns, along the longest sides of the structure, have been assumed as new variables of the optimization problem.

Based on the results coming from the two case studies and for the two constructive options, it is possible to demonstrate that configurations with the fewest number of divisions in both directions and the maximum allowable value of height are the solutions preferred by the optimizer. Adding realistic constraints related, for example, to stricter transportability, manufacturing conditions, and feasibility of the connections does not affect appreciably the final design which seems to be stable with a minimum number of subdivisions. Nevertheless, the cross-section assignment yields some interesting mixed-material configurations: adding timber sections can result in optimum solutions that are both lighter and environmentally acceptable.

In conclusion, the main novelty of the proposed methodology is the successful integration of LCA analyses into the Grasshopper environment which enables real-time feedback on the building's environmental performance for supporting decision-makers in an easier and faster matter. Moreover, the structural complexity has been addressed and involved in the multi-objective problem formulation aiming to assess the most sustainable design solution by avoiding constructability issues during the construction process and a dramatic increase in the total cost of the structure.

Finally, all the proposed optimal design seems to disagree with the common design solutions adopted for real-world similar structures where the huge number of nodes and beams leads to non-environmental-friendly solutions and lower structural efficiency.

The LCA analyses are integrated by matching material and processes with selected suitable environmental datasets. From the technical perspective, such an "add-on" can be further developed in the more complex and dedicated plug-in for the Grasshopper environment. In order to provide more intuitive input selection, it could be helpful to allow, e.g., higher automation and interoperability between the parametric design tools and an external environmental database. If this will result, on the one hand, in an API aimed at the integration of more complex analyses, on the other hand, its development and application could be challenging due to the limited computational capacities of informatics instruments.

In light of the findings, it is crucial to emphasize that steel continues to be one of the priciest and environmentally challenging materials, due to its current energy-intensive production processes. This has been particularly proven in steel connections, for which structural design optimization alone cannot cut significantly emissions (2016).

Nowadays it is frequently common to combine steel with wood elements. Blending these two resources may be an interim approach to enhance the environmental and technical performance of the structure. Steel is reusable and recyclable, with recycling rates that range between 81-98 % (2014). Hence, this should be possibility more exploited. All in all, the optimization of the design should take place simultaneously with an improvement and optimization of the processes (e.g. by using renewable energy for manufacturing processes and producing less material wastes). This could help to achieve lower use of resources as well as higher decarbonization rates. Such an observation can be extended for bio-based materials as well, e.g. timber elements, which applicability on a larger scale should be commensurate with the wood availability and, therefore, of productive forestry availability (2022).

In future developments, alternative solutions and new production processes of steel and wood components could be investigated in the LCA analysis aiming to achieve comparable effects between connections and other components both in terms

of sustainability and total structural cost. Moreover, transport and reusing could be integrated in a future development allowing a comprehensive and realistic evaluation of the GWP impact derived by all the industrial stages.

Chapter 7

Bibliography

S. N. Al-Saadi and K. S. Al-Jabri. Optimization of envelope design for housing in hot climates using a genetic algorithm (ga) computational approach. *Journal of Building Engineering*, 32:101712, 2020.

M. K. Ansah, X. Chen, and H. Yang. Two-stage lifecycle energy optimization of mid-rise residential buildings with building-integrated photovoltaic and alternative composite façade materials. *Buildings*, 11(12):642, 2021.

E. Antipova, D. Boer, G. Guillén-Gosálbez, L. F. Cabeza, and L. Jiménez. Multi-objective optimization coupled with life cycle assessment for retrofitting buildings. *Energy and Buildings*, 82:92–99, 2014.

P. A. T. Arpini, M. C. Loureiro, B. D. Breda, A. F. Calenzani, and É. C. Alves. Optimum design of a composite floor system considering environmental and economic impacts. *Revista IBRACON de Estruturas e Materiais*, 15, 2021.

F. Ascione, R. F. De Masi, F. de Rossi, S. Ruggiero, and G. P. Vanoli. Optimization of building envelope design for nzebs in mediterranean climate: Performance analysis of residential case study. *Applied energy*, 183:938–957, 2016.

F. Ascione, N. Bianco, C. De Stasio, G. M. Mauro, and G. P. Vanoli. Casa, cost-optimal analysis by multi-objective optimisation and artificial neural networks: A new framework for the robust assessment of cost-optimal energy retrofit, feasible for any building. *Energy and Buildings*, 146:200–219, 2017.

F. Ascione, N. Bianco, G. M. Mauro, and G. P. Vanoli. A new comprehensive framework for the multi-objective optimization of building energy design: Harlequin. *Applied Energy*, 241:331–361, 2019.

S. Ashtul and S. Patil. Review on study of space frame structure system. *Int. Res. J. Eng. Technol*, 2020.

U.-P. Baustähle. Offene walzprofile und grobbleche. Technical report, EPD-BFS-20180116-IBG2-DE, ausgestellt am 25.10. 2018, gültig bis 24.10. 2023 . . . , 2018.

B. Björkman and C. Samuelsson. Recycling of steel. In *Handbook of recycling*, pages 65–83. Elsevier, 2014.

N. C. Brown and C. T. Mueller. Design for structural and energy performance of long span buildings using geometric multi-objective optimization. *Energy and Buildings*, 127:748–761, 2016.

C. Brunelli, F. Castellani, A. Garinei, L. Biondi, and M. Marconi. A procedure to perform multi-objective optimization for sustainable design of buildings. *Energies*, 9(11):915, 2016.

J. Brütting, G. Senatore, and C. Fivet. Optimization formulations for the design of low embodied energy structures made from reused elements. In *Advanced Computing Strategies for Engineering: 25th EG-ICE International Workshop 2018, Lausanne, Switzerland, June 10-13, 2018, Proceedings, Part I 25*, pages 139–163. Springer, 2018.

J. Brütting, G. Senatore, M. Schevenels, and C. Fivet. Optimum design of frame structures from a stock of reclaimed elements. *Frontiers in Built Environment*, 6: 57, 2020a.

J. Brütting, C. Vandervaeren, G. Senatore, N. De Temmerman, and C. Fivet. Environmental impact minimization of reticular structures made of reused and new elements through life cycle assessment and mixed-integer linear programming. *Energy and Buildings*, 215:109827, 2020b.

O. Bucklin, R. Di Bari, F. Amtsberg, and A. Menges. Environmental impact of a mono-material timber building envelope with enhanced energy performance. *Sustainability*, 15(1):556, 2022.

L. Caldas, L. Norford, and J. Rocha. An evolutionary model for sustainable design. *Management of Environmental Quality: An International Journal*, 14(3):383–397, 2003.

L. G. Caldas and L. K. Norford. A design optimization tool based on a genetic algorithm. *Automation in construction*, 11(2):173–184, 2002.

L. G. Caldas and L. K. Norford. Genetic algorithms for optimization of building envelopes and the design and control of hvac systems. *J. Sol. Energy Eng.*, 125 (3):343–351, 2003.

C. V. Camp and F. Huq. Co2 and cost optimization of reinforced concrete frames using a big bang-big crunch algorithm. *Engineering Structures*, 48:363–372, 2013.

E. Ching and J. V. Carstensen. Truss topology optimization of timber–steel structures for reduced embodied carbon design. *Engineering Structures*, 252:113540, 2022.

D. A. Coley and S. Schukat. Low-energy design: combining computer-based optimisation and human judgement. *Building and Environment*, 37(12):1241–1247, 2002a.

D. A. Coley and S. Schukat. Low-energy design: combining computer-based optimisation and human judgement. *Building and Environment*, 37(12):1241–1247, 2002b.

G. Databases. Gabi software system, sphera solutions gmbh, lbp-gabi, 2011.

G. F. de Medeiros and M. Kripka. Optimization of reinforced concrete columns according to different environmental impact assessment parameters. *Engineering Structures*, 59:185–194, 2014.

C. Diakaki, E. Grigoroudis, N. Kabelis, D. Kolokotsa, K. Kalaitzakis, and G. Stavrakakis. A multi-objective decision model for the improvement of energy efficiency in buildings. *Energy*, 35(12):5483–5496, 2010.

M. P. Drewniok, J. Campbell, and J. Orr. The lightest beam method–a methodology to find ultimate steel savings and reduce embodied carbon in steel framed buildings. In *Structures*, volume 27, pages 687–701. Elsevier, 2020.

T. M. Echenagucia, A. Capozzoli, Y. Cascone, and M. Sassone. The early design stage of a building envelope: Multi-objective search through heating, cooling and lighting energy performance analysis. *Applied energy*, 154:577–591, 2015.

C. EN. 15978: 2011 sustainability of construction works—assessment of environmental performance of buildings—calculation method. *CEN: Brussels, Belgium*, 2011.

C. Ö. EN. 14080: 2013 08 01: Timber structures—glued laminated timber and glued solid timber—requirements. *European Committee for Standardization: Brussels, Belgium*, 2013.

D. EN. 15804: Environmental product declaration core rules for building products. 2022.

F. Flager, B. Welle, P. Bansal, G. Soremekun, and J. Haymaker. Multidisciplinary process integration and design optimization of a classroom building. *Journal of Information Technology in Construction (ITcon)*, 14(38):595–612, 2009.

J. Gantner, B. Wittstock, K. Lenz, M. Fischer, K. Sedlbauer, J. Anderson, T. Saunders, Z. Gyetvai, C. Carter, A. Braune, et al. Eebguide guidance document part b:

Buildings. *Operational Guidance for life Cycle Assessment Studies of the Energy-Efficient Buildings Initative; Fraunhofer Institut für Bauphysik: Stuttgart, Germany*, 2015.

T. García-Segura and V. Yepes. Multiobjective optimization of post-tensioned concrete box-girder road bridges considering cost, co2 emissions, and safety. *Engineering Structures*, 125:325–336, 2016.

P. Gatheeshgar, K. Poologanathan, S. Gunalan, K. D. Tsavdaridis, B. Nagaratnam, and E. Iacovidou. Optimised cold-formed steel beams in modular building applications. *Journal of Building Engineering*, 32:101607, 2020.

F. Gilles, S. Bernard, A. Ioannis, and R. Simon. Decision-making based on network visualization applied to building life cycle optimization. *Sustainable cities and society*, 35:565–573, 2017.

H. Gross. Glulam handbook. *Gross Produktion AB, Stockholm, Sweden*, 2013.

S. A. Guimarães, D. Klein, A. F. G. Calenzani, and É. C. Alves. Optimum design of steel columns filled with concrete via genetic algorithm: environmental impact and cost analysis. *REM-International Engineering Journal*, 75:117–128, 2022.

N. Gunantara. A review of multi-objective optimization: Methods and its applications. *Cogent Engineering*, 2018.

IEA. Iea report (2022). *Buildings, Paris*, 2022.

ISO. 14044: Environmental management: life cycle assessment; requirements and guidelines. 14044, 2006a.

ISO. 14040: Environmental management—life cycle assessment—principles and framework. *Environmental management—life cycle assessment—principles and framework*, pages 235–248, 2006b.

C. Jiang, C. Tang, H.-P. Seidel, and P. Wonka. Design and volume optimization of space structures. *ACM Transactions on Graphics (TOG)*, 36(4):1–14, 2017.

A. Kaveh and A. Kaveh. Cost and co 2 emission optimization of reinforced concrete frames using enhanced colliding bodies optimization algorithm. *Applications of Metaheuristic Optimization Algorithms in Civil Engineering*, pages 319–350, 2017.

N. D. Lagaros. The environmental and economic impact of structural optimization. *Structural and Multidisciplinary Optimization*, 58(4):1751–1768, 2018.

K. Li, L. Pan, W. Xue, H. Jiang, and H. Mao. Multi-objective optimization for energy performance improvement of residential buildings: A comparative study. *Energies*, 10(2):245, 2017.

S. Longo, F. Montana, and E. R. Sanseverino. A review on optimization and cost-optimal methodologies in low-energy buildings design and environmental considerations. *Sustainable cities and society*, 45:87–104, 2019.

C. Loss, M. Piazza, and R. Zandonini. Connections for steel–timber hybrid prefabricated buildings. part ii: Innovative modular structures. *Construction and Building Materials*, 122:796–808, 2016.

Y. Lu, S. Wang, Y. Zhao, and C. Yan. Renewable energy system optimization of low/zero energy buildings using single-objective and multi-objective optimization methods. *Energy and Buildings*, 89:61–75, 2015.

L. Magnier and F. Haghighat. Multiobjective optimization of building design using trnsys simulations, genetic algorithm, and artificial neural network. *Building and Environment*, 45(3):739–746, 2010.

W. Marks. Multicriteria optimisation of shape of energy-saving buildings. *Building and environment*, 32(4):331–339, 1997.

D. Martínez-Muñoz, J. García, J. Martí, and V. Yepes. Discrete swarm intelligence optimization algorithms applied to steel–concrete composite bridges. *Engineering Structures*, 266:114607, 2022.

D. Mavrokapnidis, C. C. Mitropoulou, and N. D. Lagaros. Environmental assessment of cost optimized structural systems in tall buildings. *Journal of Building Engineering*, 24:100730, 2019.

R. McNeel et al. Rhinoceros 3d, version 6.0. *Robert McNeel & Associates, Seattle, WA*, 2010.

L. Mei and Q. Wang. Structural optimization in civil engineering: a literature review. *Buildings*, 11(2):66, 2021.

M. Mensinger and L. Huang. Optimized preliminary structural design of steel composite buildings using the sustainable office designer: Comparing optimizations to satisfy different objectives. *Steel Construction*, 10(1):17–22, 2017.

E. Mostavi, S. Asadi, and D. Boussaa. Development of a new methodology to optimize building life cycle cost, environmental impacts, and occupant satisfaction. *Energy*, 121:606–615, 2017.

K. Negendahl and T. R. Nielsen. Building energy optimization in the early design stages: A simplified method. *Energy and Buildings*, 105:88–99, 2015.

NTC18. Norme tecniche per le costruzioni, 2018.

Ökobaudat. Ökobaudat. 2019.

H. S. Park, H. Lee, Y. Kim, T. Hong, and S. W. Choi. Evaluation of the influence of design factors on the co2 emissions and costs of reinforced concrete columns. *Energy and Buildings*, 82:378–384, 2014.

E. Parliament and the Council of the European Union. Directive 2002/91/ec of the european parliament and of the council of 16 december 2002 on the energy performance of buildings. *Official Journal of the European Communities*, 1:65–71, 2003.

I. Paya-Zaforteza, V. Yepes, A. Hospitaler, and F. Gonzalez-Vidosa. Co2-optimization of reinforced concrete frames by simulated annealing. *Engineering Structures*, 31(7):1501–1508, 2009.

V. Penadés-Plà, T. García-Segura, and V. Yepes. Accelerated optimization method for low-embodied energy concrete box-girder bridge design. *Engineering Structures*, 179:556–565, 2019.

C. Preisinger. Linking structure and parametric geometry. *Architectural Design*, 83 (2):110–113, 2013.

C. Quaglia, N. Yu, A. Thrall, and S. Paolucci. Balancing energy efficiency and structural performance through multi-objective shape optimization: Case study of a rapidly deployable origami-inspired shelter. *Energy and Buildings*, 82:733–745, 2014.

B. Raphael. Multi-criteria decision making for collaborative design optimization of buildings. *Built Environment Project and Asset Management*, 1(2):122–136, 2011.

M. Röck, M. R. M. Saade, M. Balouktsi, F. N. Rasmussen, H. Birgisdottir, R. Frischknecht, G. Habert, T. Lützkendorf, and A. Passer. Embodied ghg emissions of buildings–the hidden challenge for effective climate change mitigation. *Applied Energy*, 258:114107, 2020.

J. F. Santoro and M. Kripka. Minimizing environmental impact from optimized sizing of reinforced concrete elements. *Computers and Concrete*, 25(2):111, 2020.

Y. Schwartz, R. Raslan, and D. Mumovic. Implementing multi objective genetic algorithm for life cycle carbon footprint and life cycle cost minimisation: A building refurbishment case study. *Energy*, 97:58–68, 2016.

B. Standard. Eurocode 3—design of steel structures—. *BS EN*, 1(1):2005, 1993.

B. Standard et al. Eurocode—basis of structural design. *Eurocode 0*, 2002.

K. Suga, S. Kato, and K. Hiyama. Structural analysis of pareto-optimal solution sets for multi-objective optimization: An application to outer window design problems using multiple objective genetic algorithms. *Building and Environment*, 45(5): 1144–1152, 2010.

A. Tedeschi and D. Lombardi. The algorithms-aided design (aad). *Informed Architecture: Computational Strategies in Architectural Design*, pages 33–38, 2018.

D. E. The European Union Per Regulation 305/2011, Directive 98/34/EC. En 1995-1-1 - eurocode 5: Design of timber structures - part 1-1: General - common rules and rules for buildings. *Eurocode 5*, 2004.

D. Tuhus-Dubrow and M. Krarti. Genetic-algorithm based approach to optimize building envelope design for residential buildings. *Building and environment*, 45 (7):1574–1581, 2010.

D. Van Cauteren, D. Ramon, J. Stroeckx, K. Allacker, and M. Schevenels. Design optimization of hybrid steel/timber structures for minimal environmental impact and financial cost: A case study. *Energy and Buildings*, 254:111600, 2022.

W. Wang, R. Zmeureanu, and H. Rivard. Applying multi-objective genetic algorithms in green building design optimization. *Building and environment*, 40(11): 1512–1525, 2005a.

W. Wang, R. Zmeureanu, and H. Rivard. Two-phase application of multi-objective genetic algorithms in green building design. *Proceedings of IBPSA-2005, Montreal*, 2005b.

W. Wang, H. Rivard, and R. Zmeureanu. Floor shape optimization for green building design. *Advanced Engineering Informatics*, 20(4):363–378, 2006.

A. H. Whitworth and K. D. Tsavdaridis. Genetic algorithm for embodied energy optimisation of steel-concrete composite beams. *Sustainability*, 12(8):3102, 2020.

D. Yeo and F. A. Potra. Sustainable design of reinforced concrete structures through co 2 emission optimization. *Journal of structural engineering*, 141(3):B4014002, 2015.

V. Yepes, J. V. Martí, and T. García-Segura. Cost and co2 emission optimization of precast–prestressed concrete u-beam road bridges by a hybrid glowworm swarm algorithm. *Automation in Construction*, 49:123–134, 2015.

Y. K. Yi and A. M. Malkawi. Optimizing building form for energy performance based on hierarchical geometry relation. *Automation in Construction*, 18(6):825–833, 2009.

Appendix A

Python scripts

A.1 Geometrical model

```
import rhinoscriptsyntax as rs
import rhinoscriptsyntax as rhlib
import ghpythonlib.components as gh
import Rhino as rc
import Rhino.Geometry as rg

# Variables
Lx=60
Ly=30
height=H
divisions_x=div_x
divisions_y=div_y
spacing_x=Lx/divisions_x
spacing_y=Ly/divisions_y

# X DIRECTION
# Nodes
p_lower_chord=[] #to be used to create lines
p1_upper_chord=[] #to be used to create lines
p2_upper_chord=[] #to be used to create lines
points1_up_chord=[] #to store the points in a list
points2_up_chord=[] #to store the points in a list
points_low_chord=[] #to store the points in a list

a=0
for i in range(0,int(divisions_x+1)):
    p1_upper=gh.ConstructPoint(spacing_x*a,0,0)
    p1_upper_chord.append(p1_upper)
    points1_up_chord.append(p1_upper)
    a=a+1
```

```
31
32 a1=0
33 for i in range(0,int(divisions_x+1)):
34     p2_upper=gh.ConstructPoint(spacing_x*a1,spacing_y,0)
35     p2_upper_chord.append(p2_upper)
36     points2_up_chord.append(p2_upper)
37     a1=a1+1
38
39 b=1/2
40 for i in range(0,int(divisions_x)):
41     p_lower=gh.ConstructPoint(((spacing_x)*b),(spacing_y/2),-(
   height))
42     p_lower_chord.append(p_lower)
43     points_low_chord.append(p_lower)
44     b=b+1
45
46 # Lines
47 upper1_chord=[]
48 d=0
49 for i in range(0,int(divisions_x)):
50     horiz_upper1_chord=gh.Line(p1_upper_chord[d],
   p1_upper_chord[d+1])
51     upper1_chord.append(horiz_upper1_chord)
52     d=d+1
53
54 upper2_chord=[]
55 d1=0
56 for i in range(0,int(divisions_x)):
57     horiz_upper2_chord=gh.Line(p2_upper_chord[d1],
   p2_upper_chord[d1+1])
58     upper2_chord.append(horiz_upper2_chord)
59     d1=d1+1
60
61 lower_chord=[]
62 d2=0
63 for i in range(0,int(divisions_x)-1):
64     horiz_lower_chord=gh.Line(p_lower_chord[d2],p_lower_chord[
   d2+1])
65     lower_chord.append(horiz_lower_chord)
66     d2=d2+1
67
68 # Diagonals
69 diagonalsA=[]
70 e=0
71 for i in range(0,int(divisions_x)):
72     diag_lineA=gh.Line(p1_upper_chord[e],p_lower_chord[e])
73     diagonalsA.append(diag_lineA)
74     e=e+1
75
```

```
diagonalsB=[]
e=0
for i in range(0,int(divisions_x+1)):
    diag_lineB=gh.Line(p1_upper_chord[e],p_lower_chord[e-1])
    diagonalsB.append(diag_lineB)
    e=e+1
diagonalsB.pop(0)

diagonalsC=[]
e=0
for i in range(0,int(divisions_x)):
    diag_lineC=gh.Line(p2_upper_chord[e],p_lower_chord[e])
    diagonalsC.append(diag_lineC)
    e=e+1

diagonalsD=[]
e=0
for i in range(0,int(divisions_x+1)):
    diag_lineD=gh.Line(p2_upper_chord[e],p_lower_chord[e-1])
    diagonalsD.append(diag_lineD)
    e=e+1
diagonalsD.pop(0)

# Copies in x direction

lower_chord_copies = []
lower_chord_copy=lower_chord[:]
for i in range(1, int(divisions_y)):
    for line in lower_chord:
        new_line_low = rs.CopyObject(line, [0, i*spacing_y,
   0])
        lower_chord_copies.append(new_line_low)
lower_chord_copies.extend(lower_chord_copy)

upper_chord_copies = []
upper1_chord_copy=upper1_chord[:]
for i in range(1, int(divisions_y+1)):
    for line in upper1_chord:
        new_line_up = rs.CopyObject(line, [0, i*spacing_y, 0])
        upper_chord_copies.append(new_line_up)
upper_chord_copies.extend(upper1_chord_copy)

diagonalsA_copies = []
diagonalsA_copy=diagonalsA[:]
for i in range(1, int(divisions_y)):
    for line in diagonalsA:
        new_line_dA = rs.CopyObject(line, [0, i*spacing_y, 0])
        diagonalsA_copies.append(new_line_dA)
diagonalsA_copies.extend(diagonalsA_copy)
```

```
124
125 diagonalsB_copies = []
126 diagonalsB_copy=diagonalsB[:]
127 for i in range(1, int(divisions_y)):
128     for line in diagonalsB:
129         new_line_dB = rs.CopyObject(line, [0, i*spacing_y, 0])
130         diagonalsB_copies.append(new_line_dB)
131 diagonalsB_copies.extend(diagonalsB_copy)
132
133 diagonalsC_copies = []
134 diagonalsC_copy=diagonalsC[:]
135 for i in range(1, int(divisions_y)):
136     for line in diagonalsC:
137         new_line_dC = rs.CopyObject(line, [0, i*spacing_y, 0])
138         diagonalsC_copies.append(new_line_dC)
139 diagonalsC_copies.extend(diagonalsC_copy)
140
141 diagonalsD_copies = []
142 diagonalsD_copy=diagonalsD[:]
143 for i in range(1, int(divisions_y)):
144     for line in diagonalsD:
145         new_line_dD = rs.CopyObject(line, [0, i*spacing_y, 0])
146         diagonalsD_copies.append(new_line_dD)
147 diagonalsD_copies.extend(diagonalsD_copy)
148
149
150 # Y DIRECTION
151
152 # Points
153 p_lower_y=[] #to be used to create lines
154 p_upper_y=[] #to be used to create lines
155 points_up_y=[] #to store the points in a list
156 points_low_y=[] #to store the points in a list
157
158 a=0
159 for i in range(0,int(divisions_y+1)):
160     p_y_upper=gh.ConstructPoint(0,spacing_y*a,0)
161     p_upper_y.append(p_y_upper)
162     points_up_y.append(p_y_upper)
163     a=a+1
164
165 b=1/2
166 for i in range(0,int(divisions_y)):
167     p_y_lower=gh.ConstructPoint((spacing_x/2),(spacing_y*b),-(
    height))
168     p_lower_y.append(p_y_lower)
169     points_low_y.append(p_y_lower)
170     b=b+1
171
```

```
#Lines
upper_y_chord=[]
d=0
for i in range(0,int(divisions_y)):
    horiz_upper_y=gh.Line(p_upper_y[d],p_upper_y[d+1])
    upper_y_chord.append(horiz_upper_y)
    d=d+1

lower_y_chord=[]
d2=0
for i in range(0,int(divisions_y)-1):
    horiz_lower_y=gh.Line(p_lower_y[d2],p_lower_y[d2+1])
    lower_y_chord.append(horiz_lower_y)
    d2=d2+1

#Copies in y direction

lower_y_copies = []
lower_y_copy=lower_y_chord[:]
for i in range(1, int(divisions_x)):
    for line in lower_y_chord:
        new_line_low_y = rs.CopyObject(line, [i*spacing_x, 0,
    0])
        lower_y_copies.append(new_line_low_y)
lower_y_copies.extend(lower_y_copy)

upper_y_copies = []
upper_y_copy=upper_y_chord[:]
for i in range(1, int(divisions_x+1)):
    for line in upper_y_chord:
        new_line_up_y = rs.CopyObject(line, [i*spacing_x, 0,
    0])
        upper_y_copies.append(new_line_up_y)
upper_y_copies.extend(upper_y_copy)

# Nodes
base_nodes_up=[] #nodi superiori
for k in range(0,int(divisions_y+1)):
    for i in range(0,int(divisions_x+1)):
        nodes_up=gh.ConstructPoint(spacing_x*i,spacing_y*k,0)
        base_nodes_up.append(nodes_up)

base_nodes_low = []
for i in range(0, int(divisions_y)):
    for point in points_low_chord:
        nodes_low = rs.CopyObject(point, [0, i*spacing_y, 0])
        base_nodes_low.append(nodes_low)

corner_points = [
```

```
219     base_nodes_low[0],
                        # bottom-left corner
220     base_nodes_low[int(divisions_x*divisions_y)-int(
    divisions_x)],                # top-left corner
221     base_nodes_low[-1],
                        # top-right corner
222     base_nodes_low[int(divisions_x-1)]
              # bottom-right corner
223 ]
224
225 # FINAL OUTPUT
226 upper_stretchers=[] #upper chord list
227 upper_stretchers=upper_chord_copies+upper_y_copies
228
229 lower_stretchers=[] #lower chord list
230 lower_stretchers=lower_chord_copies+lower_y_copies
231
232 diagonals=[] #diagonals list
233 diagonals=diagonalsA_copies+diagonalsB_copies+
    diagonalsC_copies+diagonalsD_copies
234
235 base_nodes=[] #nodes list
236 base_nodes=base_nodes_low+base_nodes_up
237
238 UpStretch=upper_stretchers
239 LowStretch=lower_stretchers
240 Diagonals=diagonals
241 Nodes=base_nodes
242 Corners=corner_points
243
244
245 # Groups for load application (upper layer)
246
247 Group1_up = []
248 group1=upper1_chord[:]
249 for i in range(int(divisions_y), int(divisions_y+1)):
250     for line in upper1_chord:
251         new_group1 = rs.CopyObject(line, [0, i*spacing_y, 0])
252         Group1_up.append(new_group1)
253 Group1_up.extend(group1)
254
255 Group2_up = []
256 group2=upper_y_chord[:]
257 for i in range(int(divisions_x), int(divisions_x+1)):
258     for line in upper_y_chord:
259         new_group2 = rs.CopyObject(line, [i*spacing_x, 0, 0])
260         Group2_up.append(new_group2)
261 Group2_up.extend(group2)
262
```

```
263 Group3_up = []
264 for i in range(1, int(divisions_y)):
265     for line in upper1_chord:
266         new_group3 = rs.CopyObject(line, [0, i*spacing_y, 0])
267         Group3_up.append(new_group3)
268 
269 Group4_up = []
270 for i in range(1, int(divisions_x)):
271     for line in upper_y_chord:
272         new_group4 = rs.CopyObject(line, [i*spacing_x, 0, 0])
273         Group4_up.append(new_group4)
```

A.2 EN 1995-1-6.3.2 - Stability of timber elements

```
import rhinoscriptsyntax as rs
import math

# 6.3.2 Stability of members
Inputs:
    sigma_ct0d: Compression/tension resistance [MPa]
    sigma_myd: Resistance for pure bending y-axis [MPa]
    sigma_mzd: Resistance for pure bending z-axis [MPa]
    A_crossec: Area cross section [cm^2]
    Iy: Second moment of inertia around y-axis[cm^4]
    Iz: Second moment of inertia around z-axis[cm^4]
    L: Length of elements [m]
    beta: Buckling multiplicator [-]
    strength_d: Design value of strength properties [MPa]
    0 - f_md
    1 - f_t0d
    2 - f_t90d
    3 - f_c0d
    4 - f_c90d
    5 - f_vd
    6 - f_rd
    strength_k: Characteristic strength properties [MPa]
    0 - f_mk
    1 - f_t0k
    2 - f_t90k
    3 - f_c0k
    4 - f_c90k
    5 - f_vk
    6 - f_rk
    stiffness_k: E-modulus [MPa]
    0 - E_005
    1 - E_9005
    2 - G_05
    3 - E_0mean
    4 - E_90mean
    5 - G_mean
Output:
    util: Utilization ratio of each element

#################

E_005 = Stiffness_k[0]
f_c0k = Strength_k[3]
f_c0d = Strength_d[3]
f_myd = Strength_d[0]
f_mzd = Strength_d[0]
```

```
47
48 A = A_cross * 10**-4 #Area of cross-section [m^2]
49
50 I_y = Iy * 10**-8 #Second moment of inertia around y-axis [m
    ^4]
51 I_z = Iz * 10**-8 #Second moment of inertia around z-axis [m
    ^4]
52
53 util = [] #Empty output list
54
55 ratioY = []
56 ratioZ= []
57
58 # Buckling length
59 #beta = 0.7 #The Euler bucklinglength depends on the support
    condition,
60 #L_ef = [i * beta for i in L] # free top-fixed = 2, pinned-
    pinned = 1, pinned-fixed = 0.7, fixed-fixed = 0.5
61
62 L_ef = L * beta
63
64 # Critical euler load
65 sigma_cry = (math.pi**2)*E_005*I_y/(A*L_ef**2)
66 sigma_crz = (math.pi**2)*E_005*I_z/(A*L_ef**2)
67
68
69 # Relative slenderness ratio
70 lambda_rely = math.sqrt(f_c0k/sigma_cry)
71 lambda_relz = math.sqrt(f_c0k/sigma_crz)
72
73 # Reduction parameters
74 beta_c = 0.1 #straightness factor: 0.1 for glued laminated
    timber & LVL, 0.2 for solid timber.
75
76 k_y = 0.5*(1+beta_c*(lambda_rely-0.3)+lambda_rely**2)
77 k_z = 0.5*(1+beta_c*(lambda_relz-0.3)+lambda_relz**2)
78
79 k_cy = 1/(k_y+math.sqrt(k_y**2-lambda_rely**2))
80 k_cz = 1/(k_z+math.sqrt(k_z**2-lambda_relz**2))
81
82
83 # Expression to satisfy
84 km = 0.7 #crosse-section parameter [-] 0.7 for rectangular
    sections, 1.0 for others.
85
86 for i in range(0,len(sigma_ctd)):
87     eq1 = abs(sigma_ctd[i])/(k_cy*f_c0d)+abs(sigma_myd[i])/(
    f_myd)
88     eq2 = abs(sigma_ctd[i])/(k_cz*f_c0d)+km*abs(sigma_myd[i])
```

```
    /(f_myd)
89      eq_max = max(eq1,eq2)
90      util.extend([max(eq1,eq2)])
91 i=i+1
```

Appendix B

Case study 1: Space frame roof

B.1 Model validation

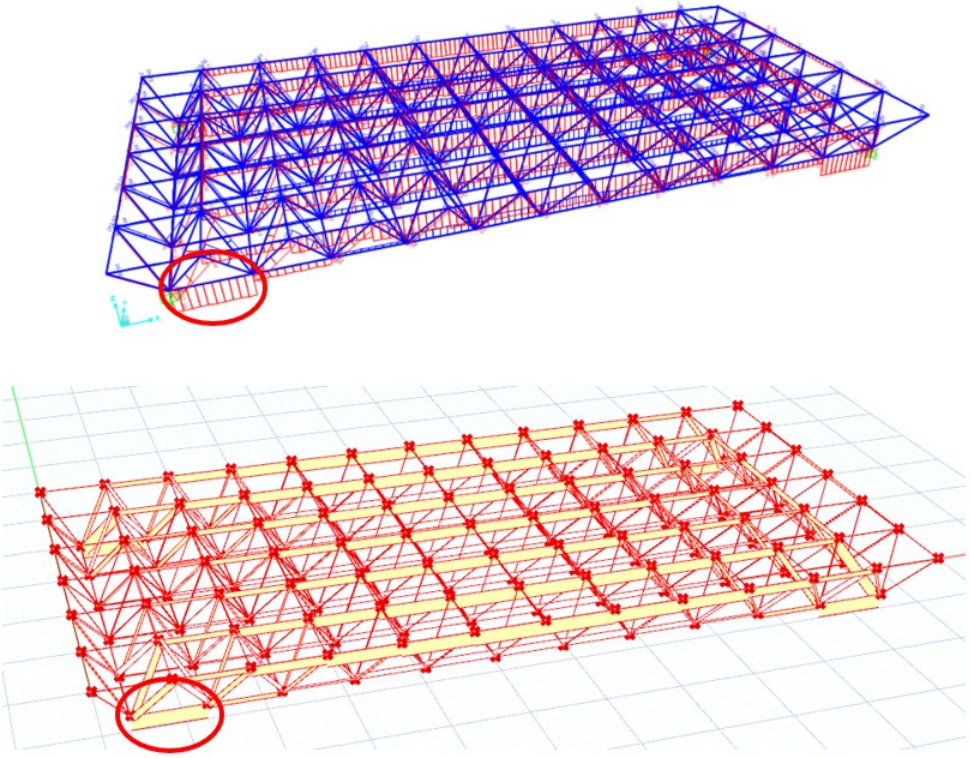

Figure B.1: Comparison of actions of the beam circled in red between SAP2000 and Grasshopper

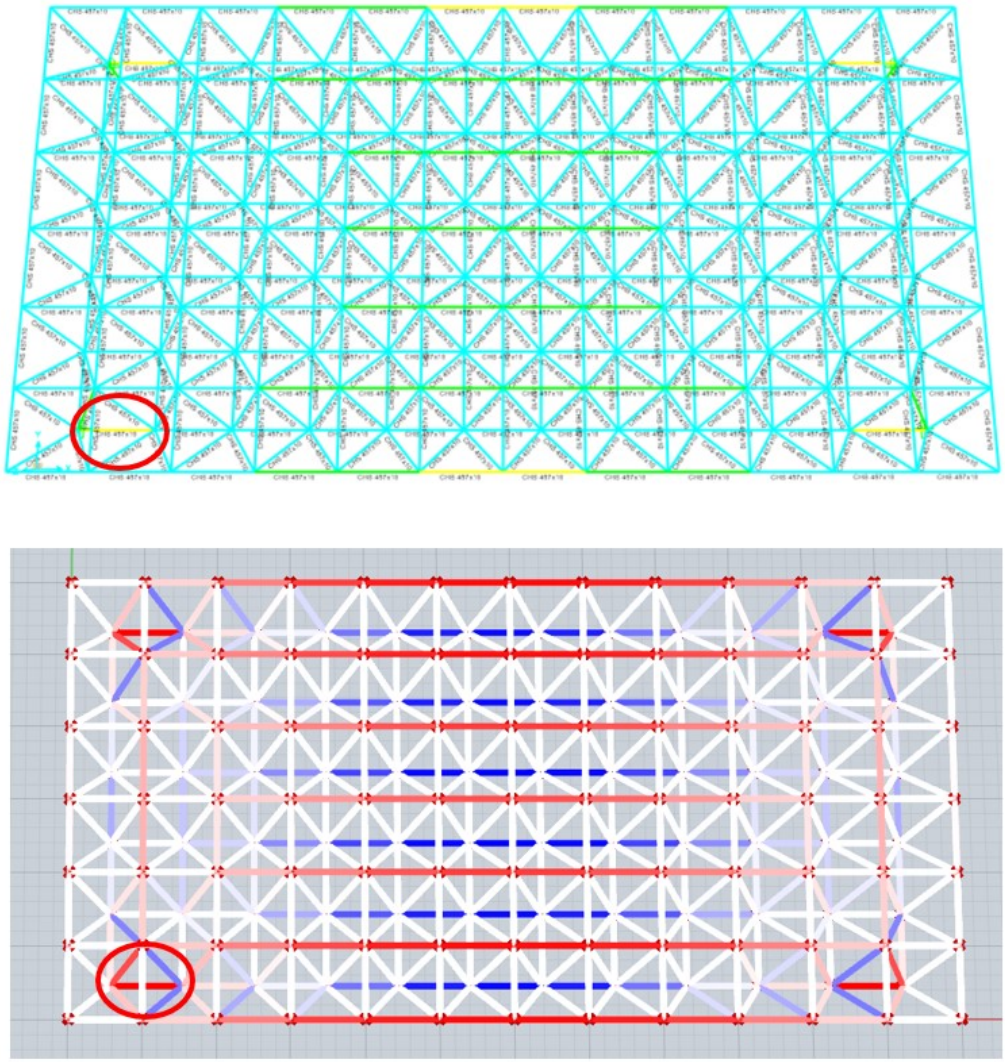

Figure B.2: Comparison of D/C ratios of the beam circled in red between SAP2000 and Grasshopper

B.2 Optimization results

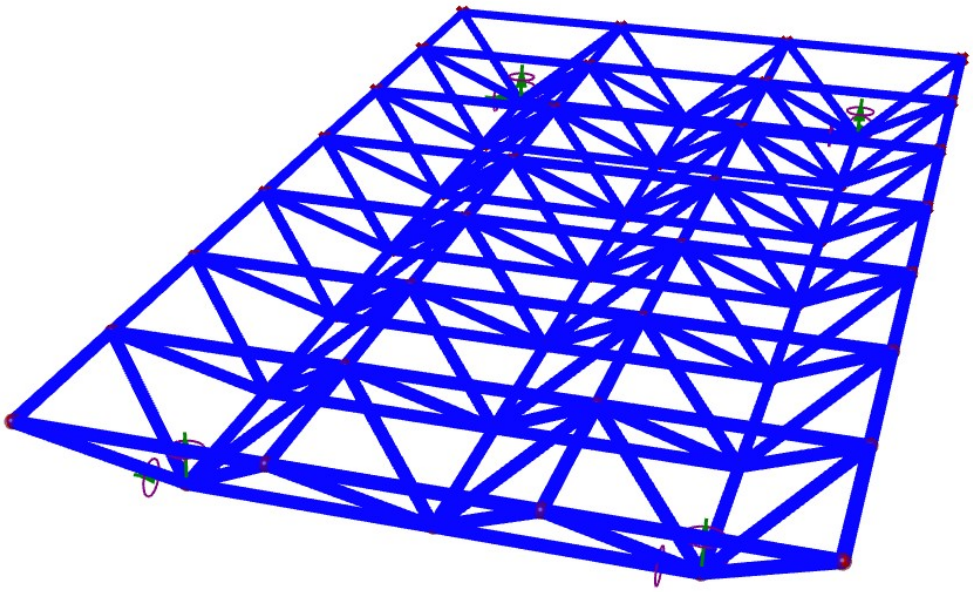

Figure B.3: Configuration A - Perspective view of the optimized structure

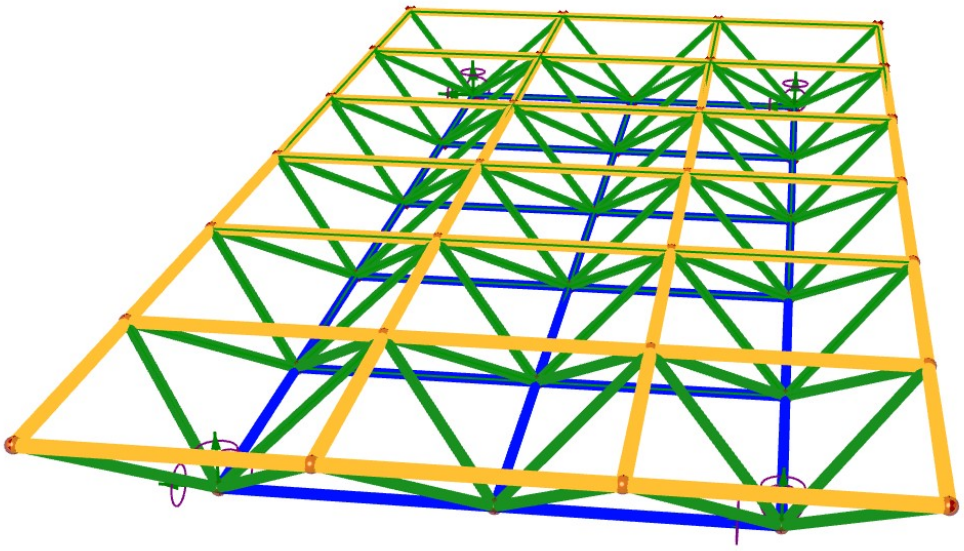

Figure B.4: Configuration B - Perspective view of the optimized structure

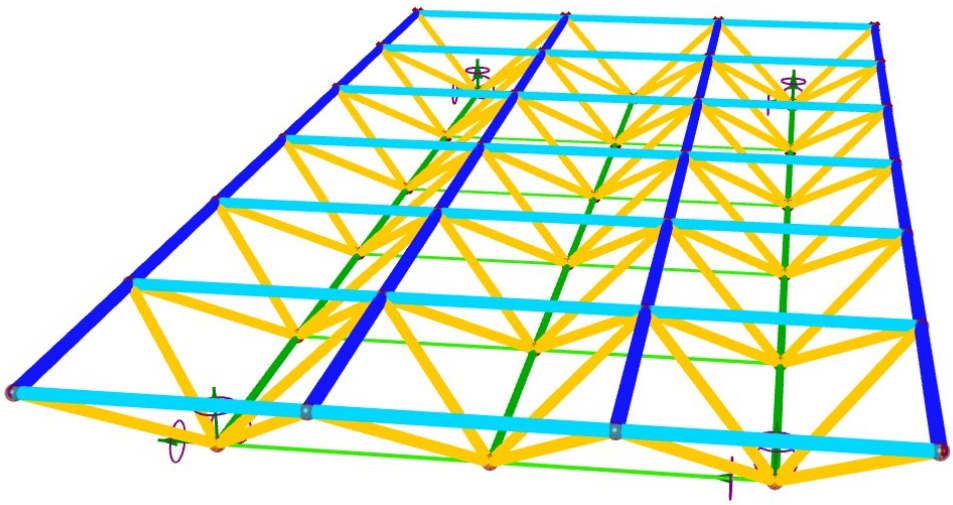

Figure B.5: Configuration C - Perspective view of the optimized structure

Appendix C

Case study 2: Industrial building

C.1 LCA integration

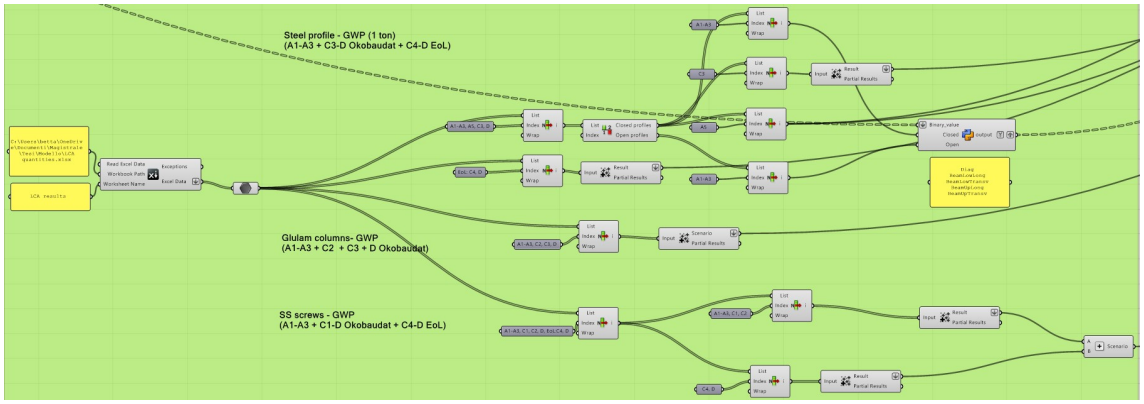

Figure C.1: Excel-reader tool for LCA data

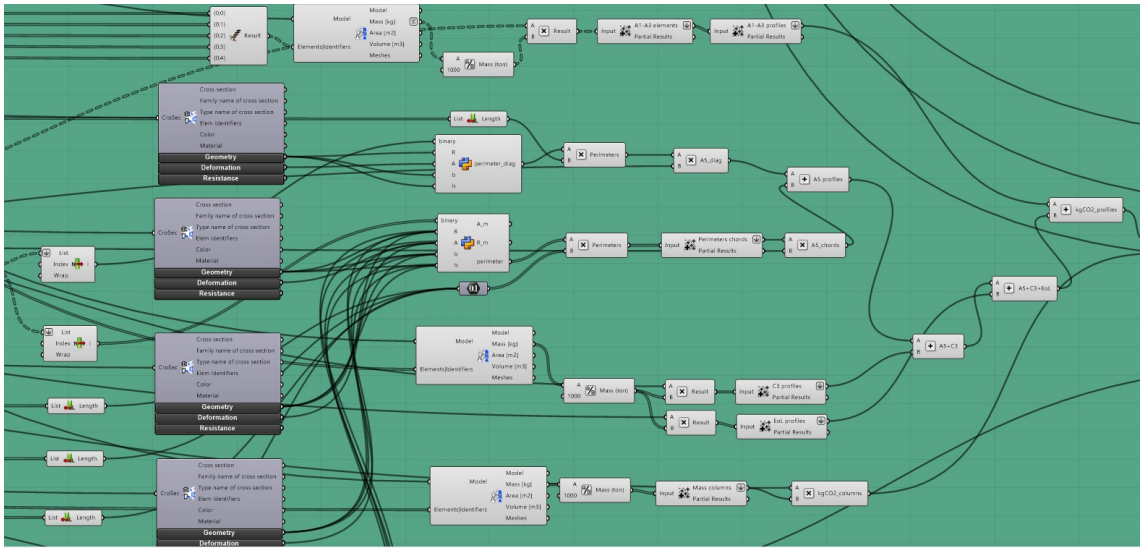

Figure C.2: Example of LCA indicator calculation for steel profiles and columns (Scenario 1)

C.2 Optimization results - Scenario 1

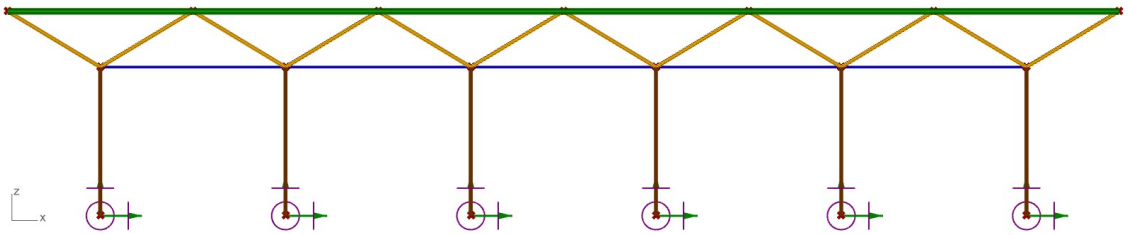

Figure C.3: Optimal configuration of Scenario 1 - Front view

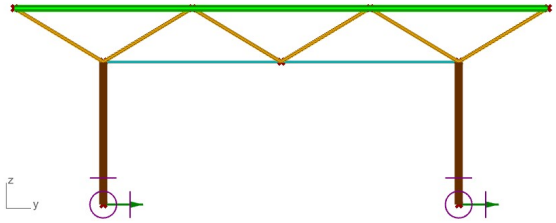

Figure C.4: Optimal configuration of Scenario 1 - Lateral view

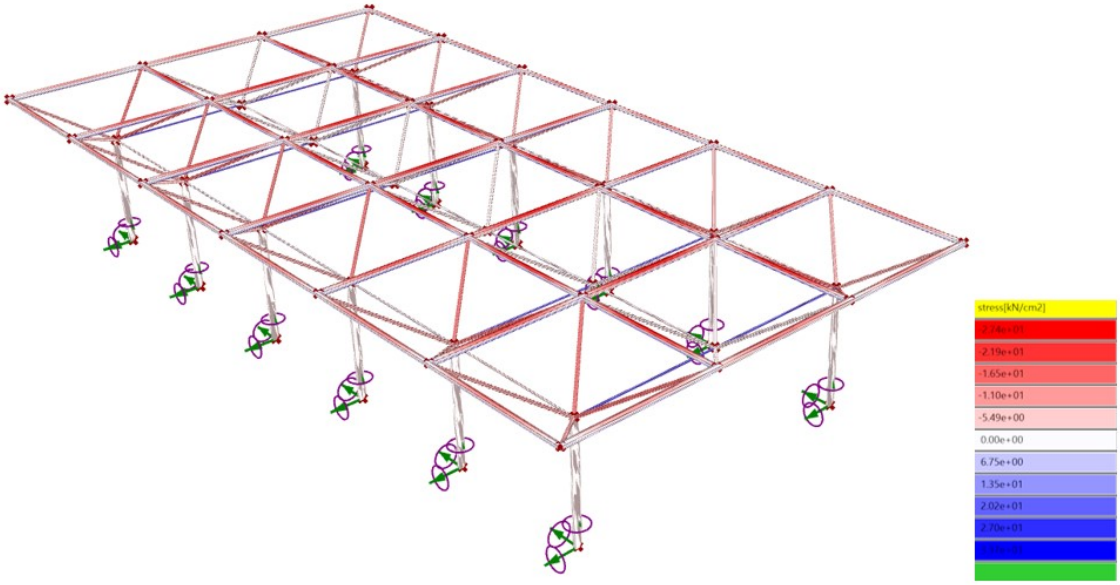

Figure C.5: Axial stress of U-point optimal configuration

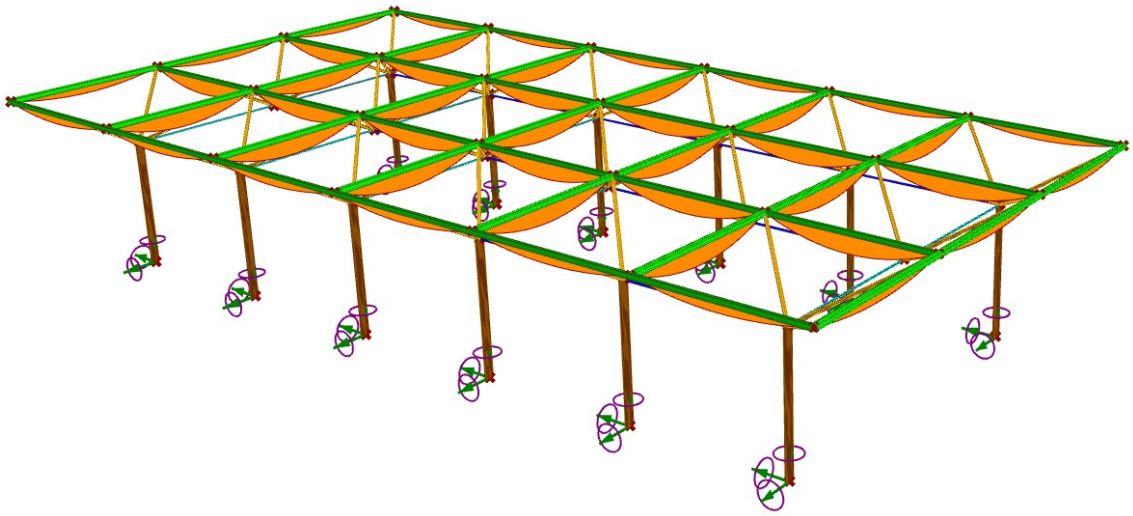

Figure C.6: Bending moment of U-point optimal configuration

C.3 Optimization results - Scenario 2

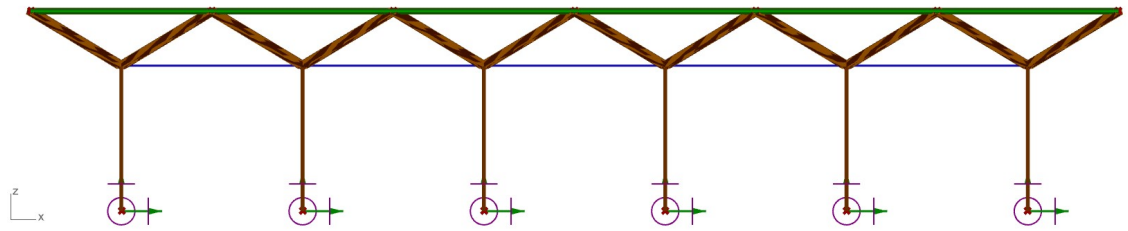

Figure C.7: Optimal configuration of Scenario 2 - Front view

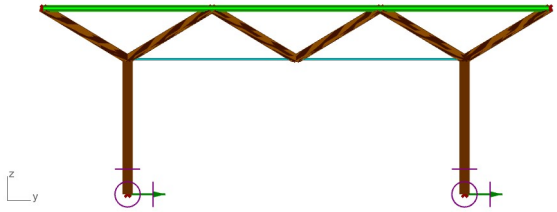

Figure C.8: Optimal configuration of Scenario 2 - Lateral view

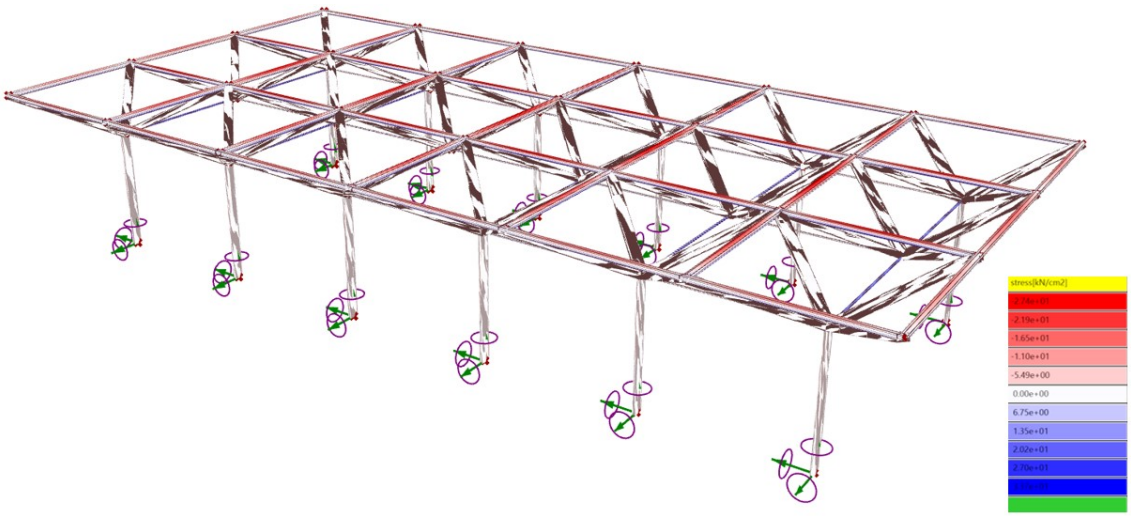

Figure C.9: Axial stress of U-point optimal configuration

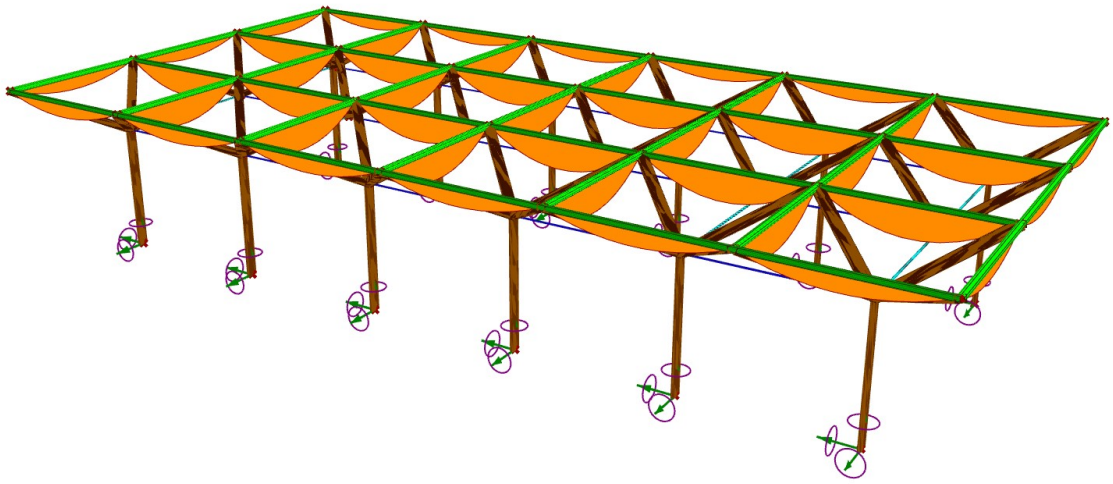

Figure C.10: Bending moment of U-point optimal configuration